Fall 12-2011

Synthesis and Characterization of Acceptor: Donor Block Copolymers for Organic Photovoltaics

Brandon Cory Achord
University of Southern Mississippi

The University of Southern Mississippi

SYNTHESIS AND CHARACTERIZATION OF ACCEPTOR: DONOR BLOCK COPOLYMERS FOR ORGANIC PHOTOVOLTAICS

by

Brandon Cory Achord

An Abstract of a Dissertation
Submitted to the Graduate School
of The University of Southern Mississippi
in Partial Fulfillment of the Requirements
for the Degree of Doctor of Philosophy

December 2011

ABSTRACT

SYNTHESIS AND CHARACTERIZATION OF ACCEPTOR:

DONOR BLOCK COPOLYMERS FOR ORGANIC PHOTOVOLTAICS

by Brandon Cory Achord

December 2011

Mankind needs sources of clean power. Photovoltaic (PV) cells, in use since 1839, have proven reliable and practical for certain applications. PV cell efficiency has changed over the years from 1-2% to ultra-high efficiency cells operating at efficiencies greater than 40%. Organic photovoltaics are a potential transformative technology platform. The potential for cell use, efficiency and cost are all parts of the research and development focus at the time this document was written. This research was initiated with a focus on the synthesis and understanding of the variables effecting acceptor-donor block copolymer. The self-assembled morphology resulting from varying volume ratios of each block in the absence and presence of both A and B homopolymers singularly and in combination was examined.

DEDICATION

To my parents who went out of their way to ensure I was provided opportunity, and continually pushed me to achieve my goals. Without their guidance and support I never would have achieved this milestone.

ACKNOWLEDGMENTS

I would like to extend my appreciation to my advisor Dr. James Rawlins, for his guidance in the research direction, and most of all for fostering an environment in which quality research is preformed and encouraged. Special thanks to my committee members, Drs. Paige Buchanan, Kenneth Mauritz, Robert Moore, Daniel Savin, and Robson Storey for guidance and suggestions throughout my graduate career. Members of TRRG all deserve recognition, but specifically I would like to thank my fellow classmates James Whittemore and Pirro Cipi, along with Sharathkumar Mendon, Dr. Eric Williams, and David Delatte for the many research-based conversations and the ideas they offered to improve my research path. Final recognition is owed to Alexandra Jarriel for her assistance and diligence in performing the many tasks and reactions I asked of her. I am most grateful for the funding I received throughout the years, specifically from the Robert M. Hearin Foundation and the Department of Energy Grant # DE-EE003173.

The University of Southern Mississippi

SYNTHESIS AND CHARACTERIZATION OF ACCEPTOR: DONOR BLOCK COPOLYMERS FOR ORGANIC PHOTOVOLTAICS

by

Brandon Cory Achord

A Dissertation
Submitted to the Graduate School
of The University of Southern Mississippi
in Partial Fulfillment of the Requirements
for the Degree of Doctor of Philosophy

Approved:

_____
Director

_____

_____

_____

_____

_____
Dean of the Graduate School

December 2011

TABLE OF CONTENTS

ABSTRACT ii

DEDICATION iii

ACKNOWLEDGMENTS iv

LIST OF TABLES viii

LIST OF FIGURES x

LIST OF EQUATIONS xix

LIST OF SCHEMES xx

CHAPTER

I. INTRODUCTION 1

Photovoltaics
Organic Photovoltaics
Conductive Polymers
Scale and Material Specific Locations for Better Morphology Control and Matching with Internal Conversion Efficiency
References

II. MATERIALS, EXPERIMENTAL, CHARACTERIZATION TECHNIQUES AND PROCEDURES 39

Materials
Experimental Procedures
Characterization Techniques
References

III. REGIOREGULARITY CONTROL THROUGH MONOMER FUNCTIONALIZATION 61

Introduction
Modification of 3-hexylthiophene
Polymerization of 2-bromo-3-hexyl-5-iodothiophene by GRIM
Summary
References

IV. GRIGNARD METATHESIS POLYMERIZATION OF 3-HEXYLTHIOPHENE 71

Introduction
Experimental
Results and Discussion
Regioregularity Control and Monomer Reactivity/Kinetics
Proposed Mechanism
Summary
References

V. END-CAPPING OF P3HT AND SITE TRANSFORMATION FOR ADDITION OF PS:CMS BLOCK BY COUPLING AND SEQUENTIAL BLOCK GROWTH..... 101

Introduction
Grignard Metathesis End-capping Reactions
Hydroboration/Oxidation of Vinyl-P3HT
Preparation of Heck-Coupling Precursor and Heck Coupling Reaction
Summary
References

VI. SYNTHESIS OF ACID FUNCTIONAL POLYSTYRENE:CHLOROMETHYL STYRENE AND P3HT:PS:CMS AND P3HT:PS:CMS..... 121

Introduction
Random Copolymerization of Styrene and Chloromethyl Styrene
References

VII. ATOM TRANSFER RADICAL ADDITION OF BUCKMINSTER FULLERENE AND FINAL BLOCK COPOLYMER SYNTHESIS 137

Introduction
Atom Transfer Radical Polymerization/Addition Proof of Concept
Acid-PS:CMS:Fu
P3HT:PS:CMS:Fu
Summary
References

VIII. PROPERTY ANALYSIS OF RESULTING POLYMERS..... 159

Introduction
Results and Discussion
Summary
References

IX. CONCLUSIONS AND RECOMMENDATIONS FOR FUTURE WORK 188

Conclusions
Suggestions for Future Work
References

LIST OF TABLES

Table

1. Peak molecular weights (from GPC) and percent regioregularity of GRIM Polymerization of 2-bromo-3-hexyl-5-iodothiophene 68

2. Resulting peak molecular weights (from GPC) and percent regioregularity of select GRIM Polymerizations of 2,5-dibromo-3-hexythiophene 68

3. Number average molecular weight by comparison of GPC (non-corrected), GPC (corrected) and MALDI-ToF 78

4. Molecular weights based on varying nickel to monomer ratios and reaction times 82

5. Corrected number average molecular weight, polydispersity indices, and percent area of high molecular weight shoulder 91

6. Molecular weight and yield data for reactions weight varying nickel addition times 94

7. Formulation and reaction conditions for vinyl end-capping 108

8. Styrene/chloromethyl styrene formulations and molecular weight results from AIBN initiation 127

9. Compositional data for styrene chloromethyl styrene copolymers initiated by AIBN 129

10. Styrene/Chloromethyl styrene formulations and molecular weight results from 4,4'-azobis(4-cyanovaleric acid) initiation 129

11. Compositional data for styrene chloromethyl styrene copolymers initiated by ACVA 132

12. Percent end-group functionalization based off Number average molecular weight and NMR integrations for ACVA initiated systems and AIBN negative control 134
13. Comparison of the areas of absorbance and fluorescence along with ratios, defining exciton quenching..... 170

LIST OF FIGURES

Figure

1. Generic and Common PV Cell 6

2. Top Contact Construction 8

3. Multijunction Solar Cell 11

4. Charge diagram for the potential processes involved in photovoltaic cells 15

5. Colloidal PANI particles stabilized with hydroxypropylcellulose 19

6. Granular structure of a PANI precipitate obtained in a standard polymerization 19

7. PANI nanotubes obtained by the oxidation of aniline with ammonium peroxydisulfate in acetic acid at -4º C 20

8. SEM with inset TEM image of Polypyrrole 21

9. Buckminster Fullerene, C_{60} 25

10. Progression of morphology control in organic photovoltaics 26

11. Common morphologies of block copolymers 28

12. Representative rod-coil morphologies: (a) wavy-lamellar; (b) bi-layer and interdigitating chains 29

13. Styrene 39

14. Hexylthiophene 39

15. 2-Bromo-3-hexylthiophene 40

16. 4-Bromostyrene 40

17. Vinyl Magnesium Bromide 40
18. *t*-Butyl Magnesium Bromide 40
19. 2-Bromo-3-hexyl-5-iodothiophene 41
20. 2,5-Dibromo-3-hexylthiophene 41
21. 1-(Chloromethyl)4-vinylbenzene 41
22. 4,4'-Azobis(4-cyanovaleric acid) 42
23. 1,3-Bis(diphenylphosphino)propane dichloronickel (Ni(dppp)Cl_2) 42
24. *N*,*N*,*N*',*N*',*N*",*N*"-Pentamethyldiethylenetriamine (PMDETA) 42
25. 2,2,6,6-Tetramethyl-1-piperidine-1-oxyl (TEMPO) 43
26. (2-Phenyl-2-(2,2,6,6-tetramethylpiperidin-1-yloxy)ethyl)magnesium bromide 43
27. 1-(1-(4-Bromophenyl)ethoxy)-2,2,6,6-tetramethylpiperidine 43
28. P3HT-TEMPO (Macroinitiator 1) 44
29. Regioregular Poly(3-hexylthiophene) (rrP3HT) 44
30. Vinyl P3HT (vP3HT) 44
31. Hydroxy-P3HT (hP3HT) 45
32. Acid functional polystyrene:chloromethylstyrene (PS:CMS) 45
33. Acid functional polystyrene:chloromethylstyrene:fullerene (PS:CMS:Fu) 46
34. Idealized Goal macromolecule - Block-poly-3-hexylthiopehene-block-polystyrene:chloromethylstyrene:fullerene (b-P3HT-b-PS:CMS:Fu) 46
35. Histogram for publications of P3HT related documents 62

36. ^{13}C NMR (from top to bottom) of 2-bromo-3-hexyl-5-iodothiophene, 2-bromo-3-hexylthiophene, and, 3-hexylthiophene 64
37. GC-MS of 3-hexylthiophene, 2-bromo-3-hexylthiophene, and 2-bromo-3-hexyl-5-iodothiophene illustrating purity and conversion 65
38. ^{1}H NMR spectrum and integration of regioregular P3HT (rr-P3HT) in polymers of 2-bromo-3-hexyl-5-iodothiophene 67
39. SEM-EDX of a) raw P3HT after precipitation, b) unpurified inorganic salts from precipitation media, c) purified inorganic salts, d) low molecular weight P3HT from hexanes extraction, and e) insoluble fraction remaining in filter 76
40. Correlation of molecular weights of poly(3-alkylthiophenes) as calculated by GPC and MALDI-TOF 78
41. Corrected number average molecular weight via GPC of P3HT as a function of reaction time at various initial molar monomer concentrations and constant 60:1 monomer to nickel ratio 80
42. GPC based polydispersity index values for P3HT as a function of reaction time at various initial molar monomer concentrations and a constant 60:1 monomer to nickel ratio 81
43. ^{1}H NMR illustrating change in regioregularity between molecular weight fractions. Irregular linkages appear at 2.60 ppm 83
44. Structures of a) regioregular linkages (head-to-tail) and b) regioirregular linkages (tail-to-tail 84

45. Percent conversion of 0.1M polymerization of 3-hexylthiophene as monitored by GC-MS 85
46. RI trace of 0.1 M polymerization of 3-hexylthiophene showing molecular weight increase and leveling with continual increase of polymer concentration 85
47. MALDI-TOF results of 0.1 molar polymerization of 3-hexylthiophene quenched with methanol showing both H-Br terminated chains as well as Br-Br terminated chains..... 87
48. Expanded MALDI-TOF of 0.1 molar polymerization of 3-hexylthiophene quenched with methanol showing both H-Br terminated chains as well as Br-Br terminated chains..... 87
49. Expanded MALDI-TOF of 0.1 molar polymerization of P3HT quenched with 5M HCl showing both H-Br terminated chains as well as Br-Br terminated chains..... 88
50. RI traces of 0.1 molar polymerization of P3HT with secondary 0.06 M monomer addition (P3HT)..... 90
51. Surface spectra as recorded by ReactIR, arrows indicate peaks of interest 93
52. Trends for conversion of t-butylmagnesium chloride, 804-783cm^{-1} 93
53. ^{1}H NMR showing regioregularity versus molecular weight: lower molecular weight species are on the bottom 96
54. Graph of Number average molecular weight versus regioregularity 96

55. GC-MS of product prior to washing and recrystallization 104
56. ^{13}C NMR of product prior to washing and recrystallization 105
57. ^{1}H NMR of product prior to washing and recrystallization 105
58. Possibly side reactions a) dibrominated styrene b) dibrominated oliogmeric species c) TEMPO functionalized oligomer 106
59. ^{1}H NMR of purified (2-Phenyl-2-(2,2,6,6-tetramethylpiperidin-1-yloxy)ethyl) magnesium bromide 106
60. ^{1}H NMR with peak assignments of Vinyl end capped P3HT 110
61. ^{1}H NMR of P3HT after quenching with (2-Phenyl-2-(2,2,6,6-tetramethylpiperidin-1-yloxy)ethyl) magnesium bromide 111
62. ^{1}H NMR after Hydroboration/oxidation of vinyl-P3HT 114
63. ^{1}H NMR of 1-bromo-4-(1-bromoethyl)benzene 116
64. ^{1}H NMR of 1-(1-(4-bromophenyl)ethoxy)-2,2,6,6-tetramethylpiperidine..... 117
65. ^{1}H NMR of P3HT after reaction with 1-(1-(4-bromophenyl)ethoxy)-2,2,6,6-tetramethylpiperidine..... 118
66. Number Average Molecular Weight versus conversion for Nitroxide Mediated Polymerization of n-butyl acrylate..... 124
67. Representative ^{1}H NMR of copolymers of styrene and chloromethyl styrene 128
68. TEMPO mediated systems initiated by AIBN (Pink trace) and ACVA (Green Trace) 130

69. AIBN (Blue trace) and ACVA (Red trace) initiated systems in the absence of TEMPO 130
70. GPC RI traces for P3HT macroinitiator before and after attempts of sequential block addition 135
71. ^{1}H NMR of polystyrene:chloromethyl styrene polymer (black trace) and b) ATRP initiated branched polystyrene (red trace) 141
72. GPC of polystyrene:chloromethyl styrene polymer (black trace) and b) ATRP initiated branched polystyrene (red trace) illustrating effective initiation from chloromethyl group 141
73. ^{1}H NMR of polystyrene:chloromethyl styrene polymer (black trace) and b) polystyrene:chloromethyl styrene/Fullerene (red trace) 144
74. GPC of polystyrene:chloromethyl styrene polymer (black trace) and b) fullerene containing polystyrene (red trace) illustrating effective initiation from chloromethyl group 145
75. DSC curve of Buckminster Fullerene 146
76. DSC curve of phenyl-C61-butyric acid methyl ester 147
77. Example DSC curve of a polystyrene-stat-chloromethyl styrene copolymer 147
78. DSC of intractable crosslinked PS-stat-CMS/Fu showing presence of non-grafted fullerene 149
79. DSC of a completed acceptor block (polystyrene-stat-Chloromethyl styrene/Fullerene 149

80. TGA of Buckminster Fullerene (black trace) and its derivatives, PCBM (red trace), crosslinked fullerene functional polystyrene (blue trace) and a functional polystyrene with pendant fullerene (green trace 151
81. Coupling reaction of 10,000 gm/mole P3HT-OH (black trace) and 15,000 gm/mol PS-stat-CMS/Fu (green trace) in the absence of catalyst, with the red trace being the final product..... 153
82. Coupling reaction of 10,000 gm/mole P3HT-OH (black trace) and 15,000 gm/mol PS-stat-CMS/Fu (green trace) in the presence of dibutyl tin dilaurate catalyst, with the red trace being the final product 154
83. Coupling reaction of 20,000 gm/mole P3HT-OH (blue trace) and 15,000 gm/mol PS-stat-CMS/Fu (navy trace) in the presence of dibutyl tin dilaurate catalyst, with the purple trace being the final product..... 155
84. Graph illustrating bandgap correlation to the solar spectrum..... 163
85. Absorbance and emission spectrum of P3HT in solution of chloroform..... 164
86. Absorbance of P3HTdrying process cast from 1 wt% chloroform solution 165
87. Normalized UV-Vis and Fluorescence of dry P3HT film 166
88. Comparison of block copolymer and homopolymer absorbencies in chloroform 167
89. Comparison of block copolymer and homopolymer fluorescence in chloroform 168

90. Comparison of block copolymer and homopolymer fluorescence in dry films, illustrating quenching 169
91. TGA of P3HT performed in air at a rate of 10ºC per minute 172
92. Mass-spec corresponding to dual degradation mechanisms in P3HT 172
93. DSC analysis of P3HT illustrating Tg and typical crystalline melt transition 174
94. TGA analysis for Block Copolymers for confirmation of fullerene % incorporation using 20,000 g/mole P3HT performed in 1) in nitrogen up to 650 ºC and switched to compressed air at that temperature and compared with 2) the same polymer in a nitrogen atmosphere throughout 175
95. AFM phase image of P3HT and PCBM mix at a 1:1 weight ratio 177
96. AFM phase image of physical blend of 20,000 g/mole P3HT and 20,000 g/mole PS:CMS/Fu 177
97. Completed block copolymer of 10,000 g/mole P3HT and 20,000 g/mole PS:CMS/Fu 178
98. Completed block copolymer of 20,000 g/mole P3HT and 20,000 g/mole PS:CMS/Fu prefiltration 179
99. Completed block copolymer of 20,000 g/mole P3HT and 20,000 g/mole PS:CMS/Fu post filtration through 0.45 micron filter 179
100. Photovoltaic efficiency curve for P3HT:PCBM bulk heterojunction cell, illustrating the key points for photovoltaic measurement 181

101. Photovoltaic efficiency curve for P3HT and PS:CMS/Fu physical blend/bulk heterojunction cell 182
102. Photovoltaic efficiency curve for P3HT –b-PS:CMS/Fu physical blend/bulk heterojunction cell 182
103. SEM image of 20kP3HT-20KPS:CMS/Fu block copolymer spin cast on mica 183
104. The concept of properties 189

LIST OF EQUATIONS

1. Relationship of tip deflection to indention displacement 58

2. Percent vinyl functionalization via GPC and NMR results 109

3. Percent end-functionalization by NMR and GPC results 112

4. Percent hydroxyl functionalization via GPC and NMR results 115

5. Quantification of percent incorporation of chloromethyl styrene 128

6. Correlation of optical band-gap to the solar spectrum 163

LIST OF SCHEMES

1. Accepted Mechanisms of Grignard Metathesis Method for the Synthesis of Regioregular Poly(3-hexylthiophene) 72

2. GRIM Mechanism as proposed by Rawlins' Group 98

3. Synthesis of 1-(2-bromo-1-phenylthoxy)2,2,6,6-tetramethylpiperidine 103

4. Mechanism of Hydroboration/Oxidation of Vinyl P3HT 113

5. Mechanism of operation for living free radical polymerization where R is a mediating species 123

6. Side reaction mechanism for TEMPO mediated polymerization of CMS 133

CHAPTER I

INTRODUCTION

Mankind needs sources of clean power. Photovoltaic (PV) cells, in use since 1839, have proven reliable and practical for certain applications. Cells typically function by collecting photons within a phosphorous doped silicon material that has electron hole and electron rich regions sandwiched between conductive layers (normally not in the path of incident light). PV cell efficiency has increased over the years from 1-2% to ultra-high efficiency cells. Polycrystalline silicon solar cells are commonly 19.8% efficient. Multi-layer and specialty cells have achieved greater than 40% power conversion but at extraordinarily high costs. Another potential transformative technology platform is organic PV (OPV) cells. At the time of this document's writing, the focus of OPV research and development is cell use area, efficiency and cost considerations. Most OPV cells are relatively low efficiency and exhibit truncated lifetimes versus silicon cells. On the contrary, OPV systems are thinner, lower in mass and typically prove to absorb light more efficiently versus thickness as well as from off-normal absorption. In addition, OPV can be applied to a wide variety of substrates, surfaces and applications with minimal influence on the architectural/structural engineering needs. The current debate rests on cost effectiveness at a cost per watt produced. In current dollars and kWh costs (2011 July), OPV cells require 8-11% cell efficiency to compete directly with inorganic cell technology.

The basis of OPV cells are acceptor and donor materials. Specifically conductive polymers provide photon absorption over a broad UV Vis and IR range while facilitating exciton formation as the photon to electron source. Ideally, they will donate or transfer that excited species to the donor material whereby electric current is produced. Efficient transfer from photon to electron is currently thought to be limited by a few main factors. A critical factor is the time and distance of exciton diffusion before self-quenching. Therefore, this research was initiated with a focus on the synthesis and understanding of the variables affecting the self-assembly process of acceptor-donor block copolymers. Specifically, the self-assembled morphology resulting from varying volume ratios of each block and block copolymers in the absence and presence of both A and B homopolymers singularly and in combination. The dominant hypothesis can be reduced to: OPV efficiency gains are tethered to the size and scale of morphology between donor and acceptor materials, and fully functionalized block copolymers match the appropriate size scale to examine efficiency limit correlation to exciton diffusion length/time.

Photovoltaics

For mankind the shift from seven billion people toward an estimated nine billion people worldwide by the year 2050 will force us to question how every resource and technology is to be used and can be used more efficiently. Several interrelated resource issues are at a critical stage for mankind. The most common are clean water, rare metals and chemicals, sufficient nutrition, clean air, liquid fuels and power. Preferably, renewable, alternative and/or efficient

energy sources will be developed and optimized for facile collection/use/distribution. Energy issues are currently one of the most important issues facing mankind. Solar power offers almost every advantage desired in alternative energy development and generation. Solar power generation and distribution have been primarily limited by cost, application difficulty and limited light exposure that varies drastically across geographic regions and at night. However, the clear inherent advantages of energy produced via PV means have consistently maintained solar power at the top of the alternative energy options' list. Burdened by nonrenewable and readily polluting resources such as coal, oil and nuclear power, our supply concerns and environmental issues are a driving force for change. PV cells, or solar cells, convert energy absorbed directly from the sun to electricity. Since the 1970s, solar cell technology has advanced to the point where it is now adapted commercially and is considered acceptable for many applications. Advancements have facilitated research towards optimizing system efficiency and performance by focusing on areas such as cell composition, cell morphology, cell engineering, processing methodologies and wiring system optimization.

Silicon is currently the standard material for producing solar cells. Solar power in most markets is not directly competitive with other energy sources, e.g., coal and natural gas. The price of finished cells is driven by production costs and complicated processing.[1] More than ever, the future of PV is focused on polymeric PV systems from which broad and tunable energy absorption frequencies are possible. Application methods are simplified to facilitate higher

power conversion efficiencies and practical utilization. Polymeric PV technology allows a broader range of fabrication/production options, many of which are automated and industrially proven; specifically, inkjet and roll-to-roll production combinations that translate directly to higher rates and reduced process costs.[2]

Solar Cell History and Developmental Timeline

Electrical power generation via solar cells originated in 1839 when Edmond Becquerel, a French physicist, discovered and validated the PV effect. Specifically, Becquerel exhibited and tried to quantify the absorption and conversion of photons (solar energy) into electron flow (electricity). Becquerel, only 19 at the time, discovered the effect while experimenting with a two metal, electrode-based electrolytic cell. Becquerel observed that certain material combinations produced electrical current when exposed to sunlight. In the 1870s, the first solid PV material, selenium, was observed. This transformative discovery sparked interest in solar power. Unfortunately after more than 35 years of additional investigations (1914), the efficiency of selenium-based solar cells remained less than 1% efficient when converting sunlight into electrical power.[3]

The first inorganic PV cell was reduced to practice at Bell Laboratories in 1954.[4] The solar battery, as it was termed originally, utilized razor blade-sized strips of silicon connected in series and parallel to generate appropriate current. The first cell was limited to an efficiency of 6% at converting the sun's power into electrical power. The first publicized PV cell utilization was launched on March 17, 1958, with the introduction of the first solar powered satellite, the Vanguard

1.[5] Even though the first generation solar panels were developed specifically for earth orbiting satellites, the applications broadened quickly after their inception. Petroleum companies made the first commercially significant use of PV technology by supplying power to light duty equipment on offshore oil rigs and eliminating the need of large banks of batteries. Battery interchanging, as the process was known, required large boats for battery transport and either helicopters or cranes to make the exchange. Smaller rechargeable batteries in combination with solar cells resulted in tremendous savings in manpower, support and cost even at low PV efficiencies.[5]

Basics of Solar Cell Operation

Solar cell technologies have transformed tremendously since inception. The technology was originally focused on simple doped silicon cells and is ever shifting towards more complex multi-junction/multi-phase cells. The key breakthroughs and research transition for solar power technology are reviewed briefly below. The goal within solar power research is to reduce the dollar watt ratio for greater market competitiveness. The market is already established and ready for rapid penetration as soon as the produced and installed parity in prices is achievable versus other energy sources. Although, many higher efficiency cells/cell technologies have been developed and evaluated at varying scales between laboratory and full scale production, most are not in commercial production. Most often the barrier remains centered on high fabrication costs and production difficulties at large scale with many low tolerance design variables.

The basic PV concept cell is simple; light energy is absorbed and electrical energy is produced. The more fundamental research question is consistently, "what is really occurring?" Commercial PV cells are most commonly silicon based, and for this reason our discussion starts with this technology overview.[6]

Regarding particular layers within a cell design, PV cells are generally comprised of a back contact, p-doped silicon layer, n-doped silicon layer, front contact, anti-reflective coating, transparent adhesive and a final cover, generally glass (Figure 1).

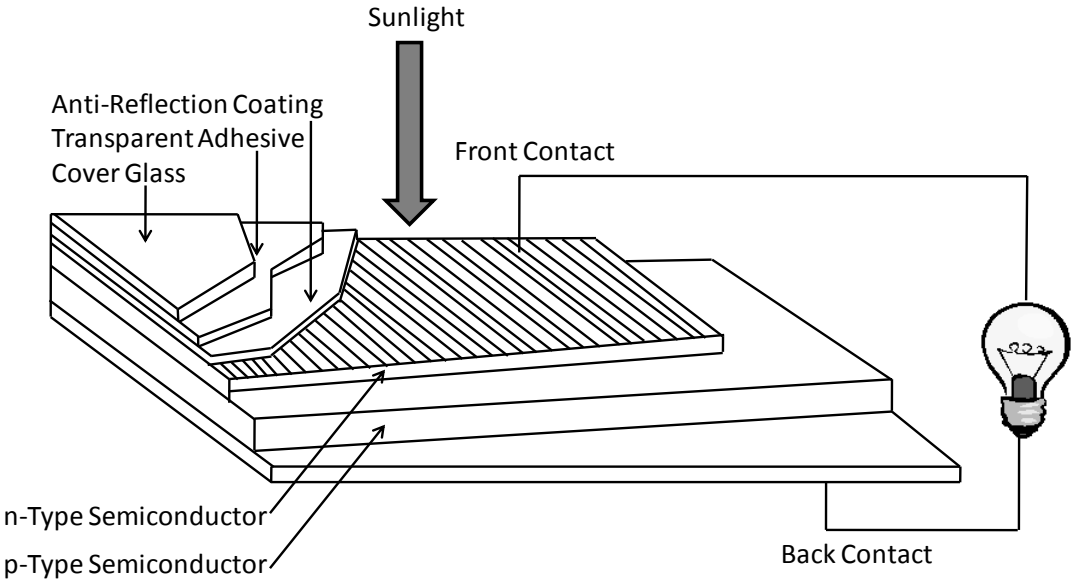

Figure 1. Generic and Common PV Cell.[7]

Each layer serves a specific purpose or purposes. From the top down, the glass cover is used to protect the cell from the elements, such as water and atmospheric gasses that often contaminate and damage the cell resulting in efficiency and lifetime reduction. Transparent adhesives maintain the connection between the cover glass and the cell and often serve an anti-reflective coating to

retain as much solar energy as possible (thereby increasing cell efficiency). Inherently, in silicon materials, the drastic difference in refractive index (RI) between the cover glass and cell creates undesirable scattering. Zinc sulfide with a RI of 2.4 is one of the best transparent anti-reflective materials positioned approximately midpoint between silicon (3.5) and the cover glass (1.5), which aides to minimize scattering losses.[7] Scattering losses have been as high as 30% of the incident light in the absence of anti-reflective coatings.[7]

The front and back contacts facilitate electron flow/circuit connection and are typically composed of silver, aluminum or similar conductive metals. Most cell designs utilize top contacts applied as “fingers” over the cell to minimize shadowing from the contact itself and maximize cell exposure. Fingers are evenly distributed with little spacing, generally 3 mm, as a compromise between losses from higher exciton diffusion length distances and shading/shadowing related losses.[8] Each finger is connected to the circuit via a busbar (Figure 2). Typical designs can shadow up to 10% of the cells surface, decreasing total absorption. Alternative materials used in many new cells utilize transparent or semitransparent metal oxides, such as indium tin oxide for the top contact, as these facilitate full surface contact without a shadowing effect (some small losses in conductivity are noted in the literature).[9]

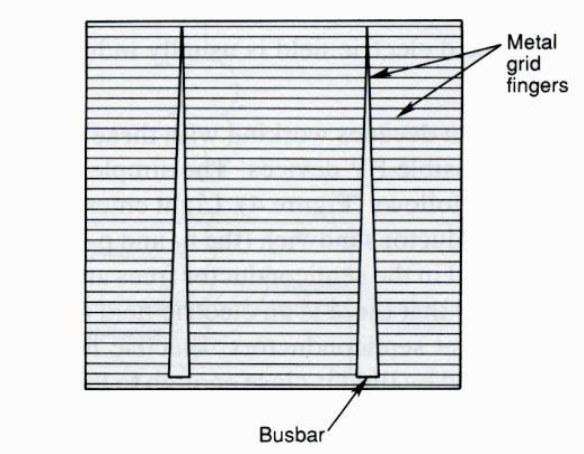

Figure 2. Top Contact Construction.[7]

The doped silicon layers, n (negative) and p (positive) are the cells main components, where the photon to electron function occurs. Electrons from the n-type silicon cross the boundary to the p-type silicon and settle in the "holes" inherently present in the p-type. Thus, the p-type silicon becomes the negatively charged area while the n-type silicon is positively charged. Although, it is important to remember that each layer maintains substantial quantities of the original species in the bulk.[10] The electron accumulation in p-type silicon creates a permanent field potential or voltage at the n-p boundary. The voltage field accelerates electrons, directly proportional in rate (first order) to the strength of the electric field, through the circuit to produce electrical current.[11]

High Efficiency Silicon

Throughout the years, improving solar technology was focused on modifying the silicon used in the cells, such as the efficiency-increasing, single crystal silicon. Improved cost-to-power ratios were achieved by texturing the surfaces for better absorption in combination with thin absorption areas and reflective backing which reflected the unabsorbed light back through the cell.

Single-crystal silicon technology has been further modified to develop polycrystalline and amorphous silicon-based cell designs. Each system has specific advantages and disadvantages. Polycrystalline silicon cells are less expensive to produce than single-crystal silicon but are also less efficient. Polycrystalline silicon is produced by crystallizing liquid silicon inside a mold. As the material crystallizes, it forms granular silicon crystals with highly defined grain boundaries. The grain boundaries serve as lattice defects and become sites for efficiency losses. The grain boundary effects are generally minimized by pacification and controlling crystal growth for structured boundary development. The engineering methods produce vertically elongated crystals, or in a sense, a single crystal with multiple neighboring crystals, which results in longer exciton diffusion lengths than most other technologies. The result produces a higher number of excitons generating current.[7] To date, the most efficient polycrystalline silicon solar cells were reported as 19.8% efficient (power output/photon input).[4]

Amorphous silicon technology also reduces the cost of producing solar cell arrays. Amorphous silicon is prepared by vapor deposition on glass or polymeric substrates and requires much less silicon than other commercial techniques. Unfortunately, the deposition process has a tendency to create defects that reduce the overall cell efficiency. The thin layer techniques do, however, enable amorphous silicon cells for multi-junction solar cells (to be discussed in more detail below). Amorphous silicon cells have achieved efficiencies up to 13%.[12]

Thin Film Solar Cells

Thin film materials offer the advantage of producing light-weight, possibly even semi-flexible solar cells. Weight restrictions are derived from substrate selection where the functional films are deposited via solvent casting and subsequent annealing. The process temperature requirements for annealing restrict the choice of polymeric substrates. Thin film cells utilize many inorganic materials in combination with silicon including copper, indium, sulfur and selenium complexes. The resulting devices are often ideal for dual-junction designs with broader band gap absorption and higher cell efficiency.[13]

Multijunction/Bulk Heterojunction Devices

Multijunction/bulk heterojunction cell designs are focused on maximizing solar radiation absorption and minimizing surface area necessary for optimal energy production. Multijunction or heterojunction devices are very promising for highly efficient PV cells. Multijunction systems, also referred to as cell stacking or stacked cells, use varying layer technology as frequency specific filters. Each layer absorbs certain solar frequency ranges; the lower frequencies (shorter wavelengths) are typically absorbed first due to their higher energy levels. Figure 3 depicts a multijunction system with two dependent cells. Notable and critical, the tunnel diode is produced from two different forms, positive and negative, facilitating higher current production. The common center diode allows each cell to function independently as two separate cells that are wired in series. However, a disadvantage is that series wiring limits current flow to that of the

lower current producing cell, while on the upside increasing the voltage in an additive fashion.[14]

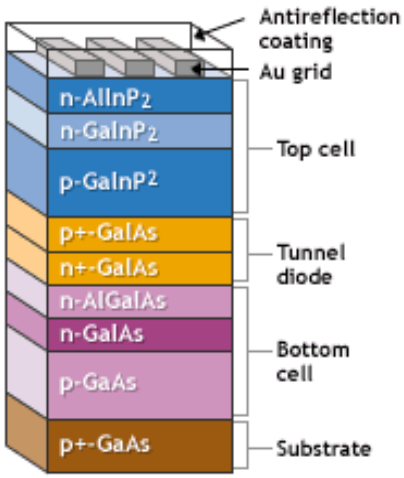

*Figure 3***.** Multijunction Solar Cell.

Bulk heterojunction systems introduce multiple phase separations within the bulk of the cell. The technique increases charge transport and the available surface area for exciton separation. Increased charge transport is directly responsible for increasing photon to electron conversion ratios. The possibility does exist for creating efficiency decreasing charge traps that result in exciton separation in the absence of cell output contribution.[15]

Organic Photovoltaics

Since solar cells were first commercialized, the cost required to produce a single watt of power has decreased dramatically, along with substantial decreases in the required area for similar output.[5, 7] The average cost to produce solar power in the United States was $3.00 per watt in 2002.[5] Even with the required capital investment (substantial price), solar power provides a return on investment (ROI) within a 25-30 year lifetime while supplying consistent power

generation and requiring only minimal maintenance over the same timeframe. In contrast to conventional PV technology, OPV are more appealing due to fabrication ease. Generically, functional thin films are commonly produced using large scale established technology such as roll-to-roll printing, inkjet application for liquid crystal display (high definition TVs) and specialty casting techniques for organic wiring boards.[16] The commonly proposed scenario is one in which polymeric/organic solar cells could be printed as flexible sheets, transported, stored, and then installed while being cut as required for the final use (much like current metal roofing or even traditional asphalt shingles), greatly reducing processing cost and broadening solar power applicability. Functional windows, spray-on application techniques and transparent versions are all currently being investigated in various research phases.[17]

The OPV history is more concise than traditional cell technology, as it is an emerging research area. Two distinct classes of OPV have been established already: 1) molecular and 2) polymeric. In general, organic systems (also known as donor/acceptor cells) employ the same techniques as silicon cells with a few critical differences. The primary difference is the operating mechanism. Unlike the traditional silicon systems which produce current via bulk process(es), organic systems operate by an interfacial current creation process.

The term interfacial process is best described in a bulk heterojunction system that exhibits distinct phase separation (material differences in morphology on a relatively small, often nanometer scale), and in the most efficient systems, many phases within a cell. In organic systems, unlike

inorganic cells, the built-in electric field does not separate the exciton. Therefore, a photoinduced transfer reaction between the donor and acceptor interface/phases is necessary to separate the excitons into respective electrons and electron holes. The phenomenon leads to a high electron concentration in one phase, and a high hole concentration in the other, allowing the minority carrier (hole) concentration to be considered insignificant for the purpose of theoretical efficiency calculations.[18] The research focus then shifts almost solely to charge transport to the interface, and it is by definition the limiting process/effect on quantum efficiency.

The absorption of photon energy is obviously a key component of a working PV cell. Each frequency specific photon possesses energy as dictated by the Planck's relationship. The PV material absorbs wavelength specific energy depending upon spectral output, solar cell structure and individual component responses to solar energy. Upon photon absorption, an electron in the bonding orbital or highest occupied molecular orbital (HOMO) is promoted to the antibonding orbital or lowest unoccupied molecular orbital (LUMO). The difference between these two states is known as the energy band gap. This process is specific to OPVs, since charge separation occurs at the interface, current is only generated if photon absorption is within the exciton diffusion length. In other words exciton generation must be within a distance from the interface that is less than the exciton diffusion length. Exciton diffusion lengths have been measured as short as 1 nm and up to 40 nm in varying investigations, whereas OPVs typically produce shorter diffusion lengths and these are

attributed directly to the ratio of material defects versus the electron hole recombination kinetics.[19]

The process for a material to be useful as an organic semiconductor (OPV materials) is quite complex. Once it absorbs a photon and generates an exciton, it then undergoes one of the following three main processes:

1) **non-radiative recombination**, whereby an exciton is not matched with the surrounding, and results in energy transfer from electronic excitation to vibrational and rotational energy,
2) **radiative loss** resulting in photoluminescence, or
3) **exciton charge stabilization** that enables material electron flow to the electrodes, creating electrical current.[14]

Solar power efficiency can be gained via minimization and/or absence of the first two processes and maximization of exciton charge stabilization. Thereby, each is critical for facilitating PV effects in organic semiconductors. Figure 4 illustrates the events dictated in these three steps. In this figure note that, in order for efficient charge transfer to occur, the LUMO of the acceptor material must be lower than the LUMO of the donor material. The figure also summarizes the processes thought to dictate each of the possible loss mechanisms throughout the charge generation process.

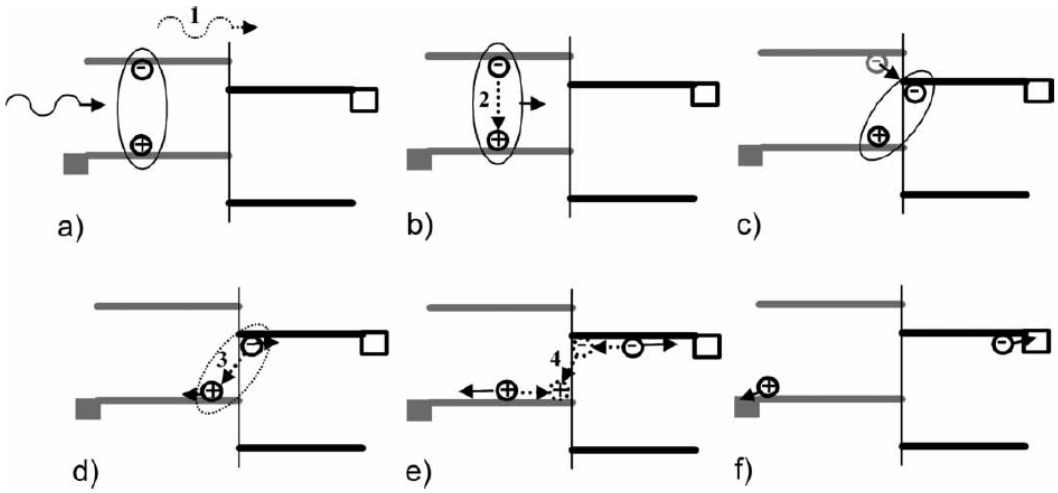

Figure 4. Charge diagram for the potential processes involved in photovoltaic cells: a) absorption of a photon resulting in an exciton, b) diffusion of the exciton to the donor acceptor interface, c) electron transfer from donor LUMO to acceptor LUMO, d) dissociation of the bound electron hole pair into free carriers, e) transport of the carriers to their respective electrodes, f) collection of charges. The losses occurring here are shown by 1) non absorbed photons, 2) exciton decay, 3) recombination of the bound pair, 4) bimolecular recombination.[20]

The donor phase of an OPV is generally responsible for photon absorption and exciton creation, although it is possible for donor and acceptor molecules to absorb photons. A donor material by definition requires particular wavelength(s) absorption in combination with higher HOMO and LUMO energy levels than the chosen acceptor. Band gap energy difference is critical and donor-acceptor pairs are selected on these principles.

The OPV acceptor phase must have the ability to accommodate and rapidly transfer additional electrons. The most common acceptor phase OPV molecules are based on Buckminster Fullerene (C_{60}). C_{60} has the capability to accommodate up to six extra electrons when un-functionalized, but unfortunately remains poorly compatible in an unmodified state. Following that logic, a single functional group is often added for greater morphological and solubility control,

thereby reducing the molecule's electron capacity slightly, but drastically improving dispersability/compatibility in organic/polymeric materials. Critical for acceptor molecules/phases are lower LUMO in comparison with the donor molecules/phases; again it is the electron transfer between the donor phase LUMO to the acceptor phase LUMO that allows for electron flow.

Conductive Polymers

Conductive polymers are characterized by conjugated carbon double bonds in the polymer main chain. The alternation of single and double bonds creates extended lengths of delocalized π (pi) electrons thereby, more easily stabilizing charges, facilitating charge transfer, and imparting conductivity. The long range conjugation reduces the energy band gap between the HOMO and LUMO to an accessible range in the visible spectrum (1.5-3 eV), much lower than that associated with non-conjugated polymers (7-8 eV).[14, 21] Common practice for conductive polymers is to "dope" them; the process often results in a 10 order of magnitude increase in conductivity.[21, 22]

Trans-polyacetylene is considered the simplest conductive polymer backbone and was the first to be discovered.[22, 23] The trans-polyacetylene structure consists of a quasi-one dimensional structure, held together by trigonal planar σ-orbitals (sp^2) between the carbon atoms of the backbone. The resulting structure has been described as a delocalized electron cloud with a periodic alternating density, and also described as a system of alternating single and double bonds. As mentioned previously, these delocalized electrons form a

network that allows conjugated polymers to stabilize a charge and facilitate conductivity in doped systems.[14]

Since the first conductive polymers were discovered a large number of critical research advancements have identified and established many other classes of conductive polymers. The main categories and most studied are the previously mentioned polyacetylene, as well as, poly(p-phenylene vinylene), polyaniline, polypyrrole, poly(p-phenylene sulfide) and polythiophenes. Each of these polymers belongs to a general class and each has unique properties, often very different from one another, based on its structure.

Poly(p-phenylene vinylene)

Poly(*p*-phenylene vinylene) (PPV) has a structure that consists of alternating phenyl rings and double bonds, and the rings and double bonds are always separated by only one single bond in order to maintain conjugation. In comparison to polyacetylene, PPVs exhibit increased electron density that is attributed to the phenyl ring inclusion in the polymer backbone. The phenyl ring establishes higher rigidity by adding a level of planarity to the system that thereby drives higher crystallinity. PPV is intractable in most solvents; however, it can easily be dispersed and crystalline films formed through casting of the dispersed polymer. In order to further manipulate properties and increase crystallinity and conductivity, PPV is commonly modified with morphology/solubility modifying side-groups, as well as, doped with halogen species or acids.

PPV conductivity levels vary over a large range and are directly dependent upon dopant level or type, crystallinity and morphological alignment.

Undoped, unsubstituted PPV is a diamagnetic material that has very low intrinsic electrical conductivity, on the order of 10^{-13} S/cm.[24] Once the system is doped it can reach conductivities reported between 10^{-3} S/cm to 100 S/cm, for iodine and H_2SO_4 as dopants, respectively.[24] PPV is also capable of being drawn, similar to fiber processing, to a draw ratio up to 10; higher drawing ratios increase alignment and therefore conductivity. Side-chain-modified PPVs increase the dopant ability to oxidize the PPV chain and drive towards higher conductivity in most cases; however, there is a side chain length limit dictated by chain-to-chain packing efficiency, i.e., larger/longer side chains reduce conductivity by decreasing packing efficiency and interchain hopping of charge carriers.[25]

Polyaniline

Polyaniline (PANI) is similar to PPV in that the main conjugation points are phenyl rings; however, PANI introduces a heteroatom, i.e., nitrogen, in the place of the double bond to separate the phenyl rings. PANI is found in many forms; however the only conducting version is the emaraldine salt, which is named for its green color. The conductivities of PANI can range anywhere from 10^{-8} to 10^{2} S/cm.[26] Very similarly to PPV, the conductivity of PANI can be drastically affected by the dopant level or type, film formation, and substitution.

An interesting feature of PANI is that the multiple polymerization methods afford a variety of supramolecular structures and often skip the difficult/narrow solubility related issues by depositing polymer directly as needed. Thereby, researchers are able to use the polymerization process to tune supramolecular structures to

the specific application. The figures below show a few of the structures obtained for various polymerization techniques.

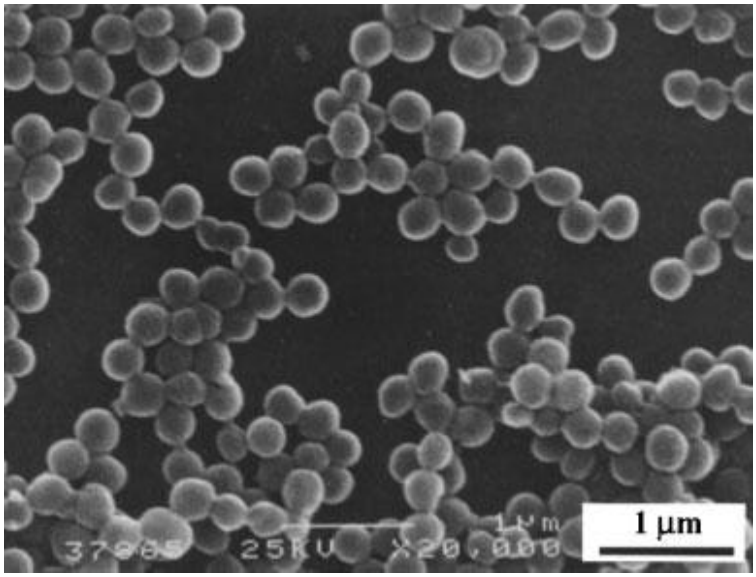

Figure 5. Colloidal PANI particles stabilized with hydroxypropylcellulose.[27]

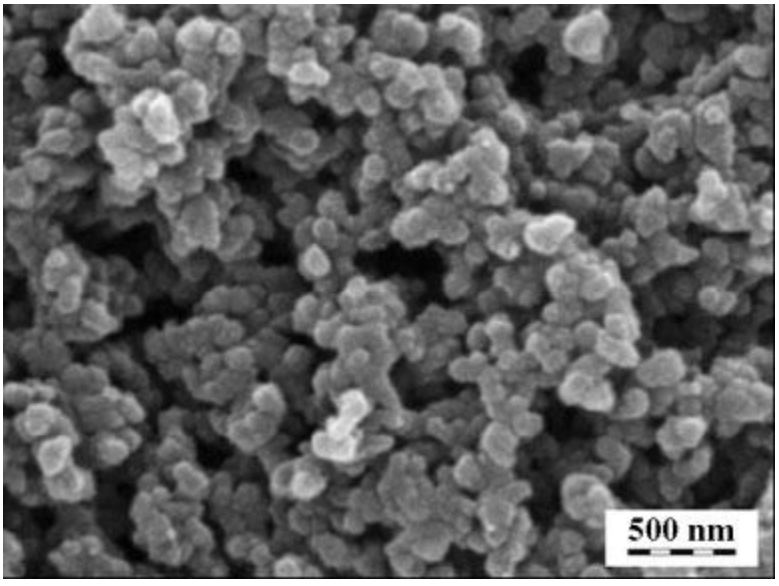

Figure 6. Granular structure of a PANI precipitate obtained in a standard polymerization.[28]

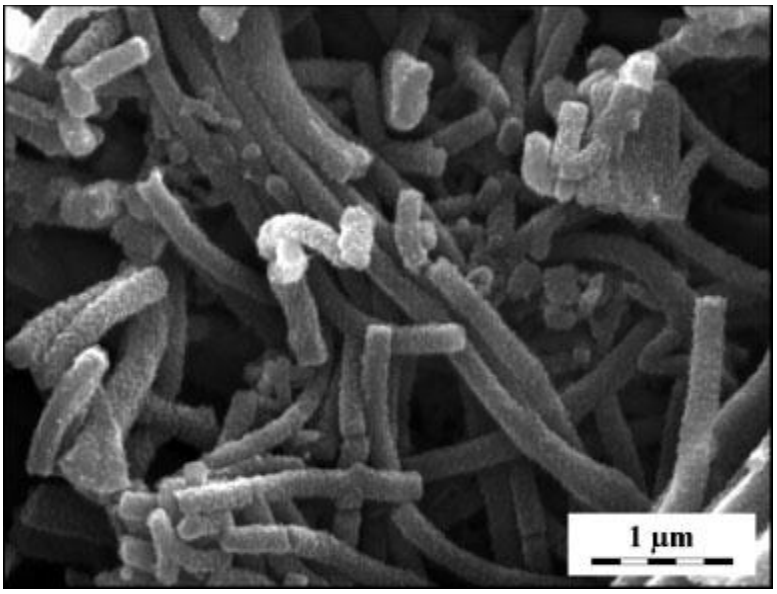

Figure 7. PANI nanotubes obtained by the oxidation of aniline with ammonium peroxydisulfate in acetic acid at -4º C.[29]

Polypyrrole

Polypyrrole (PPy) consists of five-membered heterocyclic rings (nitrogen) and possess good chemical stability, low oxidative potential, high electrical conductivity, and little to no toxicity.[30] Structurally, polypyrrole combines the ideas of PANI into a single ring structure, allowing for easy doping as well as increased electron density. PPy was one of the first conductive polymers to show high conductivity without dopant present (1 S/cm).[31] Similarly to that of PANI, PPy has recently been shown to possess the ability to alter hierarchical structure based on the synthetic techniques that is used to create the polymer. Figure 8 below illustrates an example structure of interwoven PPy wires.

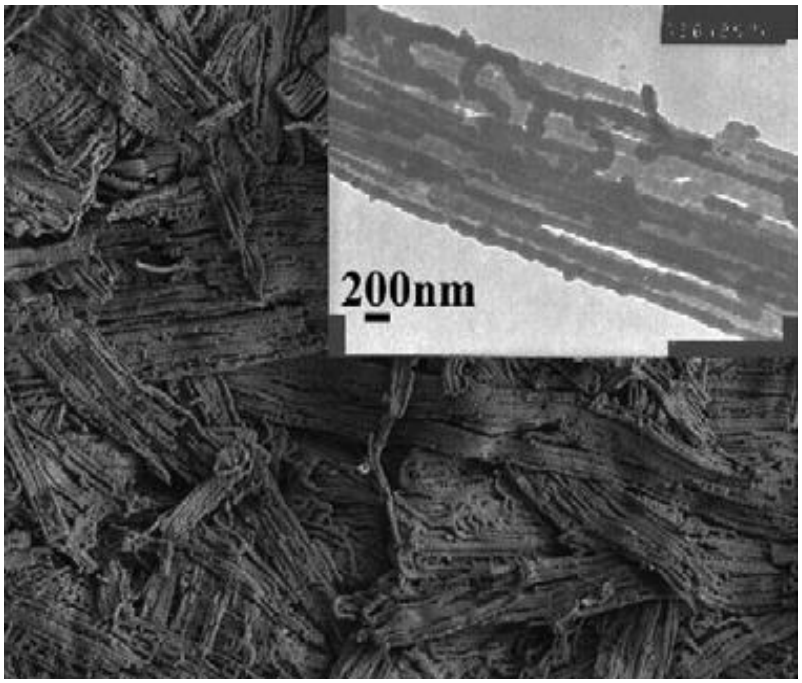

Figure 8. SEM with inset TEM image of Polypyrrole.[30]

Poly(p-phenylene sulfide)

Poly(*p*-phenylene sulfide) (PPS) is very similar in structure to PANI, however, the nitrogen species is replaced with a sulfide. PPS in its original state is an insulating material and is not conductive. The conductive form is generated by oxidation or use of dopants. The undoped, non-oxidized version is completely intractable in all solvent systems at ambient temperatures; however, as with the previous conductive polymers modification to the ring structure in the form of side chains will increase solubility. PPS does however have the advantage of high thermal stability, which allows it to be processed up to approximately 220ºC before degradation occurs. This high stability allows for molding and execution of high tolerance machining.[32] PPS is commonly used in connectors for electrical or optical fiber cables, print wiring boards, and electronic encapsultants.

Polythiophenes

Since their discovery in 1977,[33] conjugated polymeric systems have continued to prove useful and interesting due to their potential in diverse applications. However, controlling the conductivity range of π-conjugated systems is a challenge, as it is a function of structural properties such as regioregularity, molecular weight, molecular weight polydispersity, identity of terminal groups and morphology. Among conjugated polymers, and the last to be discussed herein, polythiophenes (PTs) are preferred for many organic electronic applications due to the base polymer's 1) relatively high conductivity, 2) environmental stability, and 3) tunable band gaps with varying side groups. PTs most closely resemble the PPy polymers discussed earlier; however, the nitrogen species is replaced with sulfur. Polythiophene's rise to prominence in the conductive polymer field was in many ways driven by its diverse optical properties. Small changes in the side chains resulted in drastically different colors when exposed to solvent, temperature, or outside electrical current.

The first PTs, prepared via chemical polymerization of unsubstituted thiophenes through 2,5-coupling, were highly conductive, environmentally stable polymers that were insoluble in most common solvents.[34, 35] Poly(3-alkylthiophene)s (P3ATs) were the first solvent soluble conductive PTs to be synthesized.[36] Subsequent developments led to the synthesis of regioregular (rr) P3ATs that are highly conductive, more easily processed, and environmentally stable.[37, 38] While many methods have been developed to synthesize soluble PTs, techniques that specifically yield regioregular polymers are more valuable,

as increased chain order typically correlates to higher chain packing density and higher conductivity.[39] Such synthetic techniques include, but are not limited to, the Grignard Metathesis (GRIM)[40], McCullough[41], and Rieke[42] methods. All three methods proceed through transition metal catalyzed cross-coupling reactions. While the GRIM method allows ambient or reflux temperature processes to produce rrP3ATs, the McCullough and Rieke methods require cryogenic temperatures.[43, 44, 45] The Rieke method also requires highly reactive "Rieke Zinc" to produce rrP3ATs. Each of these methods seeks optimum control over molecular weight, molecular weight distribution, end group functionality and regioregularity as a means for improved conjugated polymer utility. A more detailed examination of synthetic techniques will be discussed in later chapters as this polymer backbone is the focus of this research.

Conductive Copolymers

While the above mentioned conductive polymers make up the majority of the polymers used in studies involving organic photovoltaics, there exists a substantial number of copolymer systems which are also relevant. Many of these polymers are based on the systems mentioned above, but possess conductive side chains or a combination of variously substituted monomers. In general, the main goals of researchers synthesizing copolymer systems are to facilitate synergistic combinations between crystallization, solubility, band gap absorption, and material conductivity toward polymers with tuned properties for more efficient OPV systems. Some copolymer systems utilize alternating donor and acceptor moieties within the backbone for fine tuning the polymer band gap,

while simultaneously improving the planarity of the system which has a major effect on the charge carrier mobility. The main copolymer systems that are used for OPVs can be found in reviews by Martin et al. and Zhu.[46, 47]

Buckminster Fullerene

While not necessarily fitting directly into the conductive polymer category, fullerenes are often important parts of conductive polymer systems, especially those used in OPVs. Carbon atoms in fullerene molecules are located at the vertices of regular hexagons and pentagons, which cover the spherical surface in a regular manner. The most studied and touted molecule of the fullerene family is C_{60}, Buckminster Fullerene, whose structure is a regular, truncated icosahedron. The molecule surface is constructed from twenty regular hexagons and twelve regular pentagons such that each pentagon is adjacent only to hexagons, whereas each hexagon is adjacent to three pentagons and three hexagons alternately. The fullerene family also includes other molecules such as C_{70}, C_{76}, C_{78} and C_{84} that are distinguished by a lower symmetry and larger number of hexagons on the surface. Thus, the fullerenes form a unique class of molecules having a closed two-dimensional structure.[48]

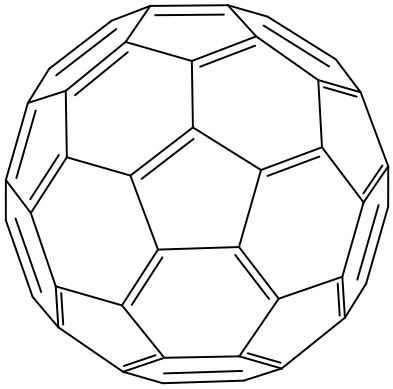

Figure 9. Buckminster Fullerene, C_{60}.

Scale and Material Specific Locations for Better Morphology Control and Matching with Internal Conversion Efficiency

The Need for Morphology Type and Size Control

Typically, a polymer (most often conducting) behaving as an electron donor (D) is blended with an electron acceptor (A), usually a fullerene, to achieve a bulk heterojunction (BHJ) structure. The polymer plays the key roles of absorbing light, creating excitons, charge separation, and the subsequent transport of holes to the anode. Further improvements in device performance will require materials harvesting more light from the solar flux and the development of well-defined morphologies to allow effective charge separation and transport. Simply blending D and A materials requires nanomorphology to provide suitable interfaces/interfacial area for exciton dissociation. Furthermore, the D and A units must segregate into size domains that are homogeneous on the order of the exciton diffusion length (1-100 nm). In the meantime, they must form a nanoscale interpenetrating phase possessing continuous paths between the electrodes for efficient charge transport.[49] As can be imagined it is difficult to simultaneously achieve a high surface area of contact between D and A phases

at a sufficiently small size scale while also achieving maximum possible contact with electrodes that do not absorb or reflect incident light.

Theoretical calculations have shown that increased order (morphological order associated with interfacial area) of the D and A materials will increase the overall cell efficiency. Figure 10 shows the progression of OPV cells, with Figure 10(c) illustrating what is currently considered state-of-the-art. Figure 10(d) shows an ordered heterojunction that possesses controlled contacts and spatial order.[50] In addition, Monte Carlo simulations suggest that feature or domain sizes of approximately 10 nm generate the ideal internal quantum efficiency for both a disordered bulk heterojunction and an ordered heterojunction.[51] These simulations also predict a photon conversion efficiency increase from approximately 1% up to 5% when an optimized ordered morphology is achieved.

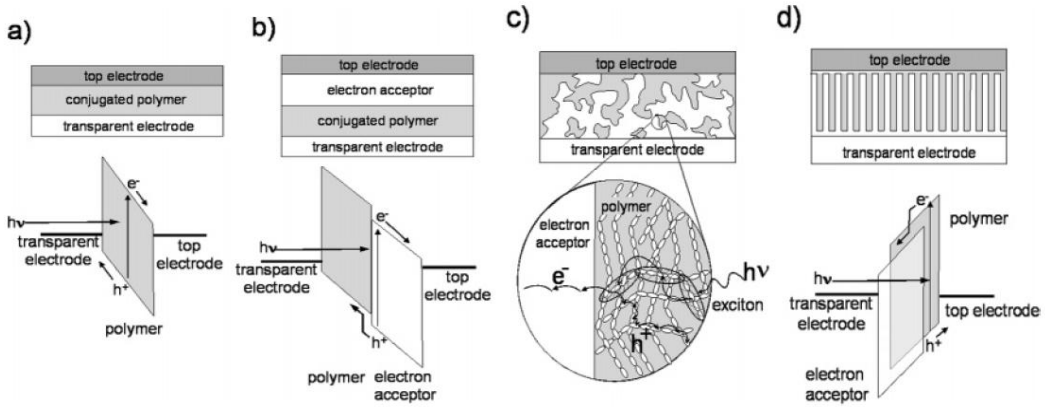

Figure 10. Progression of morphology control in organic photovoltaics.(50)

Methods of Control

A practical method for achieving morphology control is to spin coat nanoparticles from an inhomogeneous solution. Nanoparticles have been shown to result in morphology domains in the range of 30 to 300 nm.[52] By using

nanolithography, molds and templates can be employed to generate desired morphologies. Nanolithography offers morphology control approaching 10 nm and repeatable results have been achieved from 30 to 65 nm.[53, 54] Electrostatic layer-by-layer (ELBL) deposition enables varying domain sizes by changing the polyanions and polycations used in the deposition, e.g., dye-sensitized solar cells exhibit control from 20 to 40 nm.[55, 56] Zeolites also offer a high degree of control of domain separation down to 6.5 nm, however, the efficiency is less dependent on domain size as it is dependent upon grain boundaries that are created.[57]

Directly relevant to this dissertation are methods for morphology control via block copolymers and block copolymer microphase separation. This section will discuss domain shape and size control resulting from previously developed and studied block copolymer systems.

Controlled micro- or nano-phase separation from block copolymers is facilitated via block-to-block incompatibility through varying block lengths, length ratios, annealing processes and the subtle but critical degree of block compatibility. Figure 11 summarizes the more common and well-studied block copolymer morphologies, many of which have yet to be achieved with a single conductive block, much less, with two blocks each dedicated to independent donor acceptor functions. For the purposes of this research, morphologies containing rod-like structures are thought to be most favorable for OPVs as they combine thorough absorption and high interfacial surface area with excellent charge transportability and facilitate electron/hole transfer to the appropriate electrode. The typical thicknesses for OPVs allow rod-like morphologies to

create charge transfer pathways that traverse an entire device and promote higher efficiencies at each step in the process. Albeit possible, other morphologies are thought to be less desirable as they inherently introduce "charge traps" as interfaces become physically separated. In such instances, PV electrical current cannot be generated due to the lack of a continuous charge transport pathway to the electrode.

Figure 11. Common morphologies of block copolymers.

A critical distinction between coil-coil and rod-coil block copolymers are necessary as most conductive polymers are rod like in behavior and these materials drive different and critical morphological results. To date, the block copolymer morphologies studied in all areas of research have mostly been coil-coil polymers, and the behavior is well understood and thoroughly studied. Rod-coil polymers, such as the ones of interest in this research, give rise to new available morphologies such as zig-zag, bi-layer, interdigitation, and wavy-lamellar. SEM images of these structures can be seen in Figure 12.[42] With these systems, the morphological domains can range from a few nanometers to 1 micron, depending strongly on the volume fraction and molecular weight of the rod polymer in combination with the solubility/crystallization competition.[32] It has been shown that molecular weights on the order of or less than the persistence length of the rod polymer generate fibrillar morphology.[58, 59] It has also been

shown that the relative block lengths play significant roles in the packing and ordering of the rod segments.[60]

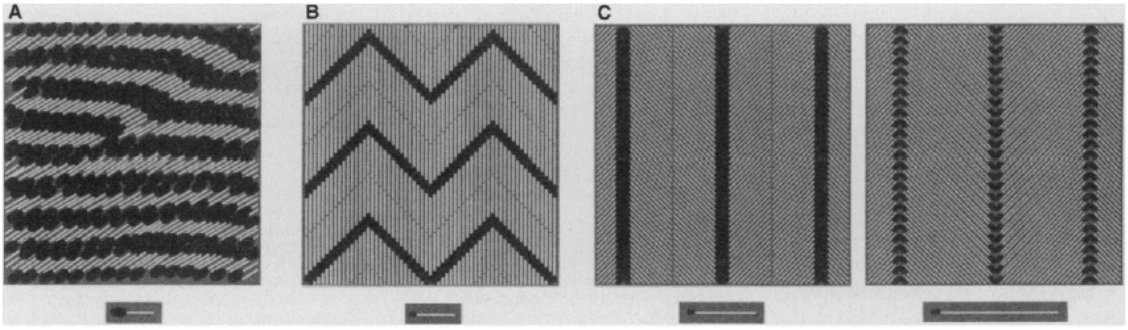

Figure 12. Representative rod-coil morphologies: (a) wavy-lamellar; (b) bi-layer and interdigitating chains.[42]

In 1984, Mahmoud Aldissi synthesized one of the first examples of conductive block copolymers (thought to be rod-coil) by synthesizing poly(acetylene)-poly(isoprene) via anionic polymerization of isoprene to desired molecular weights, followed by a catalyst exchange that lasted several days.[43] Upon introduction of acetylene, poly(acetylene) blocks formed instantaneously. The resulting block copolymer maintained reasonable conductivity after doping, exhibiting conductivities between 1-10 S/cm depending on the coil block molecular weight. The research established the potential of using a rod-coil block combination and how shifting the polymer-polymer interaction parameter facilitated microphase separation and yet maintained conductivity.[43]

The next example of a soluble conductive block containing block copolymer was reported in 1989 by Bernard Francois who synthesized polystyrene-polyparaphenylene (PS-PPP) via aromatization of polystyrene-poly(1,3-cyclohexadiene). The polymer contained conductive block lengths on the order of 10 to 11 repeat units (quantifiably below the persistence length of

rigid polymers which does not allow narrow domain spacing) that were separated by defects, and exhibited conductivities of 0.1 S/cm. The low conductivities were attributed to the relatively large polystyrene segments (30,000 g/mole) as well as the frequency of defects and disconnected regions in the conductive segment.[61] Fully conductive block copolymers have been reported, but were generally characterized by lack of solubility in organic solvents.[62, 63, 64, 65] Conductive block copolymers based on polypyrrole,[66, 67] polyaniline[68, 69] and polythiophenes[70, 71] have also been synthesized, but the desired objectives of maintaining solubility, ease of processability and high conductivity continues to be elusive.

In 2004, van der Veen *et al.* synthesized block copolymers containing poly(1,4-phenylenevinylene) (PPV) and a second coil block of various monomers with latent functionality for subsequent grafting with Buckminster Fullerene.[72] However, the reported lack of control over each block molecular weight and the blocks individual polydispersity resulted in poor morphological control in the solid state films.

In 1992, McCullough *et al.* successfully polymerized 3-alkyl thiophenes and subsequently modified the synthesis procedure to facilitate better control over polymer molecular weight polydispersity.[73] The new method, known as Grignard Metathesis (GRIM), provided *in situ* functionalization of low PDI conductive blocks, and the subsequent growth of a second coil block polymer segment.[74] Using this method, Richard *et al.* synthesized a poly-3-hexylthiophene-block-acrylate/fullerene copolymer; however, the low and limiting

molecular weight of the conductive rod-like block did not permit self-assembly into the expected morphologies.[58]

The research described herein is focused on achieving an all-in-one donor-acceptor block copolymer with intended phase separation and control over domain spacing and molecular weights within each domain to facilitate a fundamental study of parameters yet unattained in the open literature. These parameters are collectively and critically important to further understanding whether and how increasing efficiency for OPV materials is possible. Specifically, tuning material photon absorption characteristics, defined and regular morphology (to facilitate shorter exciton diffusion lengths associated with OPVs), rapid charge transfer to minimize recombination, ease of application and material lifetime are of main interest. It is not possible to focus on all of these simultaneously; however, the prospect of creating fully organic solar cells is exciting for many reasons. This includes the potential to yield completely flexible surfaces, application to virtually any substrate and material durability not currently possible with silicon cells.

The research presented herein, in a context of the overview above is focused on the synthesis of novel block copolymers containing all the necessary donor and acceptor materials in a single molecule. The donor block is a conductive polymer with tunable photon absorption characteristics (via side chain substitution) and the other block possesses acceptor characteristics. The block copolymer morphology is controlled by varying block lengths, composition, and via annealing or solvent specific phase separation. Once synthesized, the all-in-

one block copolymer should provide an interesting focal point to study OPV while optimizing absorption, charge transfer, exciton diffusion length and PV current production. The morphological control possible through tailored block copolymer design in an all-in-one molecule provides an almost untapped potential to harness PV for power generation.

The focus of this research was driven by the main hypothesis that gains in OPV efficiency can be directly linked to the size and scale of morphology between donor and acceptor materials. This desired morphology matches the appropriate size scale for fully functionalized block copolymers. In order to validate this hypothesis, we utilized similar molecular features and the appropriate synthetic techniques to design and control a specific absorption wavelength. With absorption in mind, a constant focus on attempting to simplify the resulting material morphology through controlled domain/phase separation and thereby creating an entire PV device from a single polymer, albeit complex in synthesis and design, simple in overall concept.

REFERENCES

1. Kelly, H. *In Renewable Energy.* Island Press: Washington, 1993.
2. Brabec, C. J., Padinger, F.; Jummelene, J.C.; Janssen, R. A.; Saricifitci, N. S. *Synthetic Metals* **1999**.
3. Smith, W. *Nature*, **1873,** 7, 303.
4. Sun, S. S.; Sariciftci, N. S. *Organic Photovoltaics, Mechanisms, Materials, and Devices.* Taylor and Francis Group: Boca Raton, 2005.
5. Surek, T. *Progress in U.S. Photovoltaics: Looking Back 30 years and Looking Ahead 20.*National Renewable Energy Laboratory, 1996.
6. Green, M. *Physica E.* **2002,** 14, 11-17.
7. Zweibel, K. *Harnessing Solar Power: The Photovoltaics Challenge.* Plenum Press: New York, 1990.
8. Wenham, S. R.; Green, M. A. *Buried Contact Solar Cell.* February 23, 1988, *4726850*.
9. Zirngibl, M.; Hu, J.; Sachot, R.; Llegems, M. *Applied Physics Letter.* **1989,** 54(21-22), 2076-2078.
10. Gibbons, J. F. *Semiconductor p-n junction solar cell and method of manufacture.* USA: January 4, 1977, *4726850*.
11. Bierman, A. *Physical Review.* **1963,** 130(6), 2266-2270.
12. Guha, S.; Yang, J.; Banerjee, A. *Progress in Photovoltaic Research Applications.* **2000,** 8, 141-150.
13. Jager-Waldau, A. *Solar Energy.* **2004,** 77, 667-678.

14. Brabec, C. *Organic Photovoltaics: Concepts and Realization.* s.l. : Springer-Verlag: Berlin, 2003.
15. Hoppe, H.; Sacriciftci, N. S. *Journal of Materials Chemistry.* **2006,** 16, 45-61.
16. Chason, M.; Gamota, D. R.; Brazis, J. R.; Paul, W.; Kalyanasundaram, K.; Zhang, J.; Lian, K. K.; Croswell, R. *MRS Bulletin.* **2006,** 31, 471-475.
17. Bonasia, J. *Solar Powered Buildings Again Hot.* July 11, 2006, Investors Business Daily.
18. Gregg, B. A. *MRS Bulletin.* **2005,** 30, 20-22.
19. Forrest, S. R. *MRS Bulletin.* **2005,** 30, 28-32.
20. Kroon, R.; Lenes, M.; Hummelen, J. C.; Blom, P. W. M.; Boer, B. *Polymer Reviews.* **2008,** 48, 531-582.
21. Kumar, D.; Sharma, R. C. *European Polymer Journal.* **1998,** 34(8), 1053-1060.
22. Rupprecht, L. and Epstein, A. J. *Conductive Polymers & Plastics.*, Plastics Design Library, 1999. pp. 1-8.
23. Boer, B.; Stalmach, U.; Hutten, P. F.; Melzer, C.; Krasnikov, V. V.; Hadziioannou, G. *Polymer.* **2001,** 42, 9097-9109.
24. Skotheim, T. A. *Handbook of Conducting Polymers.* 2nd Edition. CRC Press: New York, 1997. pp. 343-351.
25. Granier, T.; Thomas, E. L.; Gagnon, D. R. ; Karasz, F. E.; Lenz, R. W. *Journal of Polymer Science, Part B: Polymer Physics.* **1986,** 24, 2793-2804.
26. Sapurina, I.; Stejskal, J. *Polymer International.* **2008,** 57, 1295-1325.

27. Stejskal, J. ; Spirkova, M.; Riede, A,; Helmstedt, M.; Mokreva, P.; Prokes, J. *Polymer.* **1999,** 40, 2487-2492.

28. Stejskal, J.; Gilbert, R. G. *Pure and Applied Chemistry.* **2002,** 74, 857-867.

29. Stejskal, J.; Kratochvil, P. Langmuir, **1996,** 12, 3389-3392.

30. Han, Y.; Qing, X.; Ye, S.; Lu, Y. *Synthetic metals.* **2010,** 160(11-12), 1159-1166.

31. McNeill, R.; Siudak, R.; Wardlaw, J. H.; Weiss, D. E. *Austrailian Jouranl of Chemistry.* **1963,** 16(663), 1056-1075.

32. Kumar, N.; Shukla, S. K.; Tandon, P.; Gupta, V. D. *Journal of Polymer Science Part B: Polymer Physics.* **2009,** 47(23), 2353-2367.

33. Shirakawa, H.; Louis, E. J.; MacDiarmid, A. G.; Chiang, C. K.; Heeger, A, J. *Journal of American Chemical Society, Chemical Communications*. **1977,** 16, 578-580.

34. Yamamoto, T.; Sanechika, K.; Yamamoto, A. *Journal of Polymer Science, Polymer Letters Edition.* **1980,** 18, 9-12.

35. Lin, J. W. P.; Dudek, L.. P. *Journal of Polymer Science, Polymer Chemistry Edition.* **1980,** 18, 2869-2873.

36. Elsenbaumer, R. L.; Jen, K. Y.; Oboodi, R. *Synthetic Metals.* **1986**, 15, 19-174.

37. McCullough, R. D.; Lowe, R. D. *Journal of American Chemical Society, Chemical Communications.* **1992,** 1, 70-72.

38. Chen, T. A.; Wu, Z.; Rieke, R. D. *Journal of American Chemical Society.* **1995,** 117, 233-244.

39. McCullough, R. D.; Williams, S. P.; Tristram-Nagle, S.; Jayaraman, M.; Ewbank, P. C.; Miller, L. *Synthetic Metals.* **1995,** 69, 279-282.

40. Loewe, R. S.; Khersonsky, S. M.; McCullough, R. D. *Advanced Materials.* **1999,** 11, 250-253.

41. McCullough, R. D.; Williams, S. P. *Journal of American Chemical Society*, **1993,** 115, 11608-11609.

42. Chen, T. A.; Rieke, R. D. *Journal of American Chemical Society.* **1992,** 114, 10087-10088.

43. Aldissi, M. *Journal of the Chemical Society: Chemical Communications.* **1984,** 805, 1347-1348.

44. Smith, B.; Kochi, J. K. *Journal of Organometallic Chemistry.* **1980,** 198, 199-214.

45. Ozawa, F.; Hidaka, T.; Yamamoto, T.; Yamamoto A. *Journal of Organometallic Chemistry.* **1987,** 330, 253-263.

46. Delgado, J.L.; Bouit, P-A. ; Filippone, s. ; Herranz, M. A. ; Martin, N. *Chemical Communications.* **2010,** 46, 4853-4865.

47. Zhan, X.; Zhu, D. *Polymer Chemistry.* **2010,** 1, 409-419.

48. Bezmel'nitsyn, V. N.; Eletskii, A. V.; Okun', M. V. *Physics-Uspekhi.* **1998,** 41(11), 1091-1114.

49. Chan, S. H.; Hsiao, Y. S.; Hung, L. I.; Hwang, G. W.; Chen, H. L.; Ting, C.; Chen, C. P. *Macromolecules.* **2010,** 43, 3399-3405.

50. Coakley, K..; McGehee, M. D. *Chemistry of Materials.***2004,** 16, 4533-4542.

51. Meng, L.; Shang, Y.; Li, Q.; Li, Y.; Zhan, X.; Shuai, Z.; Kimber, R.; Walker, A. B. *Journal of Physical Chemistry B.* **2010,** 114, 36-41.

52. Kietzke, T.; Stiller, B.; Landfester, K.; Montenegro, R.; Neher, D. *Synthetic Metals.* **2005,** 152(1-3), 101-104.

53. Kim, C.; Shtein, M.; Forrest, S. *Applied Phyisics Letters.* **2002,** 80(21), 4051-4053.

54. Williams, S.; Hampton, M.; Gowrishankar, V.; Ding, I. K.; Templeton, J.; Samulski, E.; DeSimone, J.; McGehee, M. *Chemistry of Materials.* **2008,** 20, 5229-5234.

55. He, J. A..; Mosurkal, R.; Samuelson, L.; Li, L.;Kumar, J. *Langmuir.* **2003,** 19, 2169-2174.

56. Zhao, L.; Ma, T.; Bai, J.; Lu, G.; Li, C.; Shi, G. *Langmuir.* **2008,** 24, 4380-4387.

57. Atienzar, P.; Valencia, S.; Corma, A.; Garcia, H. *Chemical PhysChem*, **2007,** 8(7), 1115-1119.

58. Richard, F.; Brochon, C.; Leclerc, N.; Exhard, D.; Heiser, T.; Hadziioannou, G. *Macromolecular Rapid Communications.* **2008,** 29, 885-891.

59. Iovu, M. ; Craley, R.; Jefferies-El, M.; Krankowski, A.; Zhang, R.; Kowalewski, T.; McCullough, R. *Macromolecules.* **2007,** 40(14), 4732-4735.

60. Olsen, B.; Sagalman, R. *Macromolecules*, **2005,** 38, 10127-10137.

61. Zhong, F.; Francois, B. *Synthetic Metals.* **1989,** 29, E35-E40.

62. Kempf, S.; Rotter, H. W.; Magonov, S. N.; Gronski, W.; Cantow, H. J. *Polymer Bulletin.* **1990,** 24, 325-332.

63. Shimano, J. Y.; MacDiarmid, A. G. *Synthetic Metals.* **2001,** 123(2), 251-262.

64. Carone, E.; D'llario, L.; Martinelli, A. *Journal of Applied Polymer Science*, **2002,** 83, 857-867.

65. Yang, Z.; Karasz, F. E.; Geise, H. J. *Macromolecules.* **1993,** 26(24), 6570-6575.

66. Biran, C.; Toppare, L.; Tincer, T.; Yagci, Y.; Harabagui, V. *Journal of Applied Polymer Science* **2002,** 86(7), 1663-1666.

67. Bozkurt, A.; Parlak, M.; Ercelebi, C.; Toppare, L. *Journal of Applied Polymer Science.* **2002,** 85(1), 52-56.

68. McCullough, L. A.; Dufour, B.; Rang, C.; Zhang, R.; Kowalewski, T.; Matyjhaszewski, K. *Macrmolecules.* **2007,** 40(22), 7745-7747.

69. Kinlen, P. J.; Frushour, B. G.; Ding, Y.; Menon, V. *Synthetic Metals.* **1999,** 101(1-3), 758-761.

70. van Hutten, P.F.; Gill, R. E.; Herrema, J. K.; Hadziioannou, G. *Journal of Physical Chemistry.* **1995,** 99(10), 3218-3224.

71. Francois, B.; idawski, G.; Rawiso, M.; Cesar, B. *Synthetic Metals.* **1995,** 69(1-3), 463-466.

72. van der Veen, M.; de Boer, B.; talmach, w.; van der Wetering, K.; Hadziioannou, G. *Macromolecules.* **2004,** 37, 3673-3684.

73. McCullough, R.; Williams, S. P. *Journal of Organic Chemistry.* **1993,** 58, 904-912.

74. Iovu, M.; Jeffries-El, M.; Sheina, E.; Cooper, J.; McCullough, R. D. *Polymer.* **2005,** 46, 8582-8586.

CHAPTER II

MATERIALS, EXPERIMENTAL, CHARACTERIZATION TECHNIQUES AND PROCEDURES

Materials

All materials were procured from Aldrich Chemical Company and used as received unless otherwise noted. 2,5-Dibromo-3-hexylthiophene (99%) was purchased from Waterstone Technologies, and *tert*-butylmagnesium chloride (1.7M in THF) was purchased from Acros Chemical Company. Buckminster Fullerene (C_{60}) was ordered from American Dye Source.

Monomer/Macroinitiator Precursors and Grignard Reagents

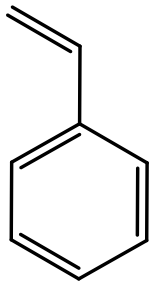

Figure 13. Styrene.

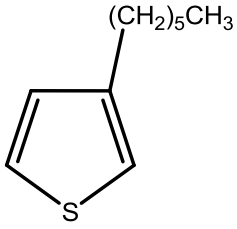

*Figure 14***.** Hexylthiophene.

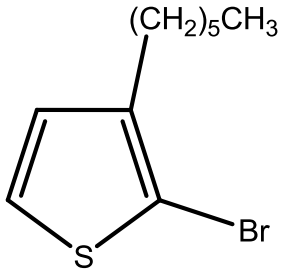

*Figure 15***.** 2-Bromo-3-hexylthiophene.

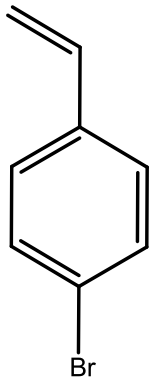

*Figure 16***.** 4-Bromostyrene.

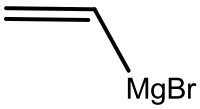

Figure 17. Vinyl magnesium bromide.

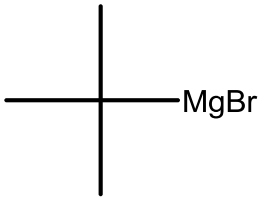

Figure 18. t-Butyl magnesium bromide.

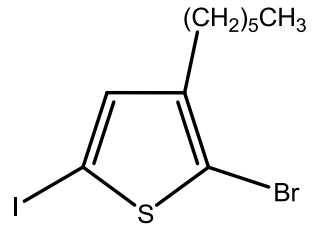

Figure 19. 2-Bromo-3-hexyl-5-iodothiophene.

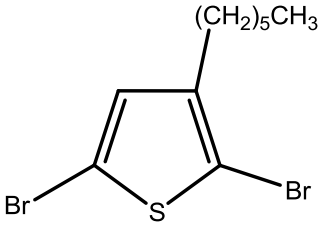

Figure 20. 2,5-Dibromo-3-hexylthiophene.

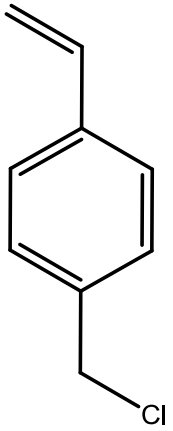

Figure 21. 1-(Chloromethyl)-4-vinylbenzene.

Initiators, Catalyst, Ligands and Mediating Groups

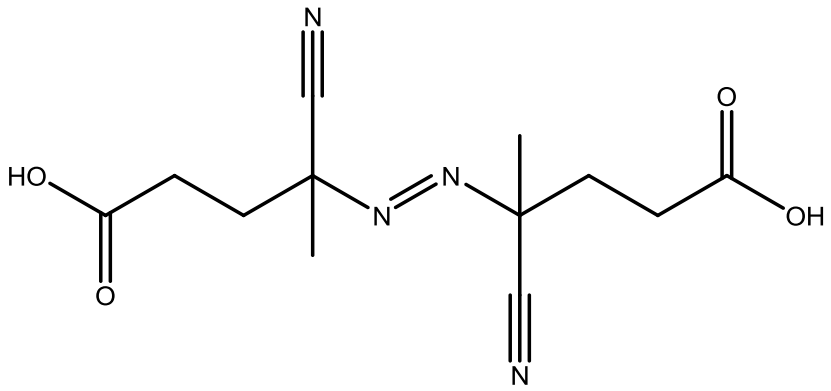

Figure 22. 4,4'-Azobis(4-cyanovaleric acid).

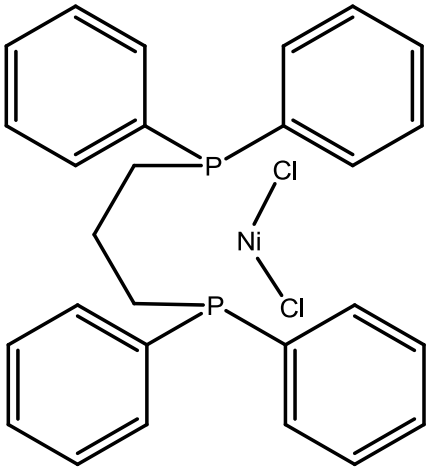

Figure 23. 1,3-Bis(diphenylphosphino)propane dichloronickel ($Ni(dppp)Cl_2$).

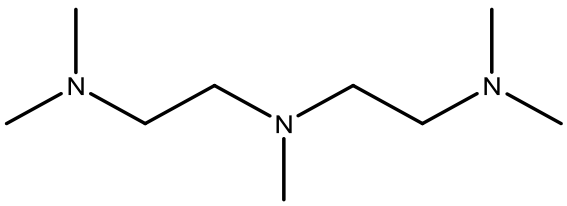

Figure 24. N,*N*,*N*',*N*',*N*",*N*"-Pentamethyldiethylenetriamine (PMDETA).

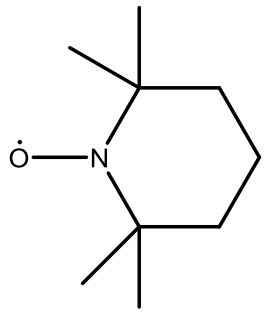

Figure 25. 2,2,6,6-Tetramethyl-1-piperidine-1-oxyl (TEMPO).

Linker Molecules and Macroinitiators

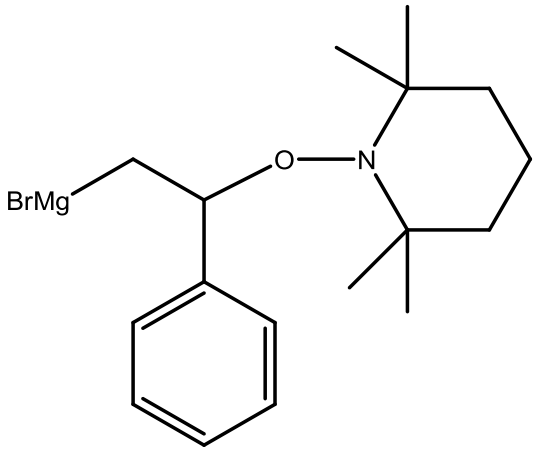

Figure 26. (2-Phenyl-2-(2,2,6,6-tetramethylpiperidin-1-yloxy)ethyl)magnesium bromide.

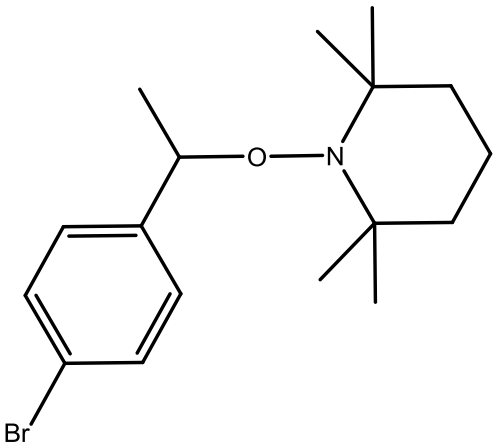

Figure 27. 1-(1-(4-Bromophenyl)ethoxy)-2,2,6,6-tetramethylpiperidine.

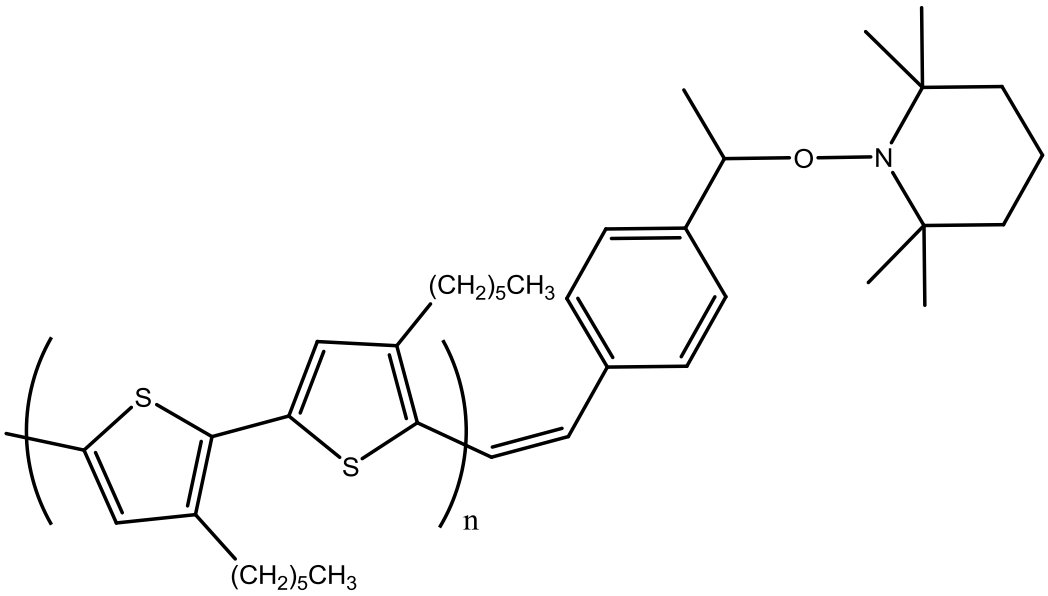

Figure 28. P3HT-TEMPO (Macroinitiator 1).

Block Copolymer and Segments

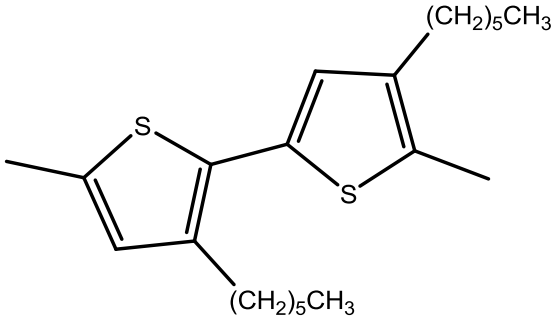

Figure 29. Regioregular Poly(3-hexylthiophene) (rrP3HT).

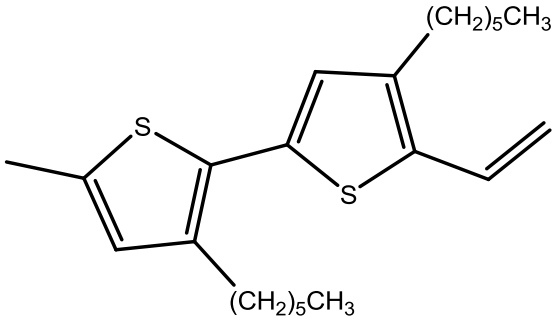

Figure 30. Vinyl P3HT (vP3HT).

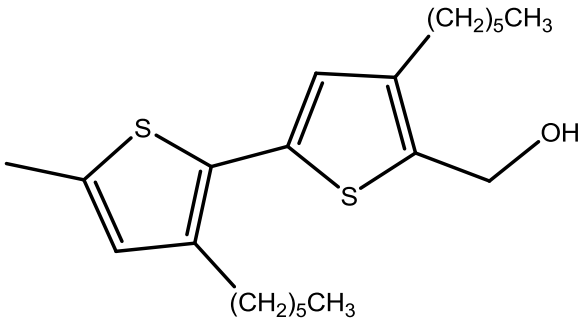

Figure 31. Hydroxy-P3HT (hP3HT).

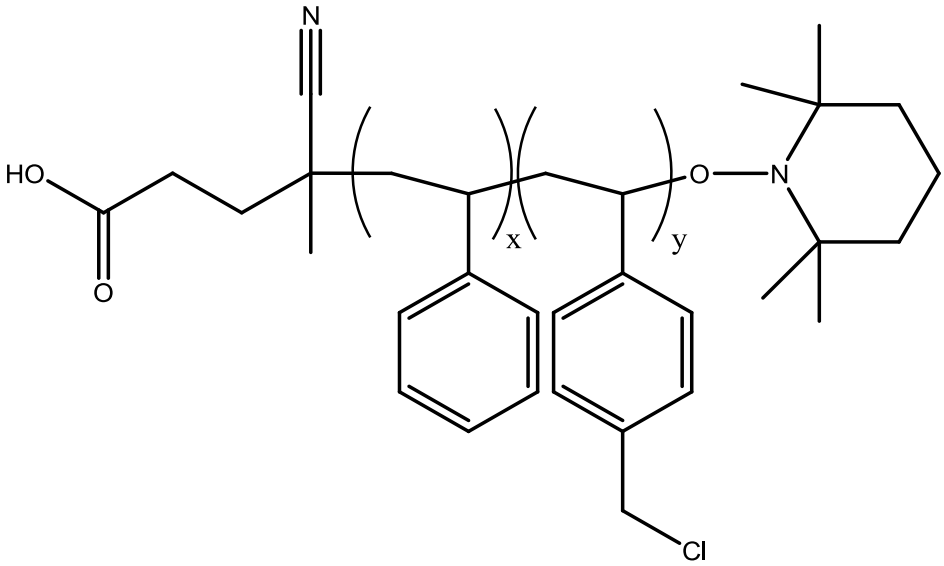

Figure 32. Acid functional polystyrene:chloromethylstyrene (PS:CMS).

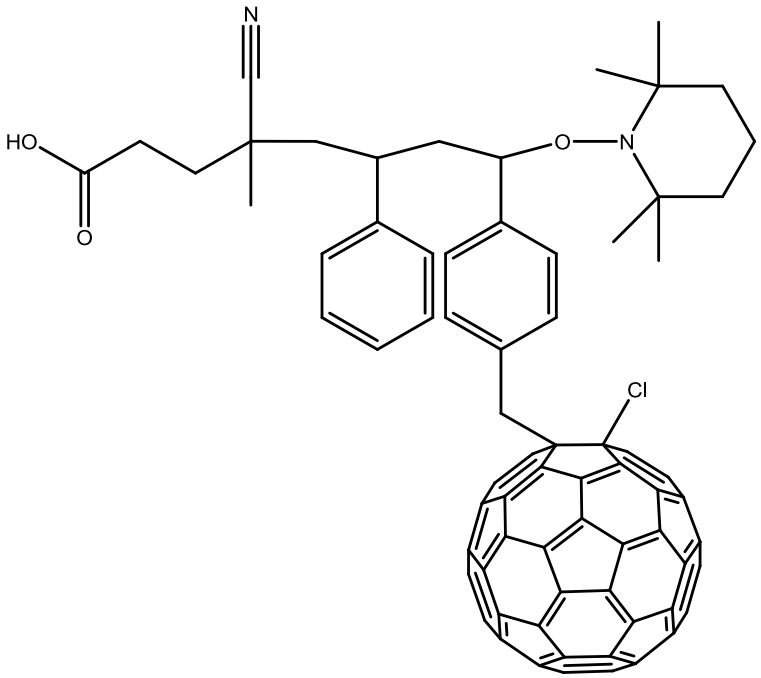

Figure 33. Acid functional polystyrene:chloromethylstyrene:fullerene (PS:CMS:Fu).

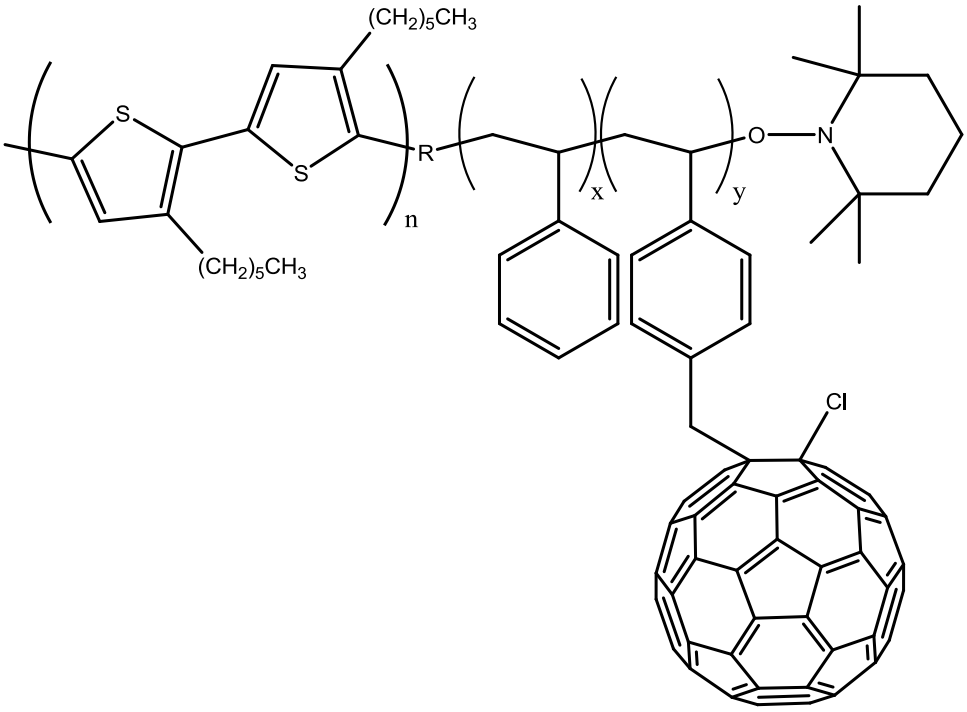

Figure 34. Idealized Goal macromolecule - Block-poly-3-hexylthiopehene-block-polystyrene:chloromethylstyrene:fullerene (b-P3HT-b-PS:CMS:Fu).

Experimental Procedures

Bromination/Iodination of 3-Hexylthiophene

For the selective bromination of 3-hexylthiophene in the 2 position, 3-hexylthiophene ($5.5x10^{-3}$ mole) was weighed into a small Erlenmeyer flask equipped with a magnetic stir bar. Glacial acetic acid (3mL) was then added to the flask. *N*-bromosuccinimide ($5.5x10^{-3}$ mole) was weighed and added through drop-wise addition, at a moderate pace (1 drop every 2-3 seconds) to maintain a slight amount of precipitate in the mixture. The reaction mixture was stirred until all the *N*-bromosuccinimide was solubilized. After stirring for an additional 10 minutes, the reaction was quenched with water, extracted with diethyl ether and washed twice with 1N NaOH and once with water. The extract was dried over magnesium sulfate, filtered, and condensed via rotary evaporation. Product confirmation and purity was determined via GC-MS and ^{1}H NMR. Iodination of the 5 position was performed following the same technique using *N*-iodosuccinimide in place of *N*-bromosuccinimide.

Synthesis of (2-phenyl-2-(2,2,6,6-tetramethylpiperidin-1-yloxy)ethyl)Magnesium Bromide

In dry box conditions, TEMPO ($1.0x10^{-2}$ mole) was weighed into a 25 mL round bottom flask, followed by 5 mL carbon tetrachloride. Upon dissolution of TEMPO, bromine ($5.8x10^{-3}$ mole) was added to the flask. A brown insoluble precipitate was formed and dissolved slowly upon injection of styrene ($9.0x10^{-2}$ mole). After the styrene adduct formed, the CCl_4 and excess styrene were removed via rotary evaporation. The product was washed with water, dissolved

in hexane, dried over magnesium sulfate, filtered and the hexane removed by rotary evaporation. The product was finally recrystallized from methanol. The Grignardized final product was synthesized by adding mechanically activated magnesium powder, generated from mechanical stirring of magnesium turnings, to a mixture of the styrene adduct and diethyl ether. The mixture was refluxed at a temperature of 35°C for 3 hours, and the product was directly injected into P3HT synthesis to end-cap the reaction.

Synthesis of 1-(1-(4-bromophenyl)ethoxy)-2,2,6,6-tetramethylpiperidine

For hydrobromination, a mixture of HBr (48%) and 4-bromostyrene (3:1 molar ratio) was charged into a round bottom flask and stirred overnight in an oil bath at a temperature of 60°C. The mixture was then poured into 200 mL of water and the organic layer was isolated. The aqueous layer was extracted twice with 50 mL diethyl ether. The organic layers were combined and dried over anhydrous $MgSO_4$. The solvent was removed via rotary evaporation and the product was purified by vacuum distillation. The product, 1-bromoethyl-*p*-bromobenzene, was analyzed by ^1H NMR to confirm hydrobromination.

TEMPO, 1-bromoethyl-*p*-bromobenzene, copper bromide and toluene were weighed into a Schlenk vessel and the reaction vessel was sealed. The vessel was subject to three consecutive freeze-pump-thaw cycles to remove any dissolved gases. Simultaneously, PMDETA was sparged with nitrogen and then injected through a purged needle. The mixture was then stirred in an oil bath at 60°C for three hours. The reaction was then cooled and washed with 5N HCl and water to remove excess TEMPO. The product was dried over magnesium

sulfate, filtered through basic alumina, and the excess solvent was removed via rotary evaporation. If necessary, column chromatography or preparative TLC was used to purify the product. The product structure and yield was determined via NMR.

Poly(3-hexylthiophene) Synthesis

The synthesis procedure is exemplified for polymerization at 0.25 M monomer concentration. Each reaction was performed in a nitrogen atmosphere. A dry 100 mL round bottom flask was charged with 5 g of 2,5-dibromo-3-hexylthiophene (0.015 mole) and anhydrous THF (62 mL). Next, 9 mL of the 1.7 M *tert*-butyl magnesium chloride in THF (0.015 mole) was added to the flask and the system was allowed to react for two hours at ambient. Two volumetrically controlled aliquots were removed for gel permeation chromatography (GPC) and gas chromatography – mass spectrometry (GC-MS) analysis, quenched via methanol and acetone, respectively, and considered as time t = 0 for the reaction. At this point, 0.1385 g of Ni(dppp)Cl_2 (2.5×10^{-4} mole) was added to the reaction mixture at a ratio of $[M]_0/[Ni(0)]_0$ of 60:1. Aliquots were taken periodically to quantify monomer conversion via GC-MS and molecular weight via GPC. After polymerization was complete, the mixture was quenched by precipitating the resulting polymer into methanol and filtered. Consecutive Soxhlet extractions were performed with methanol and hexane to remove residual monomer/salts and oligomeric chains, respectively. A final Soxhlet extraction with chloroform isolated the pure polymer product from the nickel species.

End-capping of P3HT

After P3HT synthesis, vinyl magnesium bromide or (2-phenyl-2-(2,2,6,6-tetramethylpiperidin-1-yloxy)ethyl)magnesium bromide were added at either a 1:1 or 5:1 molar ratio to Ni(dppp)Cl_2. To ensure complete reaction, the contents were stirred for an additional two hours before quenching and precipitation in methanol. After Soxhlet extraction, the product was analyzed via ^{1}H NMR to confirm end-capping. Characteristic peaks for vinyl end-groups occurred at 5.11 and 5.49 ppm respectively. [1] GPC results were coupled with comparative NMR integrations to confirm the extent of end-capping.

Hydroboration Oxidation of Vinyl P3HT

The vinyl groups of vinyl terminated P3HT was converted to terminal alcohols through anti-Markovnikov addition using hydroboration oxidation reaction. In this reaction, 9-boro-bicylononane (2 molar equivalents) was added to a nitrogen purged reaction vessel equipped with a mechanical stirrer and external ice bath. Vinyl terminated P3HT (1 molar equivalent based on vinyl) dissolved in anhydrous THF was added drop-wise over 30 minutes. After a five-hour reaction period, aqueous sodium hydroxide (3 molar concentration at 2 Molar equivalents) was added to the vessel at a rate slow enough to maintain the temperature below a temperature of 30°C. 30% hydrogen peroxide (2 molar equivalents) was then quickly added to the reaction mixture. After a 90-minute reaction time, the aqueous and organic layers were separated and purified. The product was then isolated from the organic phase.

Heck Coupling of p-bromostyrene TEMPO with Vinyl P3HT

In dry box conditions, equimolar proportions of vinyl terminated P3HT and 1-(1-(4-bromophenyl)ethoxy)-2,2,6,6-tetramethylpiperidine were added to a reaction vessel equipped with a magnetic stir bar. A catalyst package [$Pd_2(dba)_3$, tris(*t*-butyl)phosphine and methyldicyclohexylamine] and THF were added to the reaction vessel before it was sealed. The reaction mixture was heated to a temperature of 55°C for 24 hours, cooled and filtered through basic alumina. The final product was precipitated into methanol. The reaction progress was verified via ^{1}H NMR while the extent of coupling was confirmed via GPC.

Nitroxide Mediated Polymerization of Styrene:Chloromethylstyrene Copolymer

To a flame dried 250 mL Schlenck flask equipped with a magnetic stir bar was added THF, TEMPO, 4,4'-azobis(4-cyanovaleric acid) or Macroinitiator 1, styrene and 1-(chloromethyl)-4-vinylbenzene. The reactant ratios were based on the desired molecular weight; i.e., degree of polymerization is equal to the moles of monomer divided by functional moles of initiator. TEMPO was added at a 1.2:1 molar ratio to initiator while 0.2:1 molar ratio to macroinitiator was chosen for increased control. The flask was sealed in a nitrogen environment with a rubber septum and secured with copper wiring. The flask was subjected to a minimum of three consecutive freeze-pump-thaw cycles, additional cycles were utilized if bubble formation continued to be apparent. The vessel was then placed in an oil bath maintained at a temperature of 120°C for six hours. The product was precipitated into methanol, dried and characterized via ^{1}H NMR and GPC.

ATRA of Buckminster Fullerene to Styrene:CMS copolymer

Copper bromide, Buckminster Fullerene and polystyrene:chloromethyl styrene were added at molar ratios of 1:1:1 to a 250 mL Schlenk vessel in dry box conditions (molar fraction of copolymer based on chlorostyrene units). Either toluene or *o*-dichlorobenzene was added as solvent media. The vessel was then sealed, removed from the dry box and subjected to three freeze-pump-thaw cycles. Finally, freshly N_2 sparged PMDETA was injected into the vessel and placed in an oil bath maintained at a temperature of 80°C for six hours. The resulting polymer was filtered through basic alumina and precipitated into methanol. The resulting polymer was purified from excess fullerene through solvent selective washes with THF. The product was analyzed via TGA, GPC and ^{1}H NMR to confirm conversion.

Coupling of Hydroxyl P3HT and Acid Functional PS:CMS:FU

In dry box conditions, equimolar proportions of hydroxyl functional P3HT and acid functional PS:CMS:FU were weighed into a reaction vessel equipped with a mechanical stirrer, reflux condenser and heating mantle. Next, toluene and dibutyltin dilaurate were added. The system was heated to reflux conditions and allowed to react for two hours. The final product was precipitated into methanol, dried and analyzed via GPC for information on coupling efficiency. The final product was studied by various casting techniques and its morphology was examined. The product was used to create working OPV cells to determine the photovoltaic output.

Characterization Techniques

Gel Permeation Chromatography (GPC)

GPC was performed on a Varian PL GPC-50 equipped with dual angle light scattering, differential pressure and refractive index detectors. THF was employed as the eluent at a flow rate of 0.8 mL/min at 40°C and a series of four Polymer Laboratory columns (three Polypore® and one 50Å PLGel® column). Toluene was used as an internal standard. GPC data was collected from polystyrene standards using corrected Mark-Houwink constants from literature, i.e., K and a values of 2.28 and 0.97, respectively. [2] Both 100% mass recovery and known dη/dc values methods were employed for analysis. The use of corrected K and a values compensates for the overestimation of molecular weights due to the higher stiffness factor of conjugated polymers. The results were confirmed via Matrix Assisted Laser Desorption Ionization Time of Flight(MALDI-TOF) spectroscopy.

Gas Chromatography - Mass Spectroscopy (GC-MS)

GC-MS was performed on a Hewlett-Packard Agilent 6890-5972A GC-MS workstation using an Agilent DB-1 high resolution column under the following conditions: carrier gas helium, injector temperature 200°C, initial temperature 50°C (3 minute hold), initial temperature ramp to 150°C (1 minute hold), 10°C/min; final temperature ramp to 250°C (20 minute hold); 10°C/min. Samples for GC-MS analysis were withdrawn as volumetrically controlled aliquots to ensure that molar concentration was maintained/tracked throughout the synthesis and characterization and to ensure that the GC-MS data corresponded

to previous calibration curves. The results facilitated verification of monomer conversion and kinetic analysis throughout the polymerization process for both standard conditions and modified conditions for mechanism confirmation.

Scanning Electron Microscopy (SEM)

SEM was performed on an FEI Quanta 200 with Thermo System 7 Energy Dispersive X-ray (EDX) analyzer utilizing 20.0 kV accelerating voltage. Sample preparation did not require conductive alloy coating. SEM was utilized to analyze each fraction during the Soxhlet purification process to determine the location of nickel complexes, as well as, magnesium by products of the reactions. Fractions included non-purified P3HT samples, methanol, hexanes and chloroform extractions and finally, insoluble fractions remaining in the Soxhlet thimble.

Matrix Assisted Laser Desorption Ionization-Time of Flight (MALDI-ToF)

MALDI-ToF spectra were obtained using a Bruker Daltonics Microflex equipped with a 337 nm N_2 laser in linear mode with a 20 kV acceleration voltage. Dithranol was employed as the matrix and all samples were prepared at 1 mg/mL in anhydrous THF as described by McCullough and coworkers. [3] Polymer samples were mixed with Dithranol matrix solution (0.1M in THF) in a 50/50 ratio by volume and 2 μL of each sample were then spotted onto a stainless steel target. An external protein calibration standard (Bruker, protein standard II) was employed for accurate measurements of polymer molecular weight. On average, over 2,000 laser shots were taken for each sample and peak molecular weight values were determined by Microflex analysis software.

MALDI-TOF results were utilized to confirm molecular weight calculations from GPC, as well as, end group analysis to verify the polymerization mechanism.

ReactIR 45M

ReactIR spectra and analysis were collected using a Mettler Toldedo ReactIR 45M equipped with a fiber optic probe and silicon probe tip. Spectral analysis was performed using ICiR software version 4.2 which allowed for trend analysis as well as temperature monitoring. The ConcIRt feature analyzed each sample for trends and identified products based on user defined barriers for time of analysis and wavelengths. Trends were also created based on peak locations of monomer and precursor specific peaks at 1005 cm^{-1} and 800 cm^{-1}, respectively. The spectral results were used for interpreting kinetic observations and monomer conversions. Coupling this information with GPC results enabled confirmation of previously identified mechanisms.

Nuclear Magnetic Resonance Spectroscopy (NMR)

^{1}H NMR and ^{13}C NMR were performed in *d*-chloroform with a Varian Mercury PLUS 300 MHz spectrometer utilizing delay times of two seconds for polymer samples and five seconds for small molecules. For P3HT samples, the resulting spectra were used to confirm regioregularity via peak integration, as reported by McCullough. End-capped P3HT samples were also analyzed via integration to confirm percent end-capping. Both ^{1}H and ^{13}C NMR spectra were used to verify structures of linker molecules and precursors.

Ultraviolet-Visible Spectroscopy (UV-VIS)

UV-VIS absorption spectra were obtained using a Cary 5 Spectrometer. Absorption characteristics were used to characterize the crystalline structure of P3HT and fullerene incorporation. In addition, the maximum absorption values were used to locate appropriate excitation wavelengths for fluorescence spectroscopy and to calculate optical band gaps.

Fluorescence Spectroscopy

Samples were prepared as either 0.1% solution in chloroform (by weight) or as dry films and analyzed using a TECAN Sapphire I spectrometer. Illumination wavelengths were chosen based on absorption maxima from UV-Vis analysis with a 2.5 nm width excitation using 10 bursts with a 10 μs delay before emission was measured. 32 scans were conducted over a wavelength range of 400 to 850 nm.

Thermogravimetric Analysis (TGA)

Thermogravimetric analyses (TGA) were conducted on a TGA Q5000 from TA Instruments, Inc. The analysis was conducted in dynamic mode over a temperature range of 25°C to 1000°C in a nitrogen environment, with a change at 650°C to an air environment. Samples of ~ 15 mg were evaluated for mass loss and thermal stability. This method also facilitated the quantification of Buckminster Fullerene incorporated into the products.

Differential Scanning Calorimetry (DSC)

DSC characterizations were conducted on a DSC Q2000 (from TA Instruments, Inc.) via a heat/cool/heat temperature profile in a nitrogen

environment. Samples approximately 5 mg in weight were evaluated over a temperature range of 0°C to 250°C with heating and cooling rates of 10°C/min and 5 °C/min, respectively. The multiple scans were evaluated and compared for crystallinity exotherms and variations of T_g from the midpoint.

Wide Angle X-Ray Scattering (WAXS) [4]

The crystalline structure of regioregular P3HT and the amount of crystallinity were determined via wide-angle X-ray diffraction (WAXD) measurements, conducted at ambient with a Rigaku Ultima III X-ray spectrometer operating in reflection mode using nickel filtered CuKα radiation (wavelength 1.542 Å). Powder samples were scanned within scattering angle 2Θ from 5 to 40^o. PeakFit automated nonlinear peak separation and analysis software was employed to deconvolute the crystalline reflections and amorphous halo. The weight fraction of crystallinity, W_c, was determined using Ruland method from the corresponding integrated areas under the crystalline reflections and the amorphous halo. [4]

Photovoltaic Output [5, 6]

Photovoltaic output was measured using an A-Nuetronics Data Acquisition System composed of a Kiethley 2400 Source Meter and Kiethley 2000 Multimeter. The system is fitted with a Sciencetech SS150W Solar simulator and AM0 irradiance filter. Sample areas were 0.45 cm^2 with silver ink employed as contact points. Irradiance meters and reference cells were used to confirm illumination intensity and solar spectrum matching. Results are presented in

current versus voltage curves where the area under the curve relates to the efficiency of the cell.

AFM

Atomic force microscopy imaging and film thickness measurements were made with a Nanoscope IIIa MultiMode AFM (Digital Instruments Inc.). The film morphology of dried assembled multilayers was investigated in tapping-mode operation in air. A DNISP steel cantilever mounted with a diamond tip (Veeco Probes, Santa Barbara, CA) was used for dry imaging and dry film thickness measurements. The AFM was calibrated using a platinum reference grid, and the deflection sensitivity of the DNISP probe was found each time an adjustment was made to the laser. The deflection sensitivity was found from indentation on a sapphire surface at forces used for film thickness measurements. Force curves generated during the indentions were used to find the film thickness. Displacement of the piezoelectric actuator (Δz_p) and tip deflection (Δz_t) are related to the indentation displacement (Δz_i) by Equation 1 below, where Δz_t is multiplied by cos(10°) to account for the angle of the probe relative to the horizontal.[7]

$$\Delta z_i = \Delta z_p - \Delta z_t \cos 10°$$

Equation 1. Relationship of tip deflection to indention displacement.

Initial contact with the surface was determined as the point where the oscillation of the cantilever ceased and tip displacement began to increase with movement of the *z* piezo. Contact with the silicon or mica substrate was determined as the point where Δz_t and Δz_p began to increase at a linear rate,

reflecting the deformation of the substrate. The difference between z_i at initial contact and contact with the substrate was taken as the thickness of the multilayer.

Image processing was performed using Veeco version 5.30R3.Sr^2 software. The image root-mean-square roughness (rms) is calculated as the root-mean-square average of the height deviations taken from the mean data plane. The errors reported for the film thickness are the standard deviations of all of the measurements taken.

REFERENCES

1. Jeffries-El, M.; Sauve, G.; McCullough, R. *Advanced Materials*. **2004,** 16(12), 1017-1019.
2. Holdcraft, S. *Journal of Polymer Science Part B: Polymer Physics.* **1991,** 29(13), 1585-1588.
3. Liu, J.; Loewe, R.; McCullough, R. *Macromolecules.* **1999,** 32, 5777-5785.
4. Chabinyc, M. *Polymer Reviews.* **2008,** 48, 463-492.
5. Green, M. *Physica E.* **2002,** 14, 11-17.
6. *Device performance; Measurements & characterization .* National Center for Photovoltaics, National Renewable Energy Laboratory (NREL). 2006. Brochure.
7. Vanlandingham, M. R.; Mcknight, S. H.; Palmese, F. R.; Elings, J. R.; Juange, X.; Bogetting, T. A.; Eduljee, R. F.; Gillespie, J. W. *Journal of Adhesion.* **1997,** 64(1-4), 31-59.

CHAPTER III

REGIOREGULARITY CONTROL THROUGH MONOMER FUNCTIONALIZATION

Introduction

Described in Chapter 1, poly(3-alkylthiophenes) (P3ATs) are being intensively investigated (Figure 35) as a result of their outstanding characteristics; i.e., electronic and charge transport properties, and reasonable tenability from structure-property relationships. P3ATs depend strongly on regioregularity for maximum conductivity. During the polymerization, regiospecificity has a strong effect over main chain and side chain packing; our improved understanding of and the ability to control the self-organizing properties has improved P3AT properties to their current level.[1, 2, 3] For the reasons described above, the selectivity of Grignard reagents appropriate to a particular monomer has been considered an important aspect of Grignard Metathesis polymerization. This chapter will discuss the synthesis of halide specific thiophenes and their role in regioregularity of the resulting P3AT. Specifically, the results for monomers 2,5-dibromo-3-hexylthiophene and 2-bromo-3-hexyl-5-iodothiophene will be compared as starting monomers in initiation and propagation results with particular attention to regioregularity.

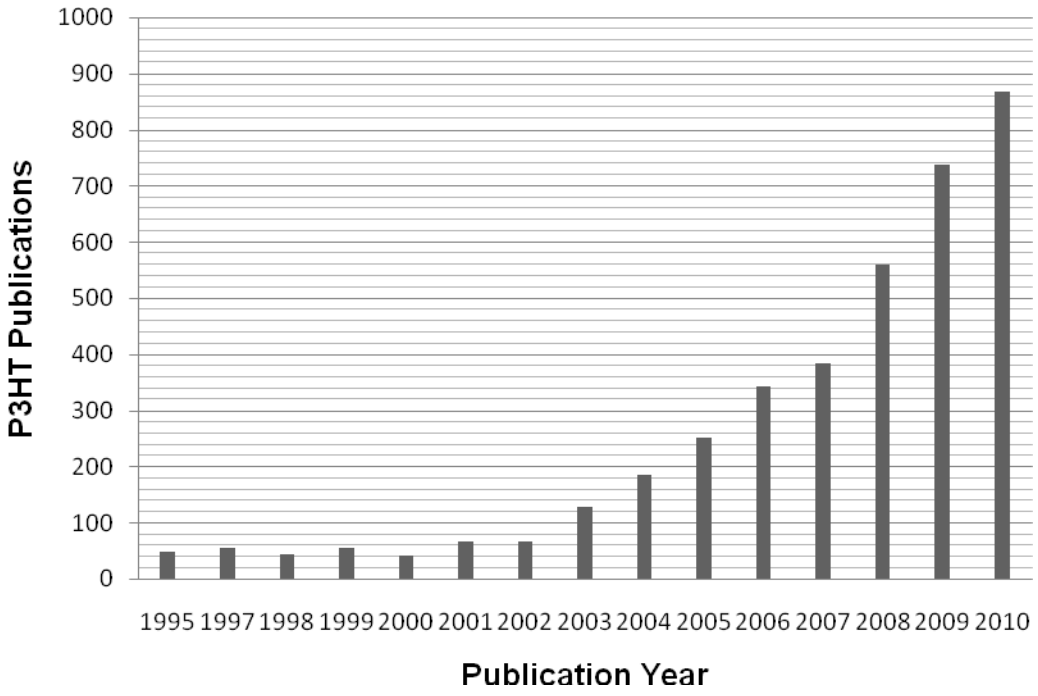

Figure 35. Histogram for publications of P3HT related documents.

Previously, it has been determined that defects through the chain are necessary to contribute to the conductivity of the films formed from P3HT.[(4)] Regioregularity can be a contributing factor to these defects as side chain entanglements, crystalline domain boundaries and chain spacing can all be affected by the frequency of irregular linkages. However, the amount of these defects must be controlled, as too many defects act as charge traps or reduce the ability of charges to hop from chain to chain. With this in mind, regioregularity control becomes a major issue and therefore was the focus of this chapter in terms of the synthesis of monomers that would allow for precise control over regioregularity.

Modification of 3-hexylthiophene

To generative selective reactivity of the Grignardizing agent, *t*-butylmagnesium chloride, 3-hexylthiophene was modified by selective bromination and iodization. The procedure for this reaction is discussed in detail in Chapter II. The first step in the modification process involved selective bromination. The product, 2-bromo-3-hexythiophene, was purified and converted into 2-bromo-3-hexyl-5-iodothiophene following the same procedure as before, however, with the less selective N-iodosuccinimide in place of N-bromosuccinimide. Figure 36 illustrates the ^{13}C NMR spectrum of 3-hexylthiophene, 2-bromo-3-hexylthiophene, and 2-bromo-3-hexyl-5-iodothiophene with the subset showing peak identification, while Figure 37 shows the increase in molecular weight, or increase in retention time, as monitored by GC-MS. It can be seen that the bromination and subsequent iodization cause significant shifts throughout the NMR spectrum, while indicating high to full conversion of the starting materials.

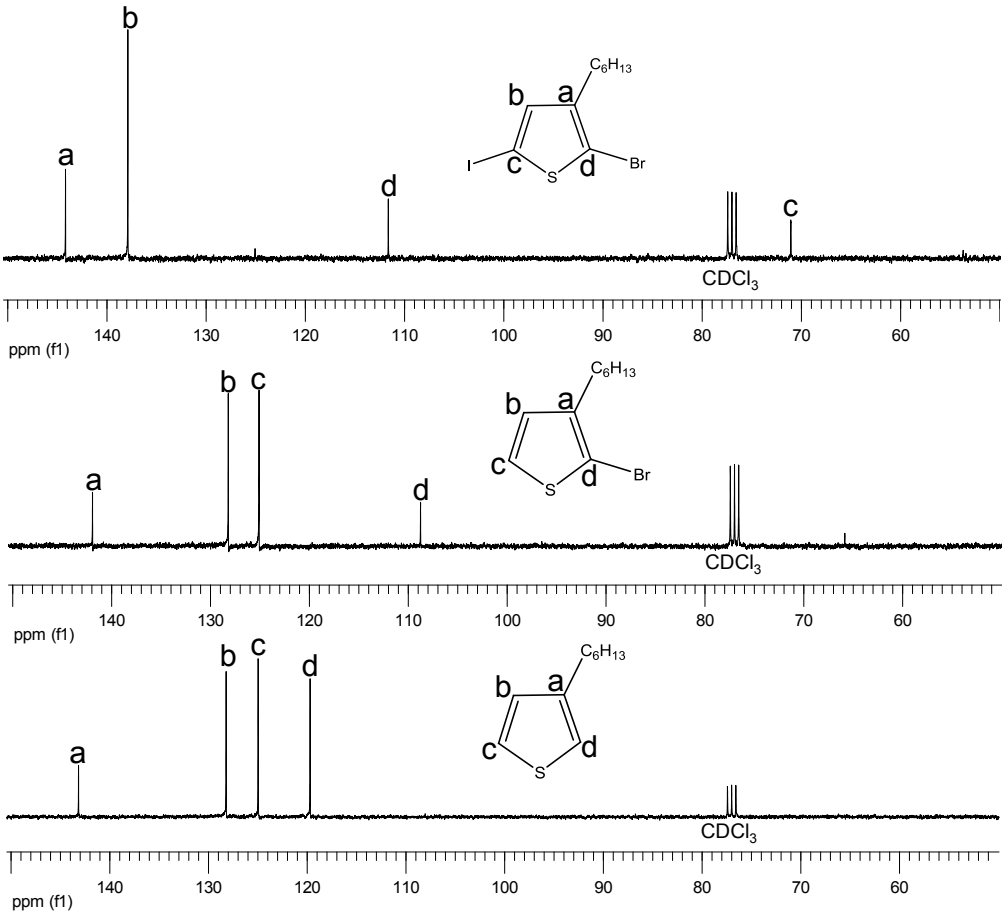

Figure 36. ^{13}C NMR (from top to bottom) of 2-bromo-3-hexyl-5-iodothiophene, 2-bromo-3-hexylthiophene, and, 3-hexylthiophene.

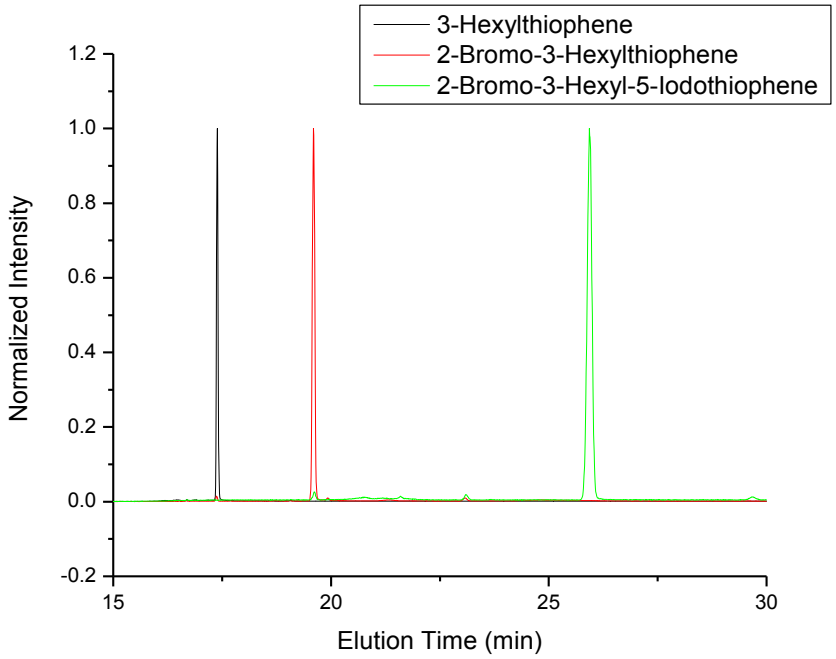

Figure 37. GC-MS of 3-hexylthiophene, 2-bromo-3-hexylthiophene, and 2-bromo-3-hexyl-5-iodothiophene illustrating purity and conversion.

In an examination of Figure 36, significant peak shifts are observed based on the changing electronic environments of each carbon. In the bromination step, two carbons are affected, carbon *a* and *d*. Carbon *a*, which has the hexyl group attached is adjacent to the substituted carbon *d*. The hexyl group acts as an electron withdrawing species making carbon d the most likely place for bromination. Subsequently after addition of bromine, both carbon *a* and *d* see a decrease in electron density, due to the electron withdrawing character of bromine, and therefore a slight shift downfield for *a* and a more substantial shift for carbon *d*. The addition of iodine has a further reaching effect. Iodine is a stronger leaving group and affects multiple peaks, most drastically carbon *c*. The decrease in electron density at carbon *c* resonates through the ring's conjugation

and generates shifts in all the remaining peaks. In the spectrum shown, there is little to no residual peaks remaining, suggesting nearly 100% of the monomer is successfully transformed to 2-bromo-3-hexyl-5-iodothiophene. Finally, any di-iodo or di-bromo species would show an additional peak in the 70 ppm and 110 ppm regions, respectively.

Further examination of Figure 37 confirms the analysis made from the NMR assignments. The lack of multiple peaks within each sample suggests each successive reaction converted nearly 100% of the reactant to the desired products.

Polymerization of 2-bromo-3-hexyl-5-iodothiophene by GRIM

Upon purification, 2-bromo-3-hexyl-5-iodothiophene was polymerized via Grignard metathesis polymerization following the method described in Chapter II (and replacing 2,5-dibromo-3-hexythiophene with 2-bromo-3-hexyl-5-iodothiophene). The resulting polymer was analyzed by GPC and ^{1}H NMR, with ^{1}H NMR providing results on polymer regioregularity. Specifically, peaks located at 2.80 and 2.60 ppm indicate head-to-tail and tail-to-tail couplings, respectively (the peak located at 7.0 ppm is related to the single aromatic proton while all other peaks are related to alkyl chain protons). Integration and comparison of the resulting areas yielded the percentage of regioregular versus non-regioregular linkages. Figure 38 summarizes the results of peak integration for a polymerization that yielded lower regioregularity; this sample was chosen to accentuate the peak differences between head-to-tail and tail-to-tail couplings.

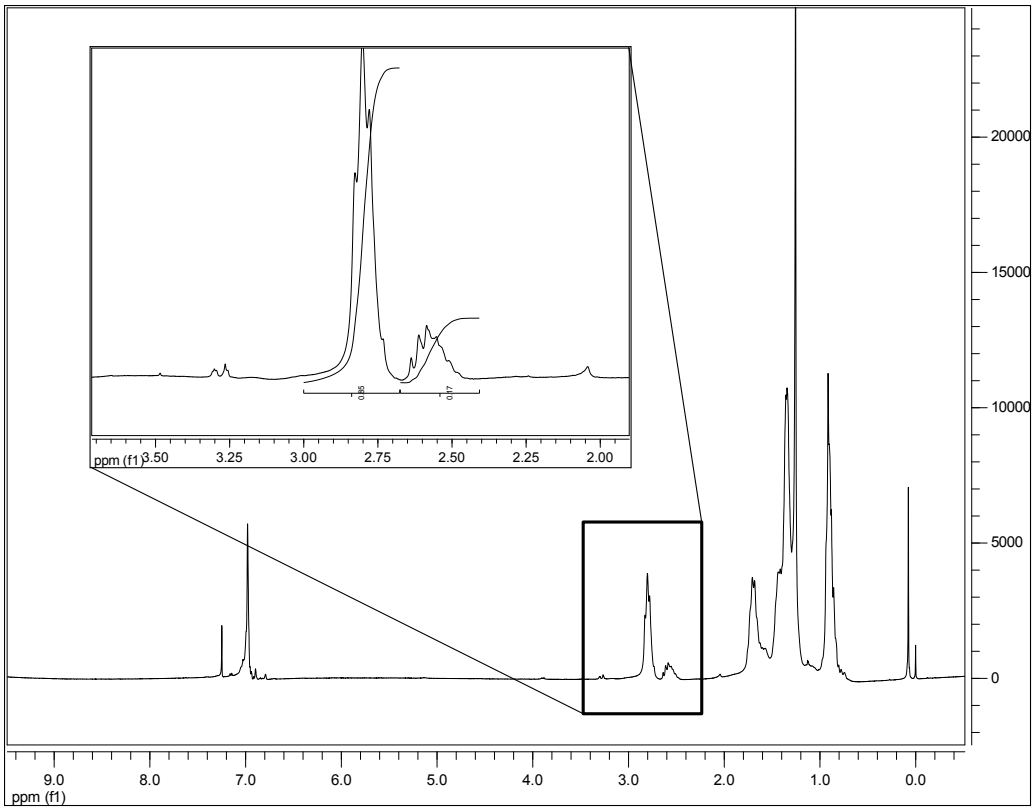

Figure 38. ^{1}H NMR spectrum and integration of regioregular P3HT (rr-P3HT) in polymers of 2-bromo-3-hexyl-5-iodothiophene.

Table 1 summarizes a larger set of regioregularity results from multiple polymerizations with various target molecular weights. Foremost, it is clear that regioregularity was fairly consistent in all polymerizations when the resulting polymers were approximately the same molecular weight, or the same fractions (hexane fraction removed for oligomeric regioregularity). As expected, the lower molecular weight fractions displayed higher PDI values as well as an increase in tail-to-tail couplings. The trend of increasing regioregularity with increasing molecular weight was slightly unexpected and will be discussed in greater detail in the following chapter. 2,5-dibromo-3-hexylthiophene was also polymerized by the same method at similar targets that yielded the same trends and similar results (discussed in greater detail in subsequent chapters).

Table 1

Peak Molecular Weights (from GPC) and Percent Regioregularity of GRIM Polymerizations of 2-Bromo-3-hexyl-5-iodothiophene

Peak Molecular Weight (g/mole)	Polydispersity Index	% Regioregularity
1,150 *	1.79	55.9
2,360 *	1.80	63.3
4,250	1.78	71.7
6,400	1.34	82.4
10,600	1.11	98.7

* Collected from Hexanes Soxhlet Extraction

Table 2 shows the results from select polymerizations of 2-bromo-3-hexyl-5-iodothiophene polymerizations shown in Table 1.

Table 2

Resulting Peak Molecular Weights (from GPC) and Percent Regioregularity of Select GRIM Polymerizations of 2,5-Dibromo-3-hexylthiophene

Peak Molecular Weight (g/mole)	Polydispersity Index	% Regioregularity
1,200 *	1.90	54.0
2,400 *	1.61	65.0
4,400	1.95	75.9
6,100	1.32	91.0
11,000	1.09	98.1

* Collected from Hexanes Soxhlet Extraction

As with the previous polymerization set, regioregularity was significantly different between molecular weight targets. The decrease in PDI values as a function of molecular weight increase is due to the fractionation process, i.e., higher molecular weight fractions are easier to separate from oligomeric species. Compared directly, both 2,5-dibromo-3-hexylthiophene and 2-bromo-3-hexyl-5-iodothiophene yielded polymers within an accepted range of regioregularity,

when the target molecular weight was of significant high values, ~10,000 gm/mole.

Summary

The results from the GRIM polymerizations of two comparable monomers showed minimal differences in regioregularity between each; albeit they were drastically different in terms of directing and leaving group quality. However, 2-bromo-3-hexyl-5-iodothiophene did provide minimal increases in regioregularity versus molecular weight. The added synthesis steps to produce the iodo substituted monomer outweighs the benefits, since 2,5-dibromo-3-hexylthiophene is commercially available. As was previously mentioned, references have shown there is a connection between minimal amounts of regio-irregularity contributing to the increase in conductivity.[5, 4] The combination of these two factors led us to focus our subsequent research on the use of 2,5-dibromo-3-hexylthiophene.

REFERENCES

1. Kim, Y.; Cook, S.; Ruladhar, S.; Choulis, S.; Nelson, J.; Durrant, J.; Bradley, D.; Giles, M.; Mcculloch, I.; Ha, C. S.; Ree, M. *Nature Materials.* **2006,** 5, 197-203.
2. Chuang, S. Y.; Chen, H. L..; Lee, W. H.; Huang, Y. C.; Su, W. F.; Jen, W. M.; Chen, C. W. *Journal of Materials Chemistry.* **2009,** 19, 5554-5560.
3. Kline, J.; McGehee, M.; Kadnikova, E,; Liu, J.; Freche, J.; Toney, M. *Macromolecules.* **2005,** 38, 3312-3319.
4. Feng, D. Q.; Caruso, A. N.; Losovyj, Y. B.; Shulz, D. L.; Dowben, P. A. *Polymer Engineering and Science.* **2007,** 47, 1359-1364.
5. Caruso, A.; Feng, D.; Lozovyj, Y.; schulz, D.; Balaz, S.; Rosa, L.; Sokolov, A.; Doudin, B.; Dowben, P. *Physica Status of Solidi: Part B.* **2006,** 243(6), 1321-1330.

CHAPTER IV

GRIGNARD METAHESIS POLYMERIZATION OF 3-HEXYLTHIOPHENE

Introduction

As mentioned previously in Chapter I, the main mechanism adapted for the polymerization for 3-alkylthiophenes is Grignard Metathesis; however, the precise mechanism of this polymerization process is still being debated. In the generally accepted GRIM mechanism, 2,5-dibromo-3-hexylthiophene is first Grignardized in an 85:15 mixture of the 2 or 5 position (Scheme 1a), where the selectivity of the 5 position is driven by steric hindrance and electronic contribution of the alkyl chain.[1] In the second phase, several authors present the view that the transition metal species [nickel(0)] is associated with a single chain and maintains this association throughout polymerization.[2, 3, 4, 5] For this reason, the transition metal has been attributed to acting as an initiator species rather than a catalyst. The McCullough group suggested that the mechanism proceeds through oxidative addition of monomer followed by reductive elimination to generate a non-diffusive associated pair of a nickel(0) species and bromine terminated polymer chain end (Scheme 1b).[2] However, Yokozawa claims that the mechanism proceeds through intermolecular transfer of the nickel species to the terminal C-Br chain during propagation (Scheme 1c).[3]

Scheme 1. Accepted Mechanisms of Grignard Metathesis Method for the Synthesis of Regioregular Poly(3-hexylthiophene)[2, 3]

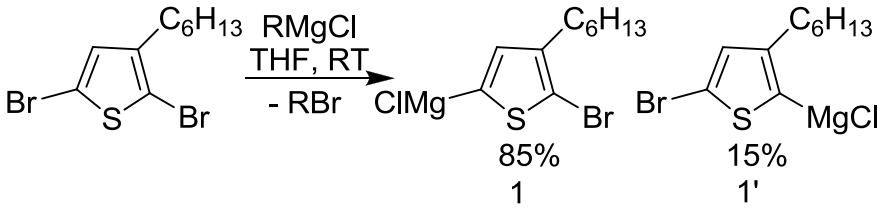

Scheme 1a. Grignardizing 2,5-Dibromo-3-hexylthiophene [2]

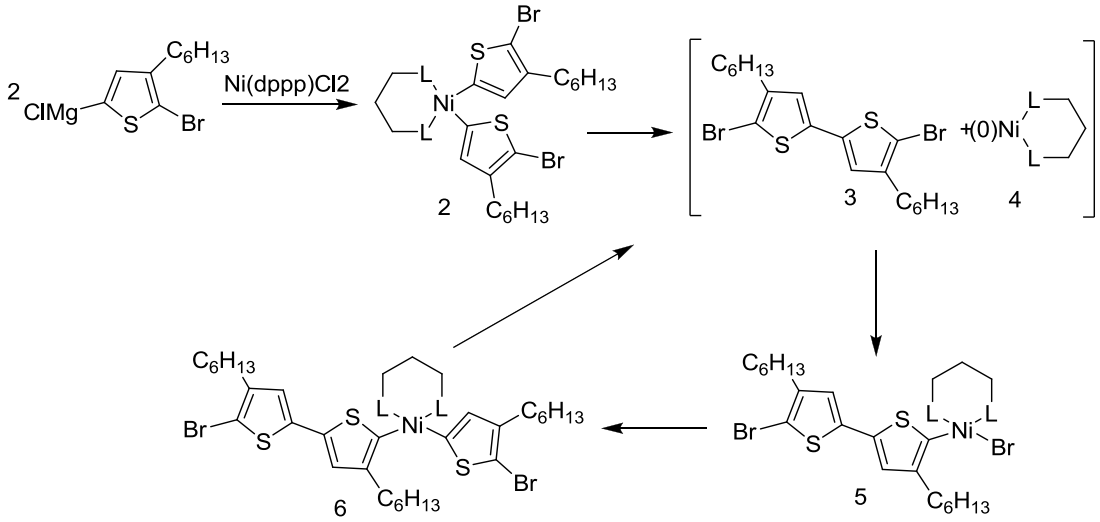

Scheme 1b. GRIM Mechanism by McCullough Group [Ni(0) Species][(2)]

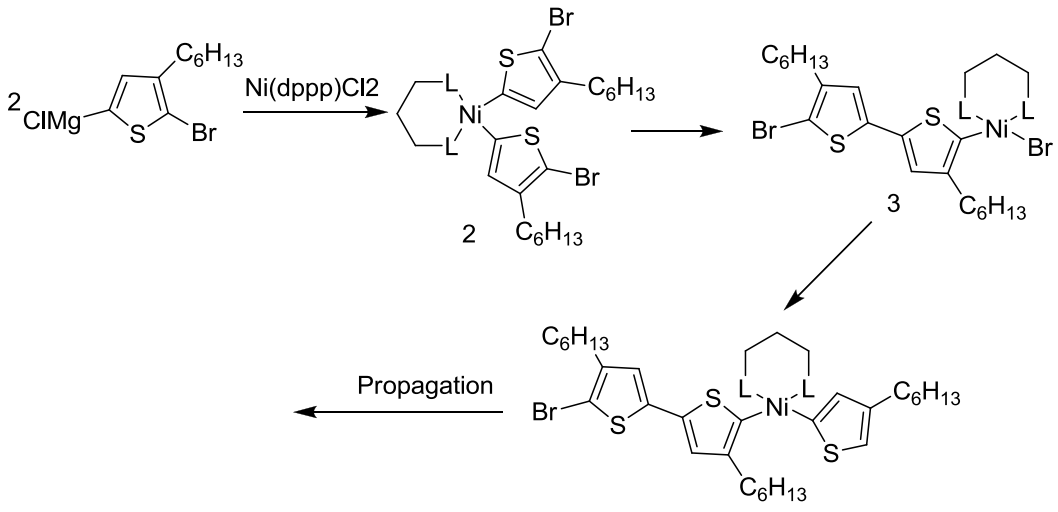

Scheme 1c. GRIM Mechanism by Yokozawa Group (Intermolecular Transfer)[3]

The data from our laboratory presented in this chapter supports another point of view for GRIM polymerization proceeding via nickel(0) diffusion at high rates of re-association. The ability of nickel(0) to re-associate allows for adequate end-capping reactions, while polymer-polymer aggregation and separation rates in solution act as one of the primary molecular weight control mechanism(s). Further, monomer consumption continues throughout polymerization with the formation of new polymer chains after a maximum molecular weight is reached and data consistently supports control via molarity/molar ratios. The data contradicts earlier reports of a direct correlation between $[M]_0/[Ni]_0$ and molecular weight. The MALDI-ToF analysis of non-fractionated samples confirmed nickel(0) species diffusion by end group analysis. The combination of continued conversion after a peak molecular weight is achieved and low polydispersities throughout the reaction further suggest that above a molarity controlled threshold, the nickel(0) species is more likely to associate with oligomeric species than higher molecular weight polymer chain ends. Possibly, the results are affected through the relationship between increasing molecular weight, solubility and functional end group access.

Also, regioregularity has been thought to be controlled by the initial Grignardization of the monomer and selectivity of the nickel association. Regioregularities ranging from 85-97% regioregular linkages are commonly reported.[6, 7, 8] Other controlling variables for these results have been identified as the purity of solvent and reagents as well as atmospheric conditions. Our findings have shown another possibility of a reverse selectivity/reactivity towards

the 15% of monomer Grignardized in the 2 position, or a possibility of unequal Grignardization routes and selectivity of monomer. The Grignardization step is now viewed to be more influential than previously thought, as the rate of polymerization is dictated by the level of Grignardization that has been achieved at the time the nickel species was added. Specifically, early additions resulted in lower molecular weight than was originally targeted, as well as, an extended polymerization time.

Experimental

Polymerization of 2,5-dibromo-3-hexylthiophene

The synthesis procedure for P3HT is described in detail in Chapter II, Poly(3-hexylthiophene) Synthesis and is exemplified for polymerization at 0.25 M monomer concentration. Results below review data collected for polymerization at 0.05, 0.1, 0.25 and 0.5 M and were chosen to augment molarity/solubility effects on polymerization mechanism. Also, to confirm that there was no chain-to-chain coupling during quenching procedure, replica runs were performed with all parameters held constant except that the quenching step was switched from methanol to 5M hydrochloric acid. Some reactions also incorporated secondary monomer additions that extended the polymerization time. Studies monitoring kinetics utilized various times of addition of the nickel species in order to augment the changes seen in the polymerization kinetics as well as in the Grignardization step. The exact reaction conditions will be clearly identified for each of the results shown below.

Results and Discussion

Polymerization Fractions and Components

After filtering the precipitated polymer (see procedure in Chapter II, Poly(3-hexylthiophene) Synthesis) the remaining media was concentrated to separate the resulting salts. The salts and filtered raw polymer were analyzed via SEM-EDX. Figure 39(a) shows the raw polymer before Soxhlet extractions. Figure 39(b) indicates the presence of inorganic magnesium salts as well as unreacted monomer and phosphorus-based ligands retained in the precipitation media. Shown in Figure 39(c), purification of these salts with acetone removed residual monomer and phosphorous based ligands, and validated the choice of acetone as the precipitation media for monomer conversion, as it was assured the monomer would stay soluble in the precipitation media. Continued fractionation by Soxhlet extraction with hexanes isolated pure segments of lower molecular weights, i.e., oligomeric species [Figure 39(d)]. Figure 39(e) pertains to the insoluble fraction remaining in the filter and shows the presence of nickel species. The isolation and fractionation of these species is important for future monomer conversion analysis as well as any post-polymerization reactions. Thus, SEM-EDX analysis confirmed adequacy of the purification procedure and offered complementary information related to monomer conversion analysis.

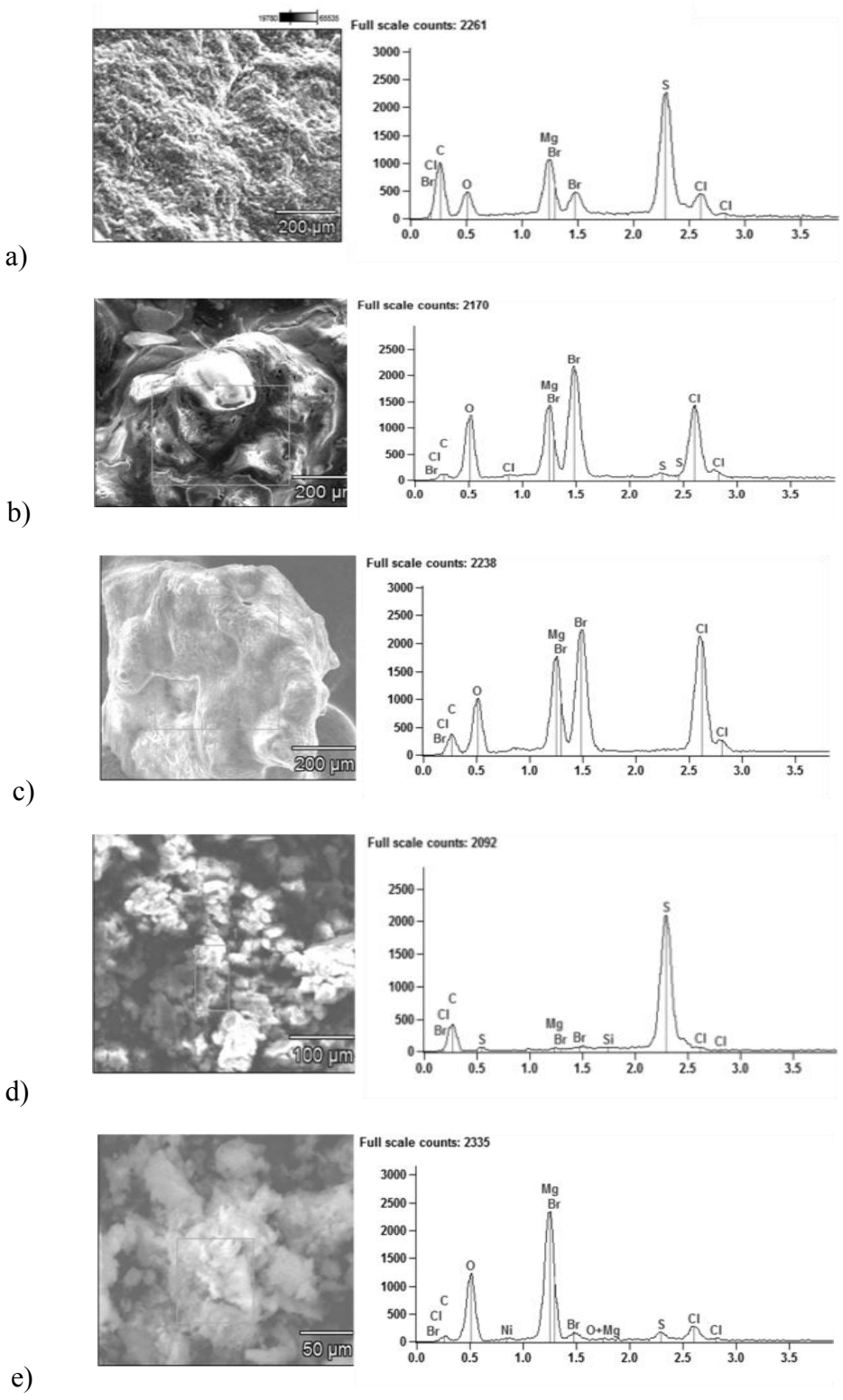

Figure 39. SEM-EDX of a) raw P3HT after precipitation, b) unpurified inorganic salts from precipitation media, c) purified inorganic salts, d) low molecular weight P3HT from hexanes extraction, and e) insoluble fraction remaining in filter.

Polymer Molecular Weight

Molecular weight measurement of poly(3-hexylthiophene) is a key variable in mechanistic considerations. Historically, P3HT molecular weight was determined via GPC analysis based directly on polystyrene standards, MALDI-ToF and NMR. Holdcraft performed ebulliometric studies on poly(3-hexylthiophene) samples and revealed that GPC analysis using polystyrene standards drastically overestimated the molecular weights.[9] Consequently, molecular weight analysis for this study was performed using a corrected calibration curve utilizing the Mark-Houwink values reported in literature, 2.28 and 0.97 for K and a, respectively.[9] Also, MALDI-ToF analysis was used to verify the corrected values. The results of MALDI-ToF and the corrected calibration curve were in close agreement when compared with the traditional universal calibration. Figure 40 below shows GPC molecular weight data versus MALDI-TOF molecular weight data and the deviation from a correlation between the two.[4] Table 3 summarizes the number average molecular weights for two model polymers as non-corrected, corrected, and MALDI-ToF data.

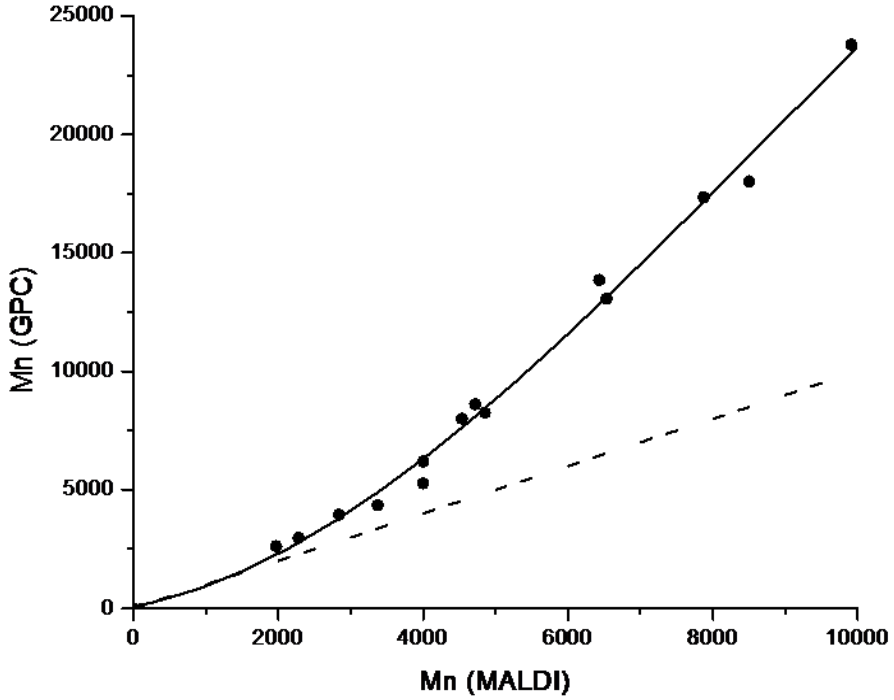

Figure 40. Correlation of molecular weights of poly(3-alkylthiophenes) as calculated by GPC and MALDI-TOF.[4]

Table 3

Number verage Molecular Weight by Comparison of GPC (non-corrected), GPC (corrected) and MALDI-ToF

Polymer	$[M]_0/[Ni(0)]_0$	Molarity (mol/L)	Non-Corrected (g/mol)	Corrected (g/mol)	MALDI-TOF (g/mol)
4K P3HT	60:1	0.1	7,850	4,040	4,110
10K P3HT	60:1	0.5	17,500	7,950	8,720

Influence of Overall Molarity

Molarity effects were studied in experiments conducted at a constant monomer to nickel species ratio of 60:1 and of 100:1. The ratio corresponds to a calculated molecular weight of 9,960 g/mol and 16,600 g/mol at 100% conversion plus the molecular weight of the terminal units (10,041 g/mol and 10,120 g/mol

for mono-brominated and di-brominated, respectively, for the 60:1 ratio). This theoretical maximum molecular weight would present itself if the nickel is associated with only a single chain during polymerization and 100% conversion was reached. However, an increase in the number of actively growing chains should affect a marked decrease in the average molecular weight versus conversion. A decrease in the number of growing chains versus time would be reflected as a trend of increasing molecular weight versus conversion. As the overall system molarity is varied, the number of polymer chains and their molecular weight are expected to remain constant in the absence of factors such as π-π sacking induced aggregation and a correlating loss of solubility.

Figure 41 illustrates the number average molecular weight curves of polymers obtained with 0.1, 0.25, and 0.5 M monomer concentrations at 60:1 monomer to nickel ratio over a two hour reaction period. The results are averages of three polymerizations, with error bars correlating to the standard deviation. The reaction was maintained longer than typically reported in the literature to account for extended monomer conversion in the later stages of the reaction.[2, 3] The data demonstrates that increasing the initial monomer molarity results in higher overall molecular weight with limited effect on polydispersity (Figure 42). After two hours, none of the attempted reagent and catalyst ratios reached the theoretical corrected maximum molecular weight. It is believed that each nickel species association adds a predetermined number of monomer units depending on the instantaneous molar concentration and overall solubility limits before it diffuses either to another chain end or to begin a new chain. In other

words, there is a characteristic association time of the nickel species that will allow a definite number of monomer units, or run number, to add to that chain based on the instantaneous monomer concentration. Polymer and oligomer chain ends would not be exempt from further association; however, increasing molecular weight will reduce the chances of re-association. The ability to re-associate with polymer chain ends offers an explanation for literature reports on end-capping of active polymer chains.[5]

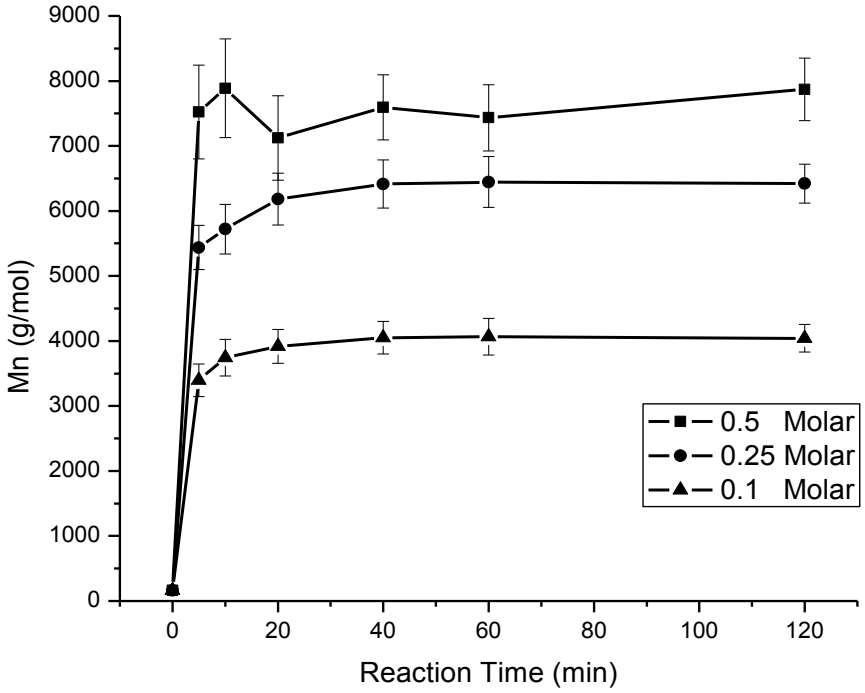

Figure 41. Corrected number average molecular weight via GPC of P3HT as a function of reaction time at various initial molar monomer concentrations and constant 60:1 monomer to nickel ratio.

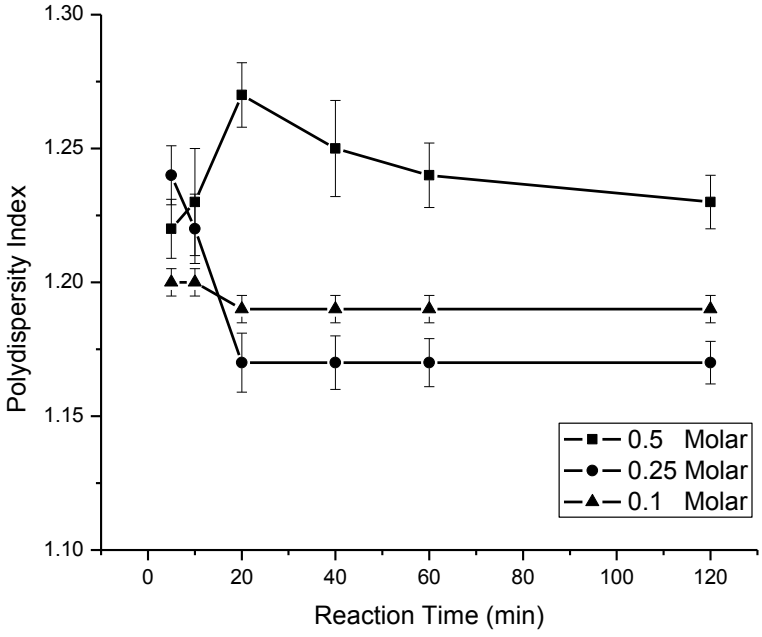

Figure 42. GPC based polydispersity index values for P3HT as a function of reaction time at various initial molar monomer concentrations and a constant 60:1 monomer to nickel ratio.

Table 4 shows consistent trends at both 60:1 and 100:1 monomer to nickel ratios. The change in reaction times before quenching, the lack of variation in molecular weights between the 15 minute species and the two-hour species and residual monomer levels (indirectly monomer conversion) all suggest nickel diffusion through the system. In the absence of nickel diffusion, a constant molecular weight is expected for each monomer to nickel ratio, as well as an increase in molecular weight as the residual monomer becomes lower. The data in Table 4 shows that molecular weight increases and polydispersity decreases with both increasing initial molarity and increasing monomer to nickel ratios. A slightly ambiguous trend involves the residual monomer content as it decreases with increasing molecular weight (increasing monomer to nickel ratios

and increasing initial monomer molarities). However, a consistent exception was observed at 0.1 M concentration.

Table 4

Molecular Weights Based on Varying Nickel to Monomer Ratios and Reaction Time

M_o:Ni	Molarity	Reaction Time	Wt% Residual Monomer	M_p	PDI
60:1	0.05	15 minutes	36.8	2,150	1.61
60:1	0.05	2 hours	15.3	2,270	1.82
60:1	0.10	15 minutes	51.0	6,180	1.25
60:1	0.10	2 hours	8.2	6,340	1.30
60:1	0.25	15 minutes	58.2	7,100	1.17
60:1	0.25	2 hours	32.0	7,470	1.16
100:1	0.05	15 minutes	33.2	4,950	2.08
100:1	0.05	2 hours	28.6	5,350	2.32
100:1	0.10	15 minutes	53.8	8,120	1.85
100:1	0.10	2 hours	11.4	8,450	1.80
100:1	0.25	15 minutes	71.7	10,140	1.63
100:1	0.25	2 hours	62.2	10,500	1.60

When analyzing the trends in the data, molecular weight dependence was noted on both the initial monomer molarity as well as monomer to nickel ratios. An optimum condition can be identified for monomer conversion and PDI. Specifically, higher molecular weight targets and higher initial molarities will result in π-π stacking causing the polymer to fall out of solution. This process has multiple effects on the overall polymerization as the trapped monomer and/or nickel species within the precipitated polymer will limit conversion and result in lower molecular weights. On the other hand, lower molecular weight targets and lower initial monomer concentrations could result in decreased selectivity and reduced regioregularity. This data strengthens our hypothesis and is reflected in

an increase in irregular linkages (as monitored by ^{1}H NMR) on chains that failed to progress to higher molecular weight targets (Figure 43).

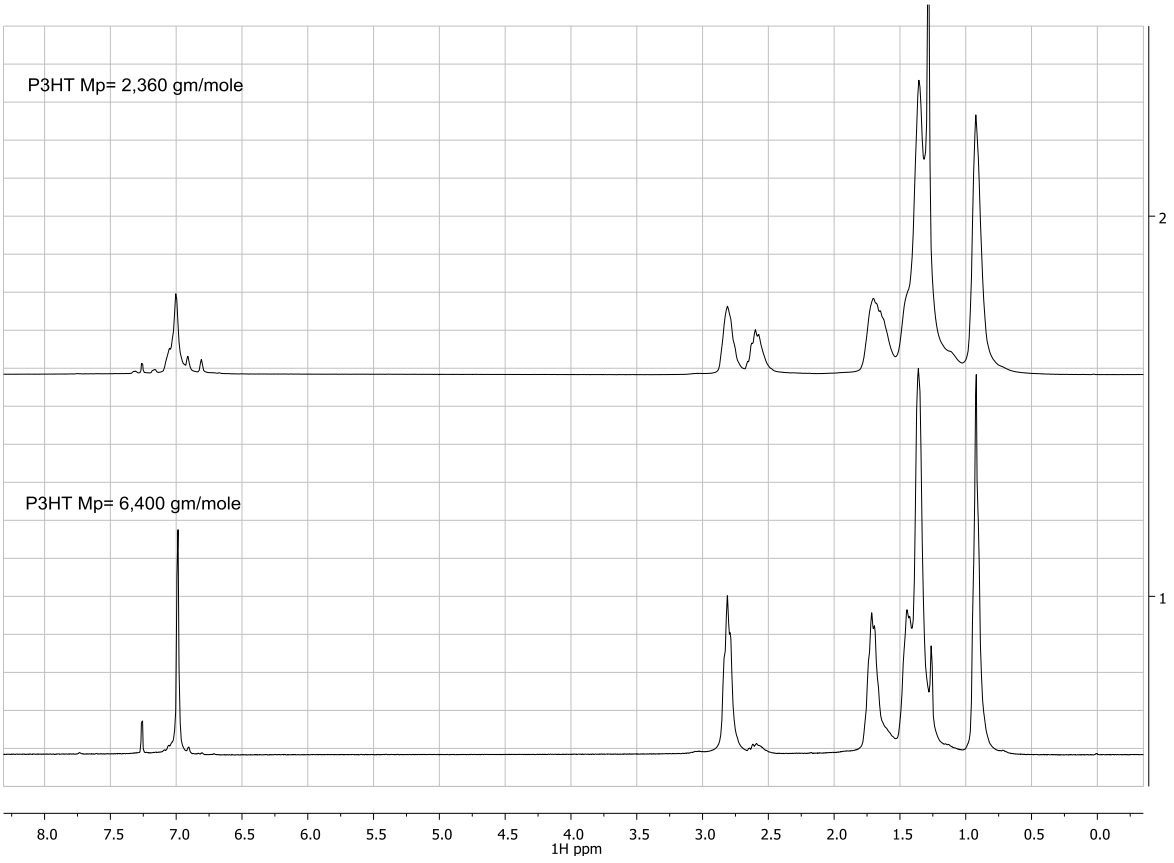

Figure 43. ^{1}H NMR illustrating change in regioregularity between molecular weight fractions. Irregular linkages appear at 2.60 ppm.

Figure 43 highlights the differences between two P3HT samples of varying molecular weight. The peaks of interest occur at 2.6 and 2.8 ppm. Both peaks are related to the protons from the first methylene in the 3 position of the thiophene ring, where the peak 2.8 ppm corresponds to head-to-tail units (Figure 44a) and the peak at 2.6 ppm corresponds to tail–to-tail linkages (Figure 44b). The ability to baseline resolve between these peaks allows for integration and quantification of regioregularity as described in Chapter 3. When comparing the two spectra, it can be clearly seen that the lower molecular weight thiophene

(top) produces a more random polymer. This is a consistent trend over all the polymerizations studied, including systems that were targeted for low molecular weight, or low molecular weight fractions that were fractionated from higher molecular weight samples.

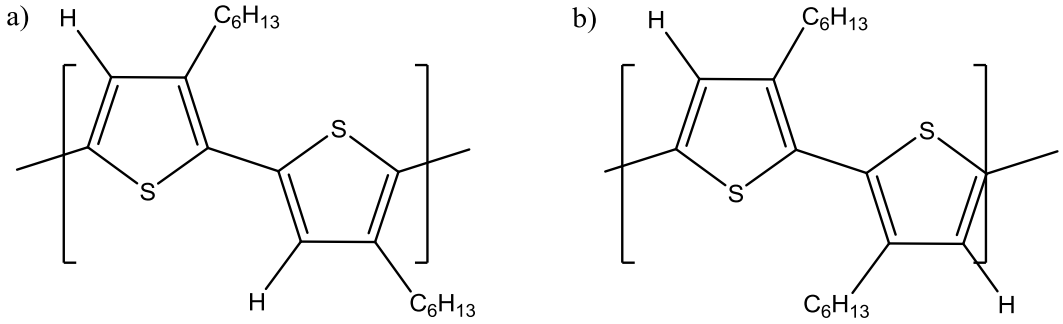

Figure 44. Structures of a) regioregular linkages (head-to-tail) and b) regioirregular linkages (tail-to-tail).

Conversion versus Molecular Weight

When the reactions failed to yield the predicted theoretical molecular weight, the monomer conversion was analyzed via GC-MS. Figures 45 and 46 summarize monomer conversion as a function of time determined over a two hour reaction period for an initial monomer concentration of 0.1 M and a 60:1 monomer to nickel ratio. The polymer molecular weights were confirmed to be constant after twenty minutes, however, the overall refractive index peak intensity continued to increase along with a concurrent decrease in monomer concentration. This is significant due to the nature of aliquot collection; each sample was volumetrically controlled and stirring of the reaction vessel should produce near homogeneous samples. This data confirms the fact that under these conditions, i.e., at a given molarity, any new polymer chains that are formed are limited to the same molecular weight by another controlling factor.

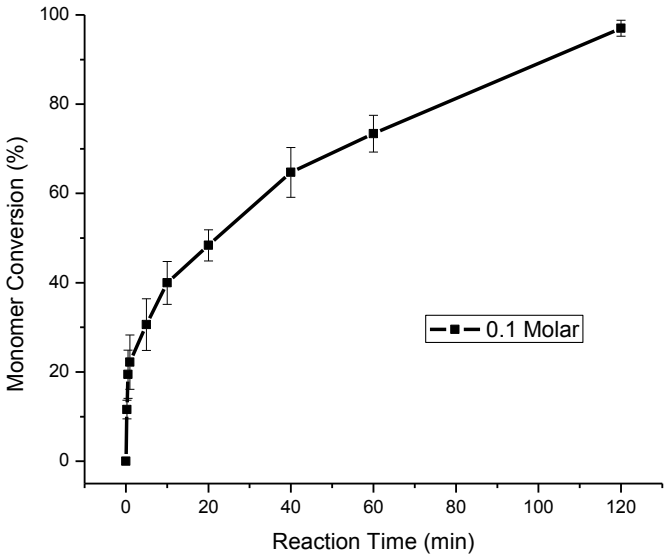

Figure 45. Percent conversion of 0.1M polymerization of 3-hexylthiophene as monitored by GC-MS.

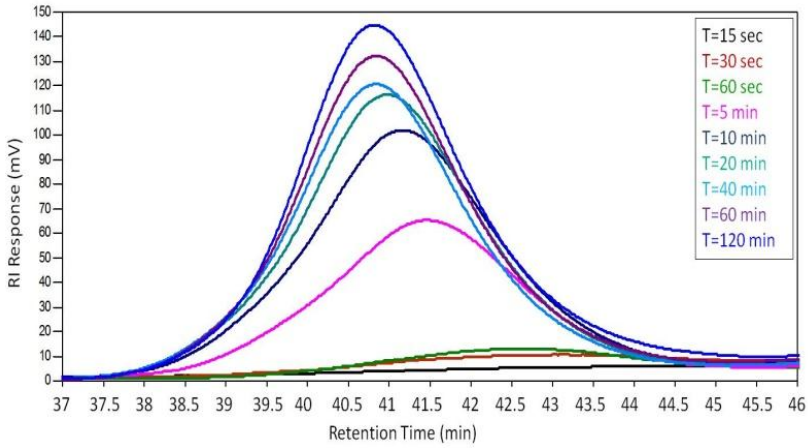

Figure 46. RI trace of 0.1 M polymerization of 3-hexylthiophene showing molecular weight increase and leveling with continual increase of polymer concentration.

Polymer Chain Ends

The discrepancy between molecular weight versus molar ratio of nickel and continued conversion versus time with limited molecular weight were inconsistent with prior literature results and required polymer chain end analysis for further understanding. When the nickel species is associated with a chain

end and the polymerization was quenched by methanol, the end group was converted to terminal hydrogen.[4] The opposite and remaining end-group would be bromine. To confirm whether each nickel(0) species was associated with a single chain during polymerization, MALDI-ToF analysis was performed to search for specific and iterative end group effects on molecular weight. Figures 47 and 48 reveal the MALDI-ToF results for a reaction conducted with the same molecular weights and ratios as employed in Figures 45 and 46. The peaks correspond to either m/z = 166n+1+80 (mono-brominated) or m/z = 166n+80+80 (di-brominated), where 166 is the repeat unit molecular weight, n is the number of repeat units, 1 refers to the terminal hydrogen and 80 is from the terminal bromine group. The reported mechanisms would yield molecular weights that match only the mono-brominated equation, with very low concentration of peaks matching the di-brominated set. The presence of two peak sets at appreciable ratios confirms the absence of nickel on a percentage of chains during quenching. The corresponding molecular weight for a reaction at 97% conversion (Figures 45 and 46) is much lower than the theoretical molecular weight if nickel were to remain associated to a single chain throughout the polymerization. This strongly suggests diffusion of the nickel species from higher molecular weight chains to both oligomeric species and monomer creating additional new chains.

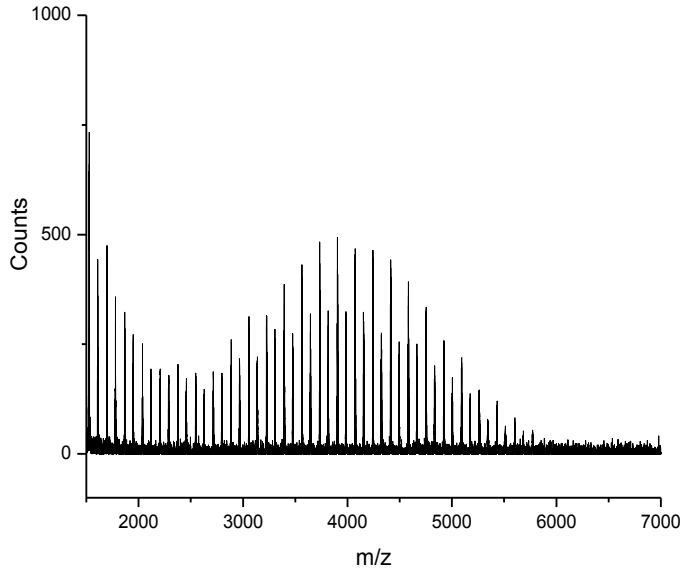

Figure 47. MALDI-TOF results of 0.1 molar polymerization of 3-hexylthiophene quenched with methanol showing both H-Br terminated chains as well as Br-Br terminated chains.

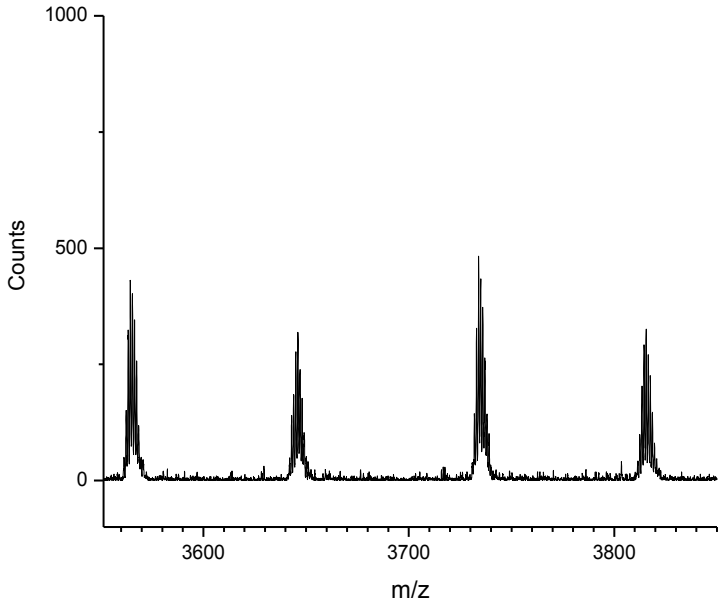

Figure 48. Expanded MALDI-TOF of 0.1 molar polymerization of 3-hexylthiophene quenched with methanol showing both H-Br terminated chains as well as Br-Br terminated chains.

It has been previously reported that quenching growing polymer chains with water causes chains to couple generating di-brominated chains with higher

molecular weight.[10] However, the lack of bimodality, lower than expected molecular weight and low polydispersity in MALDI-ToF analysis suggest that such coupling does not occur. To confirmation that the results were not from coupled chains, several replicate runs were performed where the quenching reagent, methanol, was replaced by 5M hydrochloric acid in order to deter any coupling reactions. The detailed examination of the results (Figure 49) reveals the continued presence of both mono- and di-brominated chain ends, as once again peaks matched both the m/z = 166n+1+80 (mono-brominated) or m/z = 166n+80+80 (di-brominated) equations. Furthermore, the GPC results shown in Figure 46 reiterate the lack of bimodality. Uniform polymers with low polydispersity index (PDI) are observed in spite of a four column series, which would increase separation and exaggerate any bimodal properties.

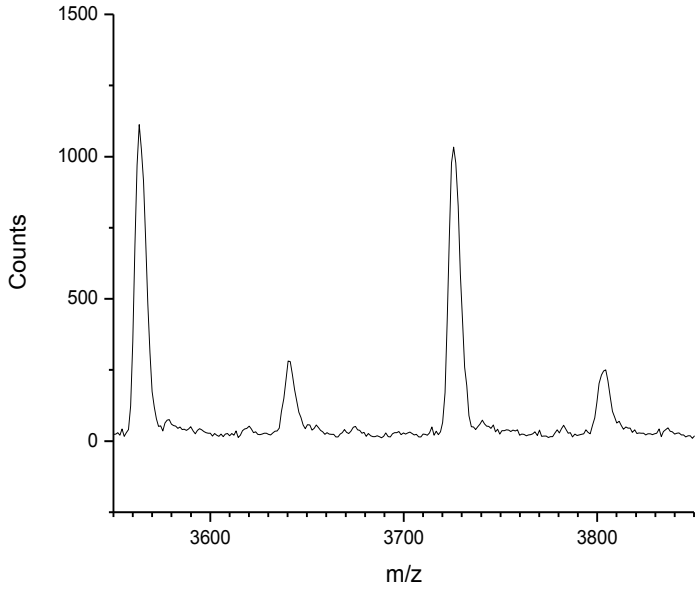

Figure 49. Expanded MALDI-TOF of 0.1 molar polymerization of P3HT quenched with 5M HCl showing both H-Br terminated chains as well as Br-Br terminated chains.

Extended Monomer Reaction for Proof of Continued Monomer Conversion

To further test the Ni diffusion theory, the duration of the monomer addition process was extended. The experimental goal was to distort the polydispersity and molecular weight plateau from the results of a single monomer addition process, and also allow the procedure to mimic a staged block copolymer synthesis while using the same monomer. If the polymerization is based upon a constant nickel association with a single polymer chain, extended monomer addition should increase the bulk molecular weight significantly while maintaining polydispersity. Accordingly, polymerization was initiated at a starting concentration of 0.1 M and allowed to react to 50% conversion, based on previous experimental results. At this point, the polymerization was extended using a secondary batch of monomer formulated to 0.06 M concentration in THF. The corresponding theoretical molecular weight for a single-chain nickel-association was expected to be 17,370 g/mol, a 75% increase. The monomer was fed continuously into the reaction at a feed rate matching the order of magnitude from the experimentally determined instantaneous monomer consumption rate. The same, but secondary addition of monomer (0.012 mole), was fed into the reaction over two hours and the mixture was allowed to react for two hours once addition was completed (total of four-hour reaction time). Aliquots were extracted at predetermined intervals throughout all stages of polymerization. As shown in Figure 50 and Table 5, GPC traces of the resulting polymer confirmed our theory of nickel diffusion and limited return to the original chains based upon a diminished collision frequency at a given molarity. The

reduction in the main peak areas is related to dilution effects from the second monomer addition, which was at a lower concentration than the original monomer batch. The limited peak molecular weight shift, increasing overall PDI, and a small, yet clear shift to higher molecular weight for late adding chains are key points that confirm diffusion. Under these conditions, it is clear that the majority of chains are not old polymer chains that increased in molecular weight but are new chains resulting from nickel diffusion via additional chain initiation and propagation. It should be noted that the molecular weight data was collected on a different GPC instrument with two PL-gel columns in series at a flow rate of 1.0 mL/min, and all other parameters including correction from polystyrene standards followed previous conditions. The conditional changes account for the variance in retention time.

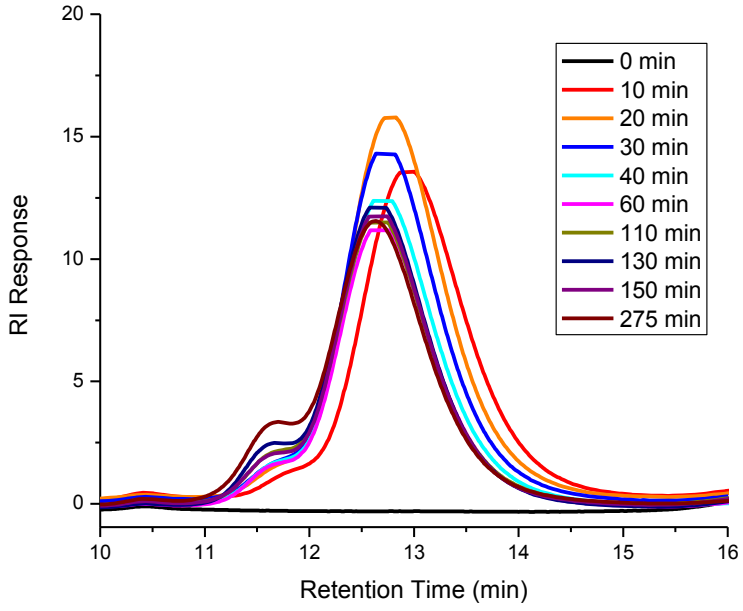

Figure 50. RI traces of 0.1 molar polymerization of P3HT with secondary 0.06 M monomer addition (P3HT).

Table 5

Corrected Number Average Molecular Weight, Polydispersity Indices and % Area of High Molecular Weight Shoulder

Reaction Time (min)	M_n (g/mol)	PDI	% Area Shoulder
10	3440	1.20	4.42
20	4030	1.19	5.72
30	4070	1.15	6.97
40	4100	1.15	7.77
60	4220	1.33	8.26
110	4250	1.35	9.50
130	4420	1.34	10.43
150	4590	1.52	11.51
275	4690	1.60	15.44

In a detailed examination of the GPC traces, the shoulder that is formed is a concern; however, this shoulder is believed to be related to coupling chains in the late stages of polymerization, in other words, the chains with multiple nickel associations in their lifetime. The percentage of the area and the limited effect on the overall calculated molecular weight suggests that this is the case.

Regioregularity Control and Monomer Reactivity/Kinetics

The last step in examination of the polymerization mechanism involved simultaneously monitoring the kinetics of the Grignardization step and polymerization. The observation on how regioregularity is affected by various changes in the polymerization process was also monitored. For kinetic analysis of the Grignardization step a series of reactions were prepared where the formation of the Grignardized monomer (by loss of C-Br bonds) and loss of *t*-butylmagnesium chloride were monitored simultaneously in real time with a ReactIR 45M. The control experimental conditions were the standard formulation

and timing system (2 hours of reaction time before nickel addition). Other systems monitored were a system where the nickel was not added until the mixture reached a complete equilibrium and finally a system where nickel was added directly after the Grignard reagent. Figure 51 shows an example of the real time spectra that are acquired (peaks of interest pointed identified with arrows). The results of these experiments were surprising; the kinetic analysis supported the changing rate of Grignardization correlated with increased rates upon the addition of nickel, the monomer was converted to the reactive Grignard species at varying rates. It is also of note that this Grignardization is much longer than previously thought. These findings, under our conditions, clarify that the Grignardization step quickly becomes the rate limiting reaction. Trends showing the conversion (consumption of t-butylmagnesium chloride) of each of the three systems are summarized in Figure 52. In the three conditionally distinct systems it becomes even more surprising that the overall yields were similar; however, the resulting polymers were decidedly different as shown in Table 6. The data support a hypothesis: forcing the Grignardization step to become the rate limiting step early in the polymerization in turn forces the diffusion characteristics of the nickel to be more clear/evident.

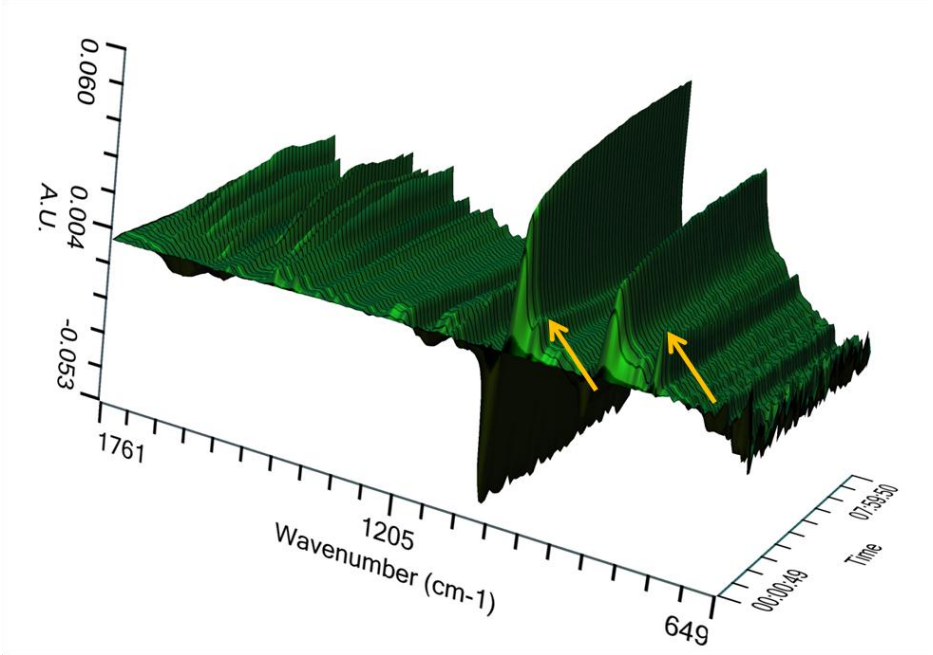

Figure 51. Surface spectra as recorded by ReactIR (arrows indicate peaks of interest).

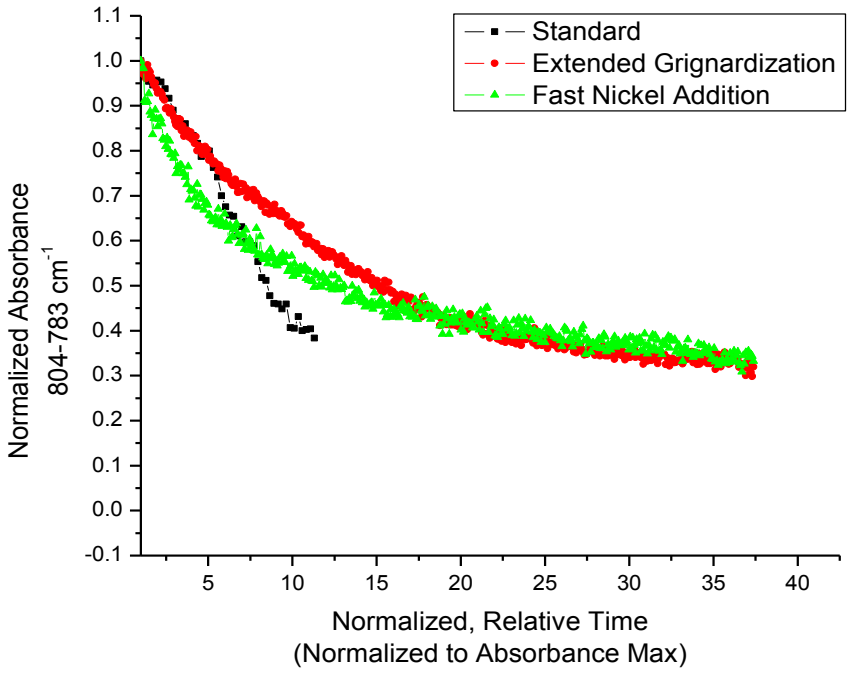

Figure 52. FTIR spectral results showing trends for conversion of *t*-butylmagnesium chloride, 804-783cm^{-1}.

Table 6

Molecular weight and yield data for reactions with varying nickel addition times.

	M_n (g/mole)	M_w (g/mole)	M_p (g/mole)	% Yield
Standard	6,180	8,040	8,260	96.2
Extended Grignardization	8,410	10,460	10,825	97.1
Fast Nickel Addition	2,600	3,405	2,710	95.4

Once the resulting molecular weight data was coupled with kinetic information/results, it appears that by forcing the Grignardization step and early nickel addition the reaction diffusion increased. This can be seen in the "Fast Nickel Addition" experiment where molecular weight is decreased due to the higher dependence on the Grignardization step, which in turn promotes the diffusion of nickel. This also could be expressed in terms of the run number, where run number should decrease as the amount of available Grignardized monomer is decreased for each characteristic association time. The reverse and opposite effect can be seen in the "Extended Grignardization" reaction, where at the time of nickel addition there is an increased instantaneous concentration of Grignardized monomer. It is of note that the rate of consumption of monomer species is faster after nickel addition. This can be explained simply by Le Chatelier's principle; the rapid and nearly immediate consumption of the Grignardized species forces the equilibrium towards product formation, i.e. consumption of *t*-butylmagnesium chloride.

Furthermore, the regioregularity results versus molecular weight were examined. For greater understanding and to probe the specific correlation between the properties additional experimental conditions were used to validate/refute our hypothesis. The lowest molecular weight samples were acquired by separating the oligomeric species with Soxhlet extraction, where the hexanes fractions were the isolated species. The moderate molecular weight species were synthesized by varying both the initial monomer concentration and nickel concentration, yielding various molecular weights. ^{1}H NMR was then used to calculate the percent regioregularity of the samples following the previously mentioned procedure, (Chapter III, Polymerization of 2-bromo-3-hexyl-5-iodothiophene by GRIM). Figure 53 summarizes the ^{1}H NMR spectra for various molecular weights, where the spectra are stacked with the lowest molecular weight species at the bottom. This figure shows a clear correlation between molecular weight and regioregularity; however, Figure 54 provides a more quantitative examination of the polymers and oligomers presented in Figure 53.

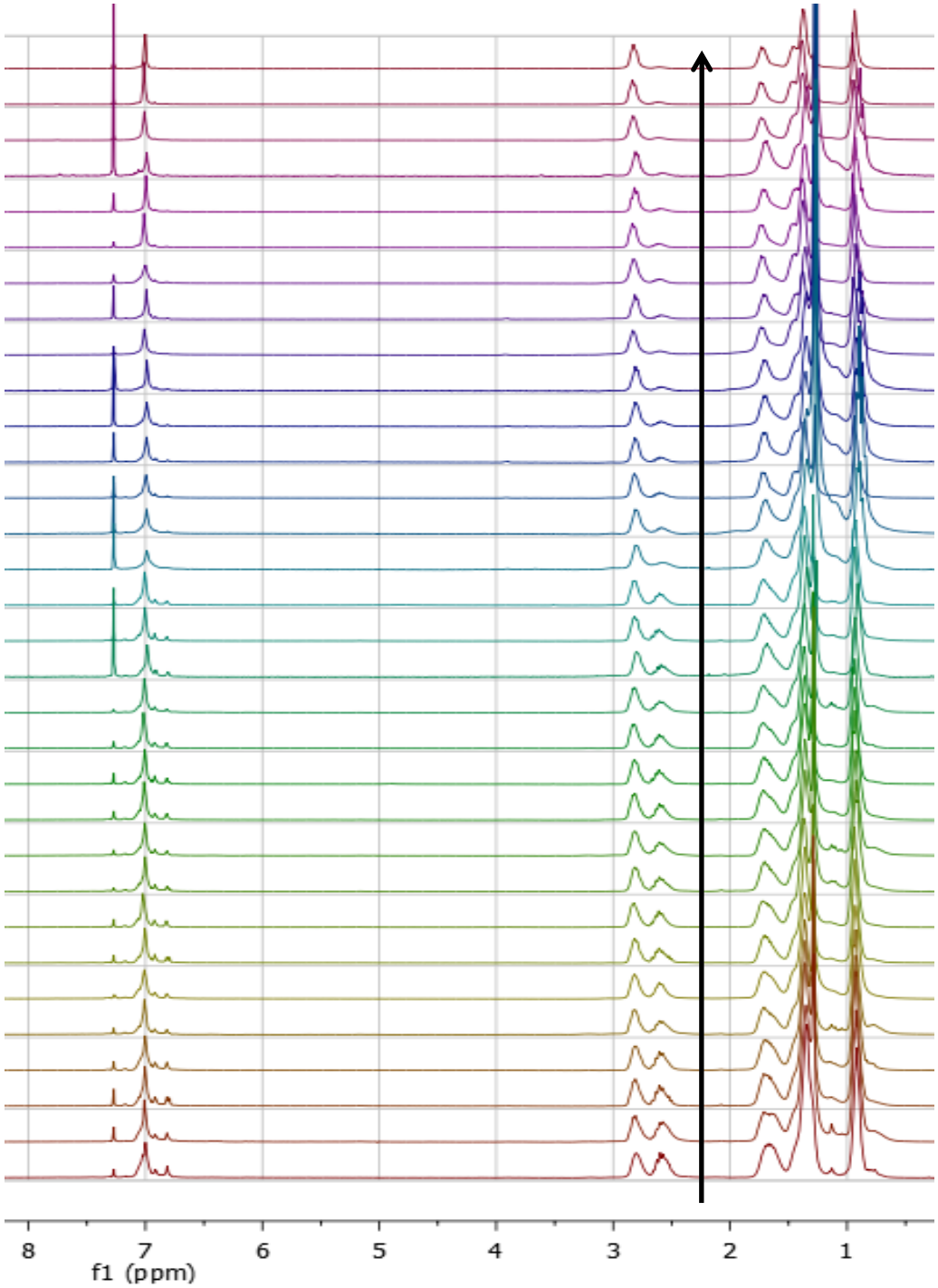

Figure 53. ^{1}H NMR showing regioregularity versus molecular weight: lower molecular weight species are on the bottom.

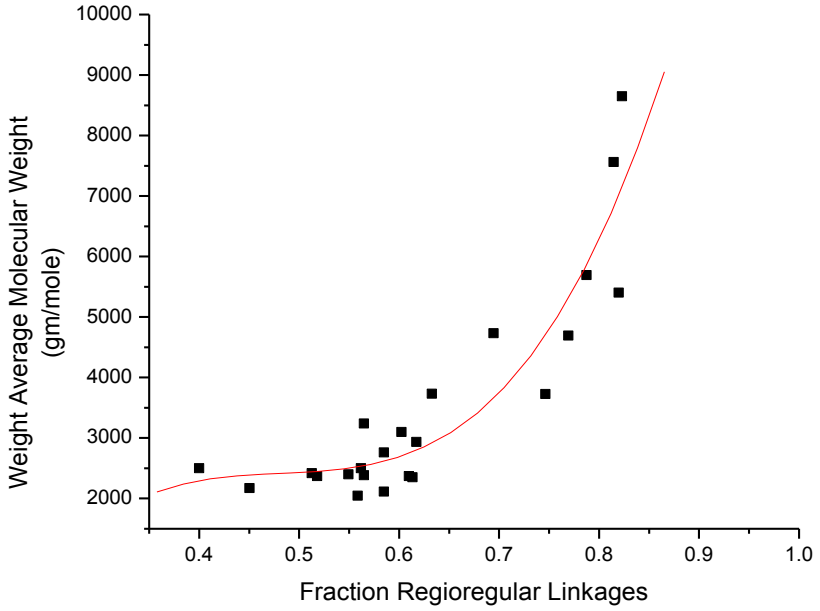

Figure 54. Graph of number average molecular weight versus regioregularity.

It is important to note that the data presented above possess a sharp increase in regioregularity and samples synthesized at higher molecular weight targets produce polymers of similar regioregularity, typically 95% or greater.

Proposed Mechanism

Based upon the data presented in this chapter, the previously discussed polymerization allowed for the determination of a new suggested mechanism. The mechanism shown below in Scheme 2 is similar to that of the McCullough Research Group; however, the main differences are the rate controlling step is actually the creation of the Grignardized monomer and there is a diffusion of the nickel that is capable of either starting new chains or binding with previous polymer chains. If monomer is completely converted to the Grignard species the diffusion is controlled by three characteristic constants, $K_{addition}$, $K_{diffusion}$ and $K_{association}$. $K_{addition}$ is the term that affects the run number, or number of monomer

units added per association of nickel to a chain end before $K_{diffusion}$ causes the nickel to diffuse to either a new chain or a previously initiated chain. The association with a new monomer or a polymer chain is controlled by access to the end group of the polymer chain, thereby forcing molecular weight, solvent concentration, and instantaneous monomer concentration to become increasingly important for regioregularity and the resulting molecular weight.

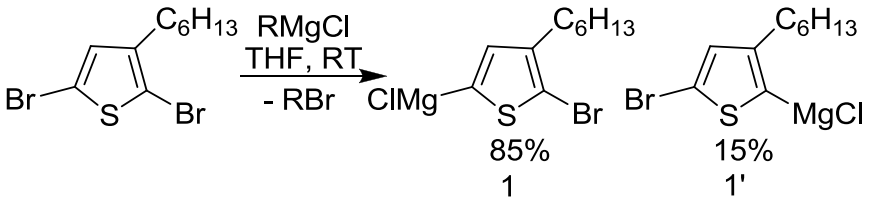

Scheme 2a. Grignardizing 2,5-Dibromo-3-hexylthiophene[2]

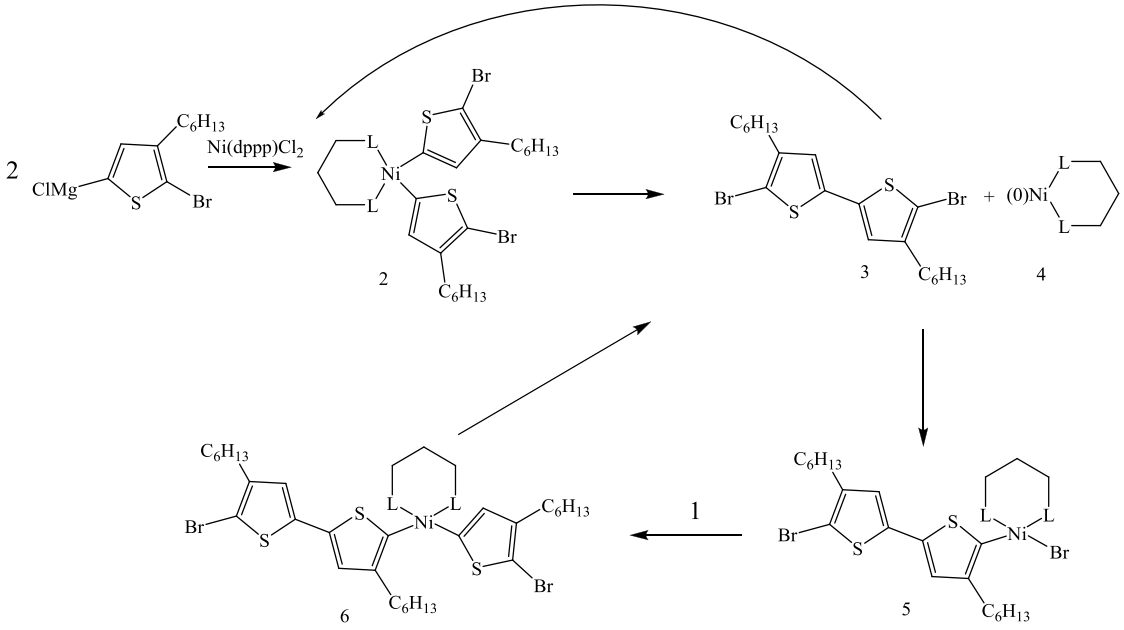

Scheme 2b. GRIM Mechanism as Proposed By Rawlins' Group[11]

Summary

The mechanism of Grignard metathesis polymerization for 3-hexylthiophene was investigated and evidence was proposed that the mediating nickel species diffuses from chain to chain throughout the reaction. The diffusion of the nickel species indicates a loss of uniform chain ends; however, it does not correspond directly to a loss in molecular weight control or regioregular control. Molecular weight was controlled by monomer to nickel ratio and initial monomer molarity, with the latter dominating under these conditions. A combination of polymerization kinetics, molecular weight monitoring and end-group analysis after methanol and HCl quenching confirm an alternative mechanism of polymerization. This alternative mechanism offers insight into controlling final molecular weight and achieving greater control over the resulting polymer architecture, i.e., regioregularity. Understanding the operating mechanism is useful in future work, where polymerization will be quenched for subsequent reaction/functionalizations which will allow application in advanced material products.

REFERENCES

1. Loewe, R. S.; Khersonsky, S. M.; McCullough, R. D. *Advanced Materials.* **1999,** 11, 250-253.
2. Iovu, M.; Sheina, E.; Gil, R.; McCullough, R. *Macromolecules.* **2005,** 38, 8649-8656.
3. Miyakoshi, R.; Yokoyama, A.; Yokozawa, T. *Journal of American Chemical Society.* **2005,** 127, 17542-17547.
4. Liu, J.; Loewe, R.; McCullough, R. *Macromolecules.* **1999,** 32, 5777-5785.
5. Jeffries-El, M.; Sauve, G.; McCullough, R. *Advanced Materials*. **2004,** 16, 1017-1019.
6. Caruso, A. N.; Feng, D. Q.; Losovyj, Y. B.; Schulz, D. L.; Balaz, S.; Rosa, L. G.; Sokolov, A.; Doudin, B.; Dowben, P. A. *Physica Status Solidi.* **2006,** 243(16), 1321-1330.
7. Ukai, S.; Ito, H.; Marumoto, K.: Juroda, S. *Journal of the Physical Society of Japan.* **2005,** 74(12), 3314-3319.
8. Chen, T.; Wu, X.; Rieke, R. *Journal of American Chemical Society.* **1995,** 117, 233-244.
9. Holdcraft, S. *Journal of Polymer Science Part B: Polymer Physics.* **1991,** 29(13), 1585-1588.
10. Miyakoshi, R.; Yokoyama, A.; Yokozawa, T. *Macromolecular Rapid Communications.* **2004,** 25(19), 1663-1666.
11. Achord, B. C.; Rawlins, J. W. *Macromolecules.* **2009,** 42(22), 8634-8639.

CHAPTER V

END-CAPPING OF P3HT AND SITE TRANSFORMATION FOR ADDITION OF PS:CMS BLOCK BY COUPLING AND SEQUENTIAL BLOCK GROWTH

Introduction

We have consistently pursued the end goal for an all in one donor-acceptor block copolymer. When considering the methodology for achieving the goal, two optional routes were shown feasible from prior chapters.

1. The first route involves the grafting of two completed polymer segments (grafting to); specifically, hydroxyl functional P3HT block and an acid functional polystyrene:chloromethyl/Buckminster Fullerene (PS:CMS:Fu) block.
2. The second route is sequential block growth (grafting from) from the original P3HT starting block material by nitroxide mediated polymerization of PS/CMS and subsequent addition of Buckminster Fullerene.

The research in this chapter focuses specifically on the examination of precursors for each route independently, i.e., functionalization of P3HT for subsequent growth or grafting and the small molecule synthesis required for these steps. The functionalization of the acceptor block (2^{nd} block) for the grafting to route and will be described in the following chapter, and the final coupling reactions and block copolymer growth will be discussed in Chapter VII. Below are summarized the variety of methods and results for each possible route at the time of this writing.

Combined research and development from our efforts and previously performed investigations specific to the mechanism of Grignard Metathesis polymerization for P3HT have confirmed that end-capping or functionalization can occur efficiently when Grignardized end-capping reagents are used. [1] The end-capping methodology can, in theory, be beneficial for both preparation of P3HT for subsequent end-group focused reactions as well as preparing the P3HT segment as a macroinitiator. This chapter summarizes the results for the procedures, efficiency and characterization of vinyl termination of P3HT. The main protocol was end-termination via vinylmagnesium bromide, subsequent hydroboration-oxidation of the vinyl end-group, quenching with a Grignardized Nitroxide Mediated Polymerization (NMP) initiator (as well as the synthesis of the initiator) and Heck-Coupling reaction of the vinyl group with a previously synthesized NMP initiator (also reviewed in this chapter).

Grignard Metathesis End-Capping Reactions

Synthesis of (2-Phenyl-2-(2,2,6,6-tetramethylpiperidin-1-yloxy)ethyl) Magnesium Bromide (Grignard Metathesis end-capping reagent)

The synthetic procedure to produce (2-Phenyl-2-(2,2,6,6-tetramethylpiperidin-1-yloxy)ethyl) magnesium bromide is very detailed in Chapter II, while Scheme 3 below, illustrates the reaction scheme for the first step which generates an *in situ* intermediate. As represented in the reaction scheme the synthesis proceeds by a two-step process, 1-(2-bromo-1-phenylthoxy)2,2,6,6-tetramethylpiperidine was isolated by washing and recrystallization from methanol as mentioned in Chapter II.

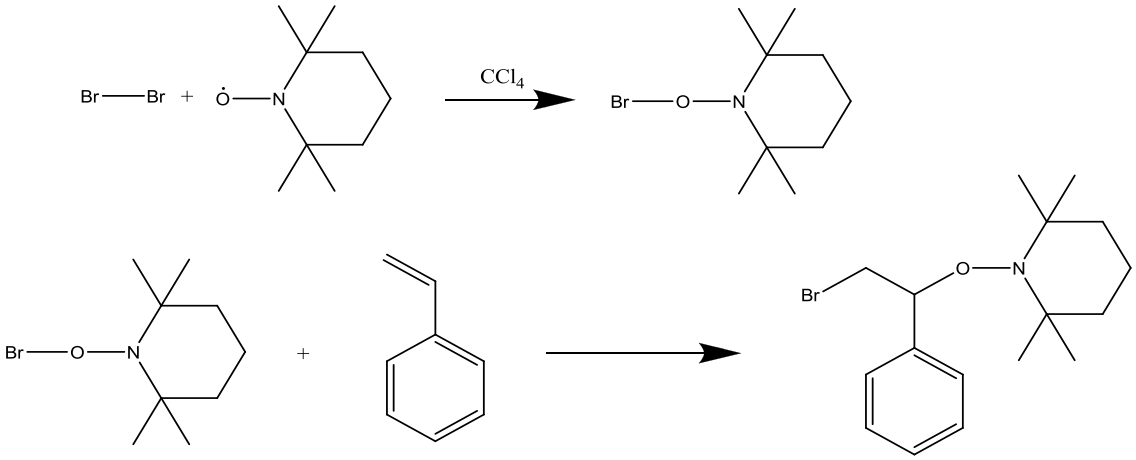

Scheme 3. Synthesis of 1-(2-bromo-1-phenylthoxy)2,2,6,6-tetramethylpiperidine.

Prior to recrystallization, the product was analyzed by GC-MS, ^{13}C and ^{1}H NMR for purity, the results of these analyses are shown in Figures 55, 56 and 57 respectively. The characterization revealed that there were multiple potential side reactions occurring during the synthesis. A few of the major side reaction products include: dibrominated styrene (Figure 58a), oligomeric styrene species [dibrominated (Figure 58b) or TEMPO functionalized (Figure 58c)] in combination with the desired product. Conventionally, species consisting of two additions of TEMPO are avoidable and absent from the possible side products as the stability of the TEMPO radicals towards double bonds discourages the adduct formation. The product was then separated by washing and recrystallized, post washing and recrystallization the product was once again analyzed by ^{1}H NMR and yielded high purity products, shown in Figure 59. The styrene adduct was then Grignardized by the addition of mechanically activated magnesium turnings. [2] In this process, magnesium turnings are stirred under a nitrogen atmosphere with a mechanical stirrer in a glass round bottom flask, the flask and stirrer were in turn coated with magnesium oxide that was located on the surface of the turnings.

The removal of the magnesium oxide layer exposes pure activated magnesium species; these turnings are then added to the styrene:TEMPO adduct in THF at 35ºC for three hours. The Grignardized species was used as the end-capping agent, which will be discussed in the subsequent section.

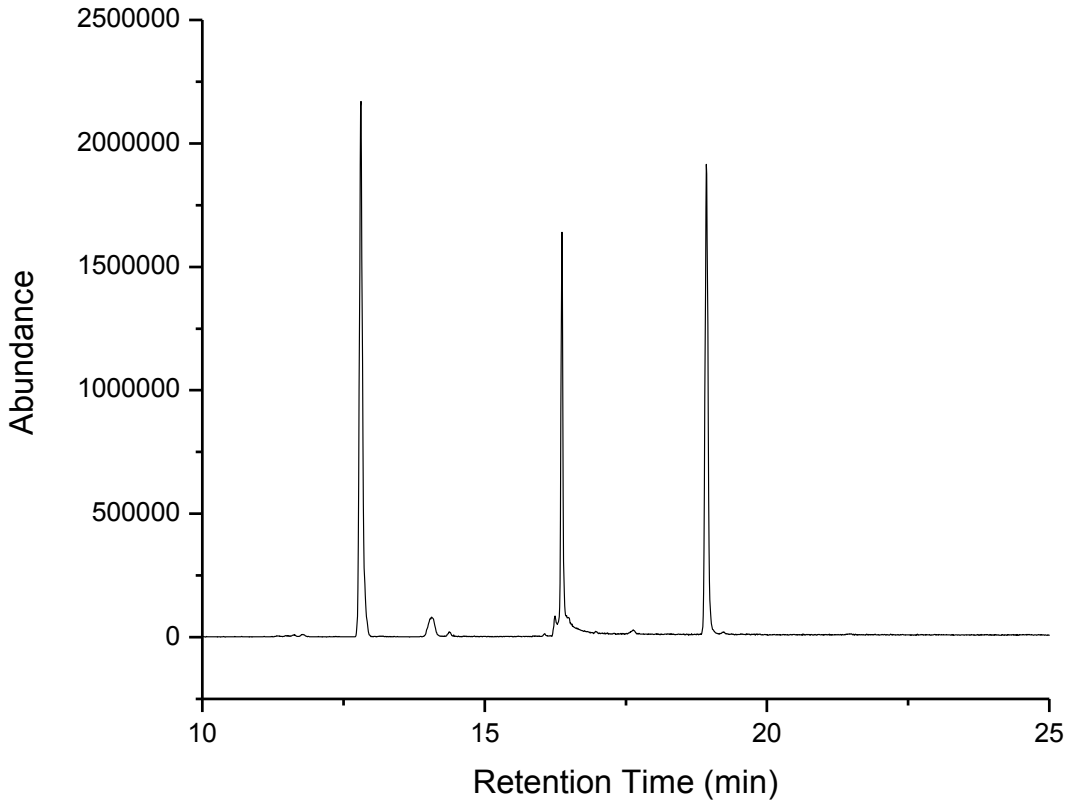

Figure 55. GC-MS of product prior to washing and recrystallization.

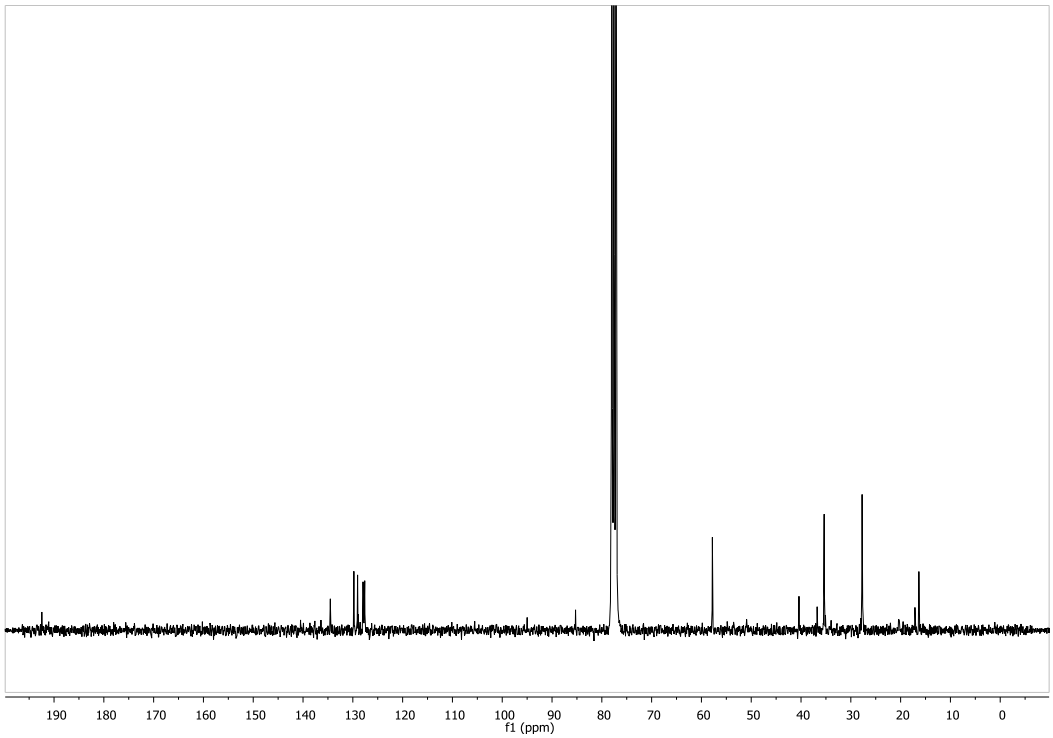

Figure 56. ^{13}C NMR of product prior to washing and recrystallization.

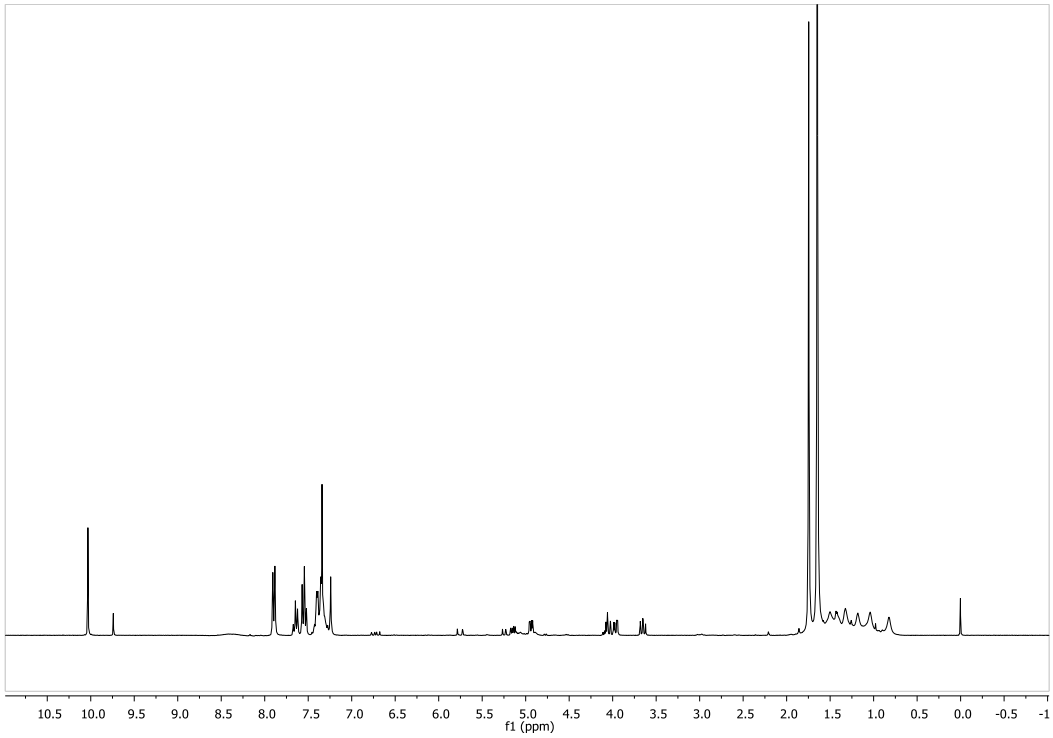

Figure 57. ^{1}H NMR of product prior to washing and recrystallization.

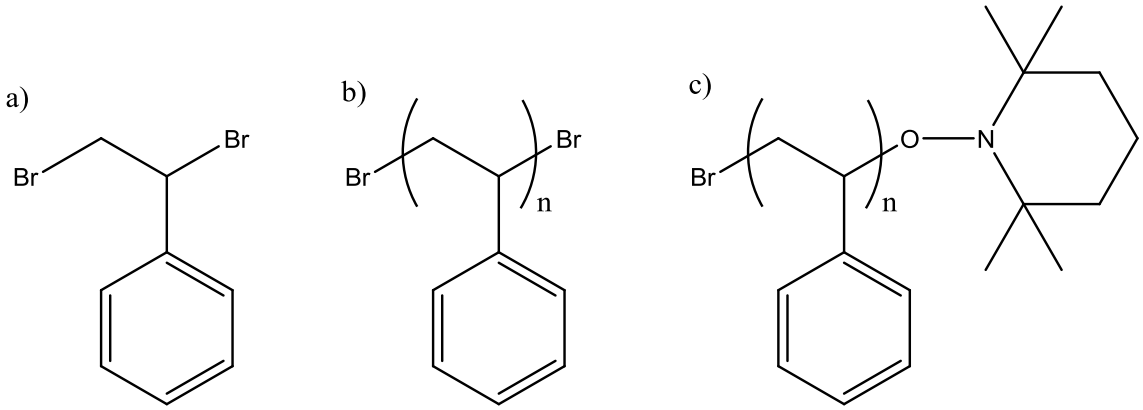

Figure 58. Possibly side reactions a) dibrominated styrene b) dibrominated oliogmeric species c) TEMPO functionalized oligomer.

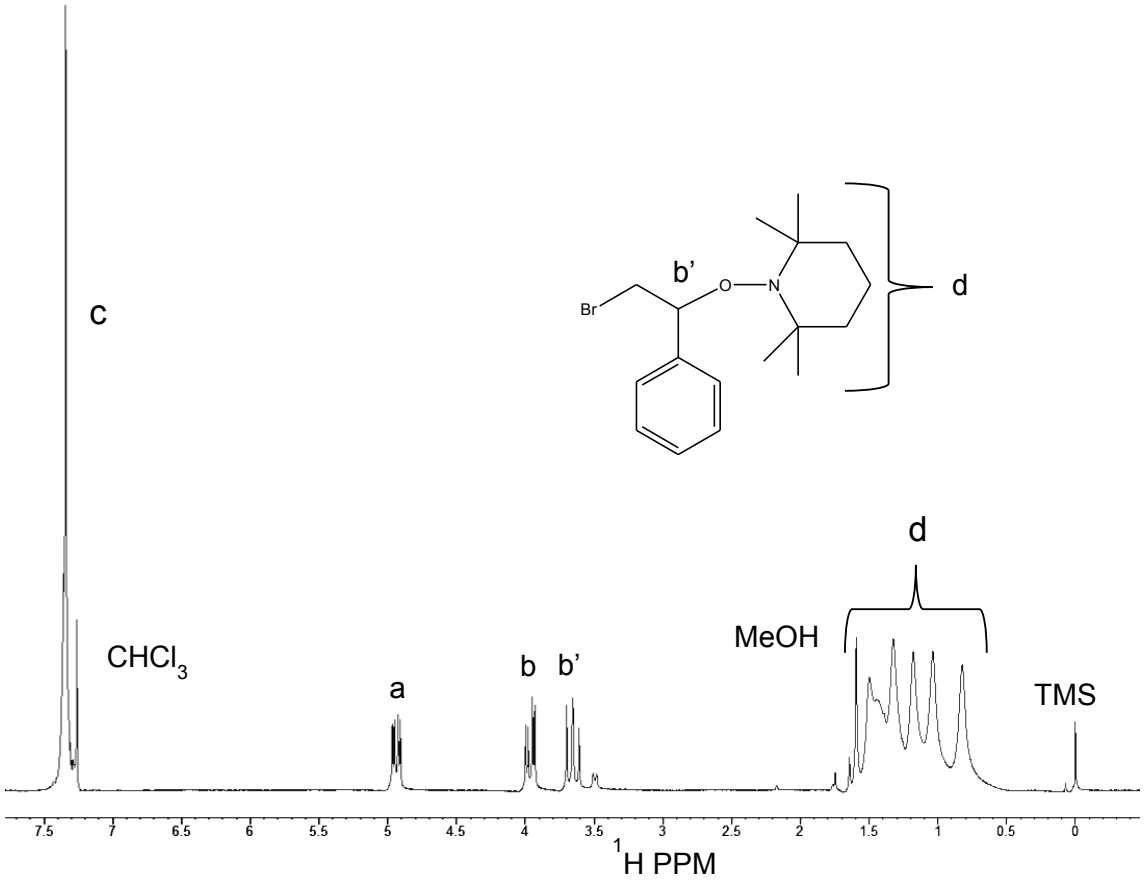

Figure 59. ^{1}H NMR of purified (2-Phenyl-2-(2,2,6,6-tetramethylpiperidin-1-yloxy)ethyl) magnesium bromide.

Quenching Reactions

The quenching step of P3HT synthesis using the synthesized and purified (2-Phenyl-2-(2,2,6,6-tetramethylpiperidin-1-yloxy)ethyl) magnesium bromide or vinyl magnesium bromide was performed according to the procedure listed in *Chapter 2, Section 2.2.5.* Our hypothesis was that several variables were critical for high efficiency quenching addition. The objective was to prove which variables were most important starting with the timing of the quenching reagent addition to the reaction mixture and also assessing quenching reagent to nickel species ratio(s).

P3HT quenching reactions have been shown successful in many literature references with multiple functional and non-functional quenching agents. [(1)] The starting choice of quenching agent for our studies was vinylmagnesium bromide. Our logic was as follows; the resulting vinyl functionality offers a variety of further reaction schemes once completed in high yield, and most importantly for this work, the conversion of the vinyl group optionally to a hydroxyl or subsequent Heck coupling reactions. Studies involving both quenching time and quenching agent to nickel ratios were investigated; Table 7 below summarizes the reaction conditions for *in-situ* quenching and molar ratios of a few selected reactions at varying target molecular weight.

Table 7

Formulation and Reaction Conditions For Vinyl End-Capping

Monomer:Nickel Ratio	End-Capping Reagent:Nickel Ratio	Relative End-Capping Addition Time (min)	Mn (gm/mole)	Percent End-Capped
60	3	15	4,760	89.4
60	3	120	6,740	84.6
60	10	15	4,910	75.6
60	10	120	7,150	66.3
75	3	15	7,420	91.2
75	3	120	8,260	90.6
75	10	15	7,650	62.4
75	10	120	8,190	59.5
100	3	15	9,330	90.8
100	3	120	10,900	86.1
100	10	15	94,70	50.8
100	10	120	11,200	56.4

Our hypothesis was that several critical reaction parameters would shift end-capping percentage drastically, a contradiction to findings by other researchers in the literature. [1, 3] Using the data to consider above the efficiency of end-capping and molecular weight values, optimized reaction conditions were deduced. A combination of molecular weight values and the end-capping percentage revealed the conditions to be most favorable at 1.1:1 (excess of) end-capping agent to theoretical number of chain ends (1.5 - 5.5 chains per Nickel depending on initiation time). Surprisingly, when excess quenching agent was added, the results revealed less efficient end-capping had occurred. These data points support the potential binding of nickel species to the end-capping reagent,

instead of activating and coupling as necessary with the polymer chain ends for functionalization.

Results compiled in Table 7 were calculated via the combination of the corrected GPC molecular weight data and the ^{1}H NMR data with the peaks of interest in NMR. The peaks of interest were located at 5.5 and 5.1 ppm for the vinyl protons and 7.0 ppm for P3HT, specifically monitoring the proton located in position 4 of the thiophene ring. The integrated peak values were used in Equation 2 to calculate the percent end-capped chains. The equation effectively equates the integrated value of one chain of P3HT (based on the degree of polymerization) to one vinyl group. Complications for the accuracy of this equation are specific to the presence of one vinyl group proton being located in the area of the thiophene ring proton. In order to compensate for the side product presence, the value of the other two vinyl protons was divided by two and subtracted from the overall integrated value for the thiophene ring. Figure 60 summarizes an example ^{1}H NMR with peak assignments for integration areas shown.

$$\%EndCapped = \frac{0.5 \times Area\ Vinyl\ Peaks}{\left(\frac{Area\ P3HT\ Peak - \frac{Area\ Vinyl\ Peaks}{2}}{DP}\right)} \times 100$$

Equation 2. Percent vinyl functionalization via GPC and NMR results.

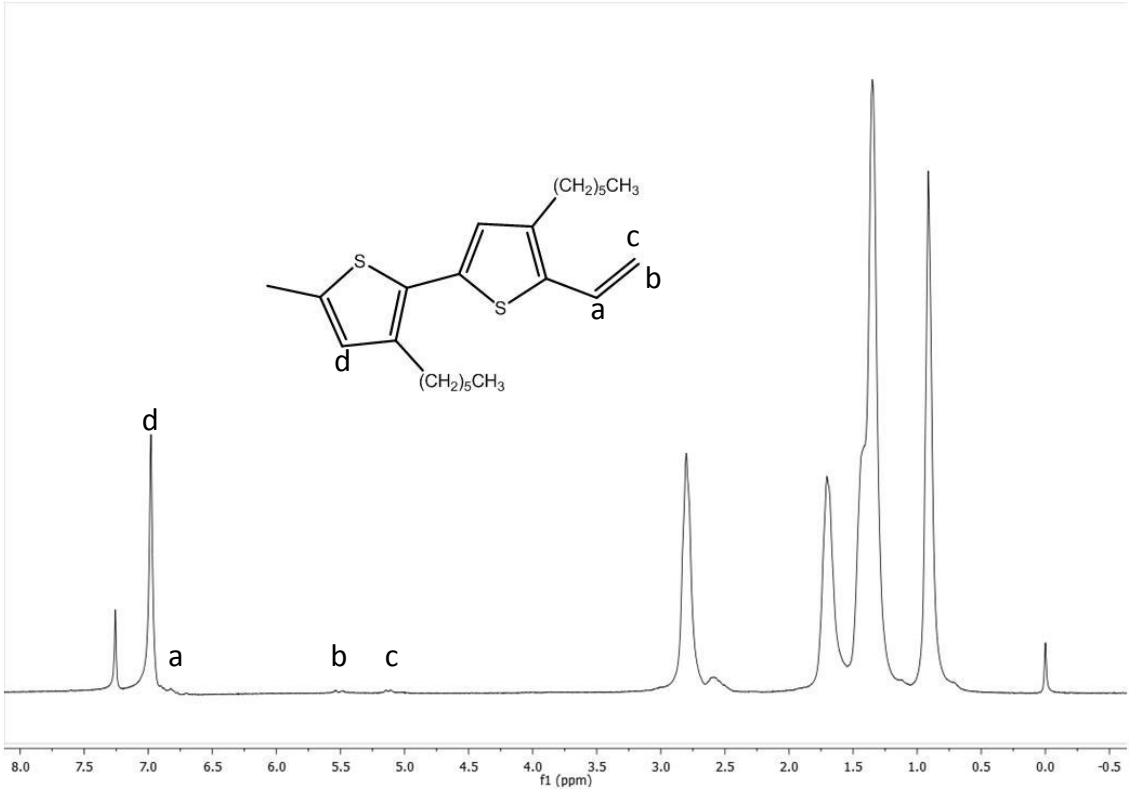

Figure 60. ^{1}H NMR with peak assignments of vinyl end-capped P3HT.

The reactions with (2-Phenyl-2-(2,2,6,6-tetramethylpiperidin-1-yloxy)ethyl) magnesium bromide resulted in limited or no quenching as shown by ^{1}H NMR (Figure 61) and collected molecular weight data singularly and in combination. From our data it was suspected that the Grignardization step with the quenching reagent was either incomplete, or the reagent was over indexed so excessively, that the nickel bound with quenching reagents instead of transferring to chains ends and promoting efficient end-capping reactions. The procedure and the resulting misstep was found to be the most common protocol in the literature as the conversion of the Grignard species is difficult to confirm without air exposure and the exposure renders the system useless (our procedure included *in situ* ATR-FTIR). From our characterization, the ^{1}H NMR spectrum was the most

convincing set of data, representing poor end-capping efficiency in combination with quantitative end-group integration and molecular weight data.

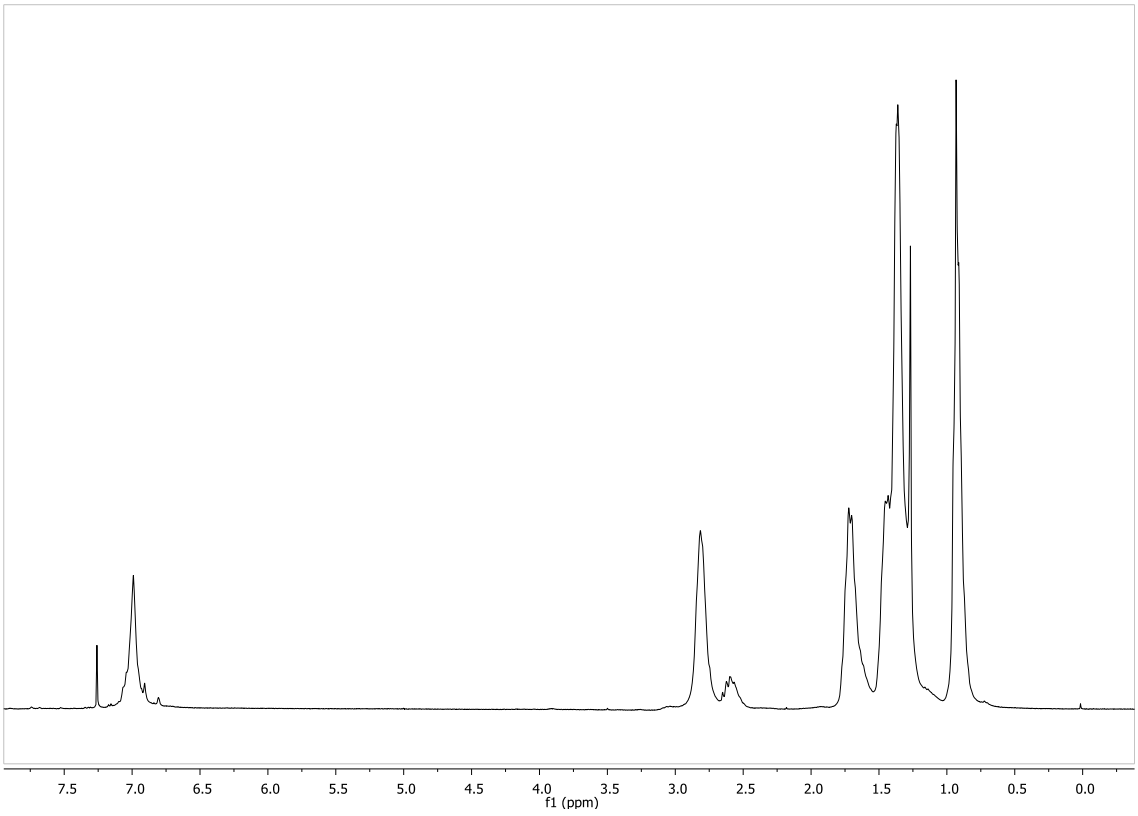

Figure 61. ^{1}H NMR of P3HT after quenching with (2-Phenyl-2-(2,2,6,6-tetramethylpiperidin-1-yloxy)ethyl) magnesium bromide.

The data, from Figure 61, represents the most successful quenching attempts and was performed at theoretical ratios of 1:4 nickel to quenching agent, the lowest of the theoretical ratios that was attempted. The results also support a process whereby binding of nickel to quenching agent combined with little or no coupling. These results are also supported by the lack of styrenic peaks located at 4.89 ppm, representing the benzylic proton adjacent to TEMPO. This particular set of conditions resulted in a polymer with 1% or less end-functionality at a molecular weight of 9,000 g/mole and a ratio of peaks located at

4.89 ppm (TEMPO from Styrene peak) and 2.8/2.6 ppm (P3HT), where percent end-capped chains were calculated according to Equation 3.

$$\%EndCapped = \frac{Area\ Styrenic\ Peak}{\left(\frac{Area\ P3HT\ Peaks}{DP}\right)} \times 100$$

Equation 3. Percent end-functionalization by NMR and GPC results.

Hydroboration/Oxidation of Vinyl-P3HT

Once P3HT was confirmed, via characterization, to be efficiently end-capped with vinyl functional groups, the resulting polymer was further reacted in preparation for coupling reactions with acid functional statistical copolymer, polystryrene:chloromethylstyrene/fullerene. For the series described immediately below, the vinyl group was functionalized to a hydroxyl group via a hydroboration/oxidation reaction, the more detailed descriptions of the experimental set up can be found in Chapter II, Hydroboration/Oxidation of Vinyl P3HT. The reaction mechanism for the hydroboration/oxidation has been shown to be quite complex and is summarized in Scheme 4 below and outlined in the text here.

1. The first step has been described most accurately (in the authors opinion) as involving a four atom center-based reaction. The addition across the double bond, commonly it is thought that the higher substituted carbon accepts electrons from the boron-hydrogen bond and the double bond donates to the Boron in return.
2. Secondarily, a hydroperoxy anion adds to the boron species followed by an alkyl (carbon center) migration (rearrangement) to the oxygen, which simultaneously involves the extradition of a hydroxide anion. The

hydroxide anion will then add to the boron species which donates back to the oxygen generating an oxy anion. In the final step, the oxy anion abstracts a proton from water to create a hydroxyl and regenerate the anion.

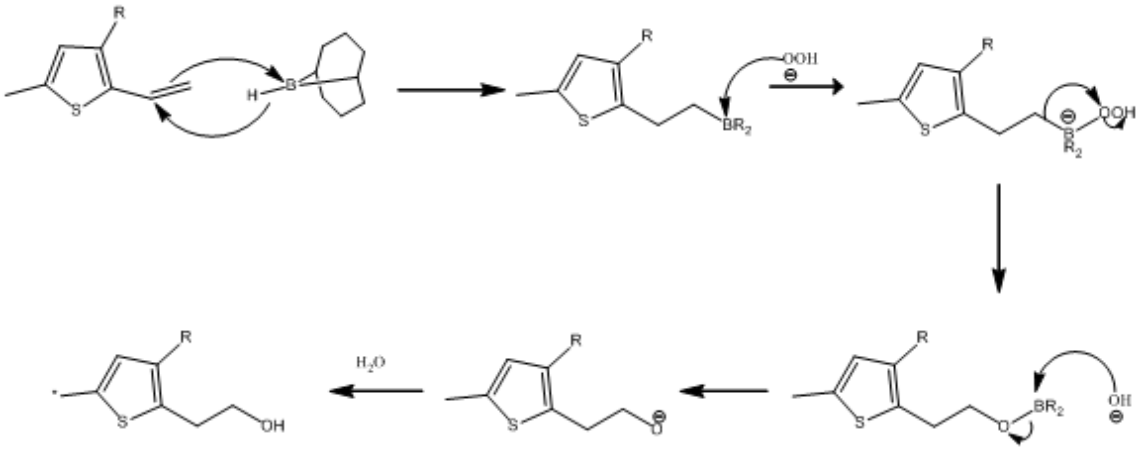

Scheme 4. Mechanism of Hydroboration/Oxidation of Vinyl P3HT

After the resulting polymer was precipitated, ^{1}H NMR was used to verify the conversion of the vinyl group to a hydroxyl group. The loss of peaks at 5.1 and 5.5 are indicative of vinyl group conversion. These peak changes combined with new peaks at 3.6 and 2.7 ppm (covered by the P3HT peaks) correspond to the presence of a new hydroxyl. Figure 62 illustrates the resulting NMR spectrum for the hydroboration reaction.

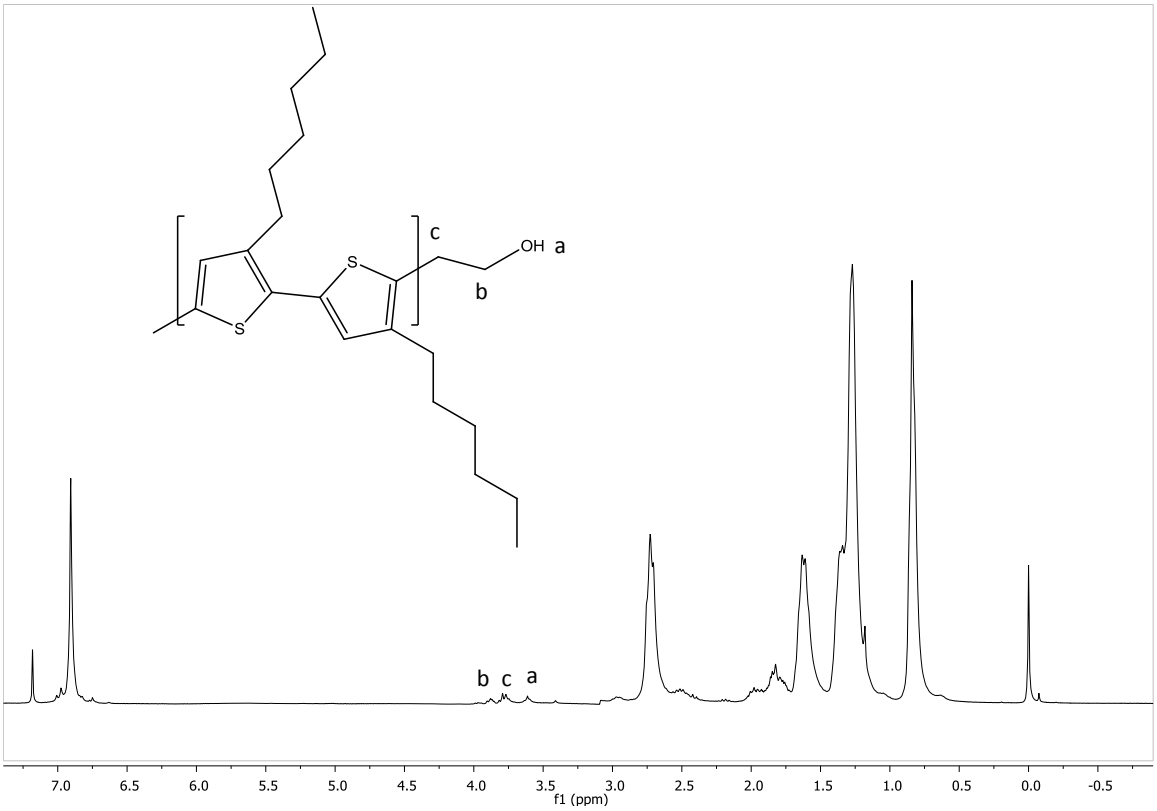

Figure 62. ^{1}H NMR after Hydroboration/oxidation of vinyl-P3HT.

We used a modified version of Equation 2 to calculate the percent of chain ends that were functionalized to hydroxyl groups. Modified Equation 2 was produced by replacing the vinyl peak area with the area of the peak located at 3.6 ppm and becomes specific to the area related to a single hydroxyl group. This substitution simplified the equation by eliminating overlapping peaks, and resulted in Equation 4 shown below (the method was consistently shown to be effective for each of the resulting polymers, both on a series of end functional materials within the scope of this dissertation and to be further confirmed by grafting efficiency versus homopolymer in GPC data after copolymer coupling reactions are completed).

$$\%Hydroxyl\ Functional = \frac{Area\ @\ 3.6\ ppm}{\left(\frac{Area\ P3HT\ Peaks}{DP}\right)} \times 100$$

Equation 4. Percent hydroxyl functionalization via GPC and NMR results.

Using Equation 4, integration values and GPC data for the example show above, the resulting percent hydroxyl functional chains was 81.4%. Within the entire set of hydroboration experiments, the percent hydroxyl functional polymer chains ranged narrowly between ~80% to 95% hydroxyl functional. The data confirm that some chains, albeit in varying percentages, were non-functionalized chains. However, these levels are considered acceptable for our end goal of study, i.e., the preference is to have only functionalized chains but regarding homopolymer effects on block copolymer morphology the achieved end functionalization levels are tolerable for the intended purposes. The details for the resulting materials are discussed in greater detail in Chapter VII.

Preparation of Heck-Coupling Precursor and Heck Coupling Reaction

The polymer end-groups required an additional functionalization step, in order to prepare P3HT for sequential block addition. This section describes the results for the attempts to functionalize the vinyl group, through the synthesis of a nitroxide mediated polymerization precursor, specifically one suitable for Heck Coupling reactions. The procedure for the precursor synthesis, (1-(1-(4-bromophenyl)ethoxy)-2,2,6,6-tetramethylpiperidine) was explained in detail in Chapter II and consisted of two separate synthetic steps.

1. Hydrobromination of para-bromostyrene

2. Subsequent addition of TEMPO through copper mediated extraction of the non-aromatic bromine

The synthesis started with hydrobromination of *p*-bromostyrene, and the resulting product was purified by vacuum distillation. The synthesis yielded 58% of the desired and final product after purification. The ^{1}H NMR of the product is shown below (Figure 63). The peak assignments for the 5.1 ppm-centered quartet were the main focus. The set of peaks corresponds to the protons on the carbon adjacent to the added bromine. Further, the residual styrene was identified by the small, yet detectable peaks at 5.25 and 5.75 ppm that confirm the presence of vinyl functionality, i.e., starting materials.

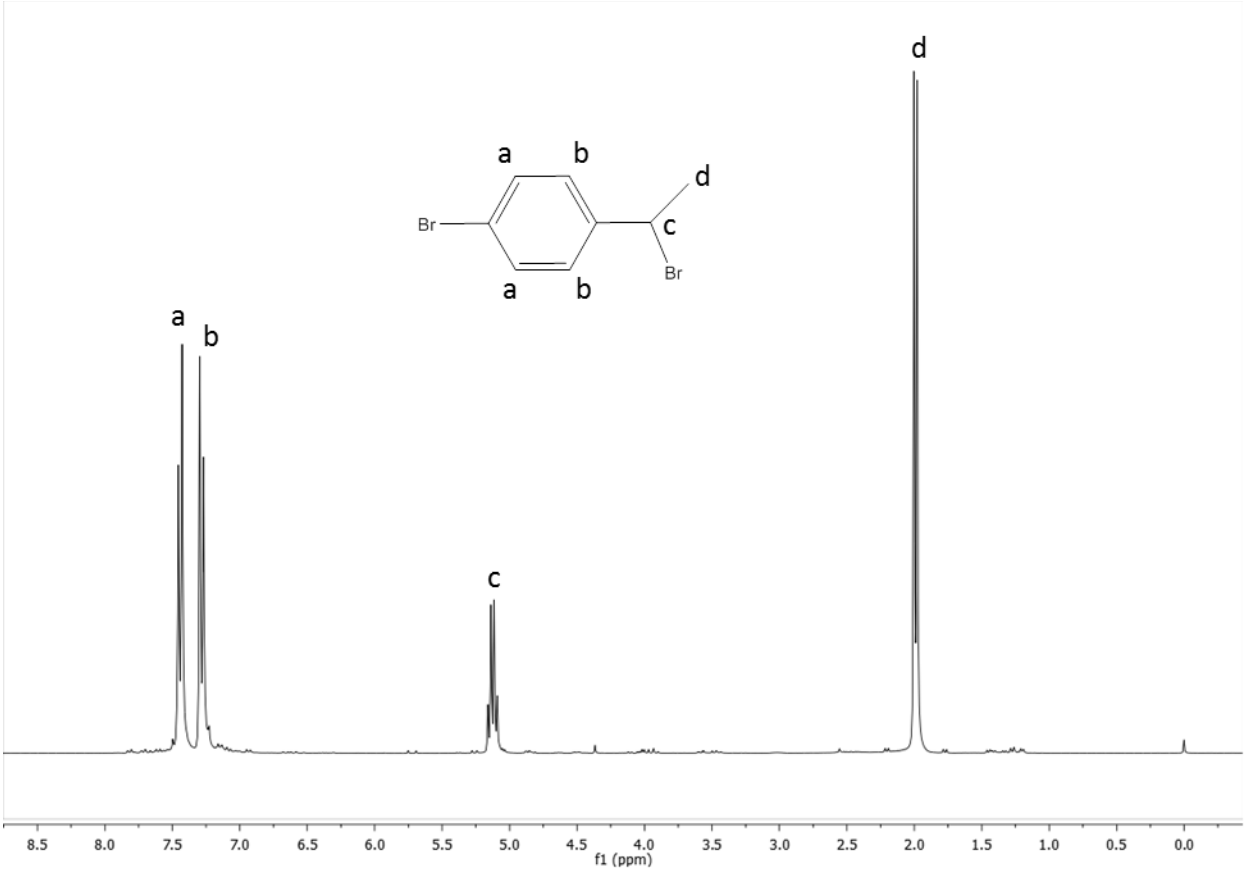

Figure 63. ^{1}H NMR of 1-bromo-4-(1-bromoethyl)benzene.

The second synthesis step focused on the copper mediated substitution of TEMPO using aliphatic bromine. Previous researchers have confirmed that the successful reaction would result in an up-field shift between the 5.1 ppm-centered peak and the additional peaks represented in the appearance of new aliphatic protons. Figure 64 below illustrates the first ^{1}H NMR acquired for this reaction product(s); however, it is critical that we observed an aromatic proton present that revealed another TEMPO substituted position as supported by the up field shift of the aromatic protons labeled as peak “a” in Figure 63 above.

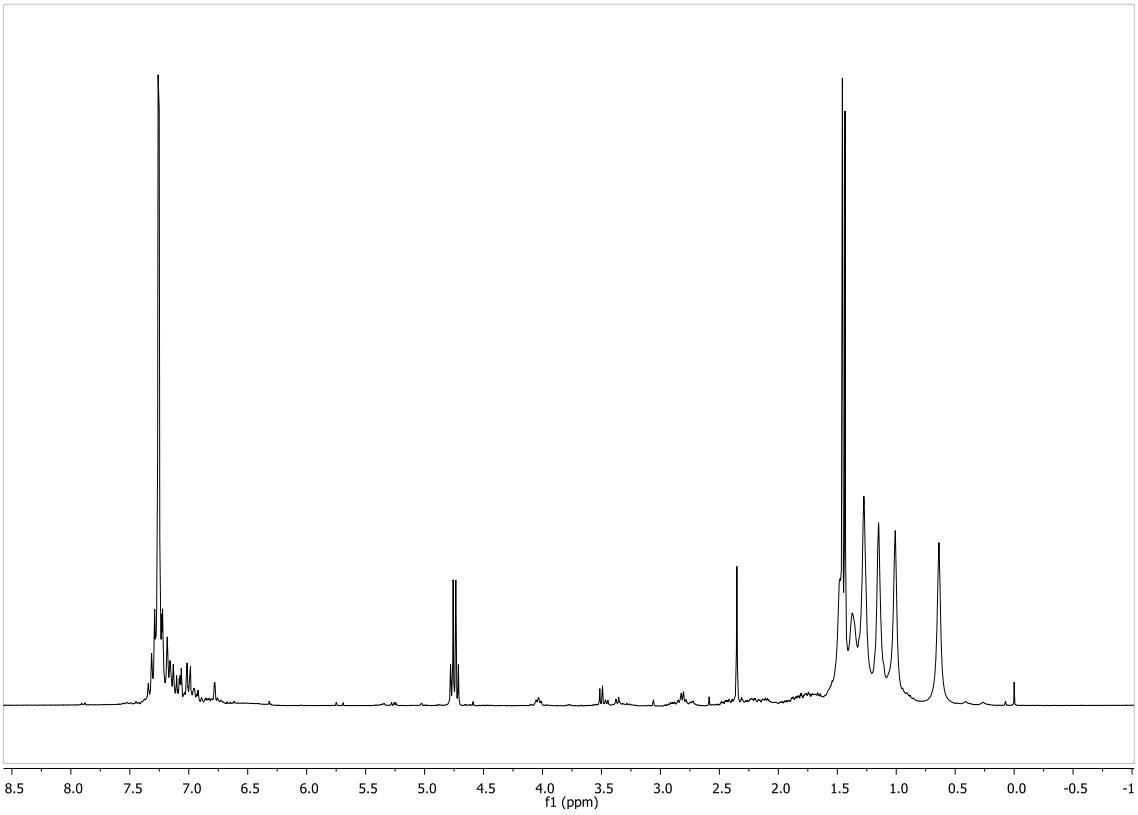

Figure 64. ^{1}H NMR of 1-(1-(4-bromophenyl)ethoxy)-2,2,6,6-tetramethylpiperidine.

Finally, a Heck Coupling reaction was performed with vinyl functional P3HT and 1-(1-(4-bromophenyl)ethoxy)-2,2,6,6-tetramethylpiperidine following the details presented in Chapter II. The resulting polymer was examined by ^{1}H

NMR and yielded little to no coupling of the nitroxide species. Figure 65 below illustrates the NMR spectrum of the reaction product. Moreover, the critical point should be made, that no TEMPO peaks were found in these products and the purification process utilized for this synthesis preparation have consistently removed non-reacted species and catalyst, i.e., precipitation and filtering process.

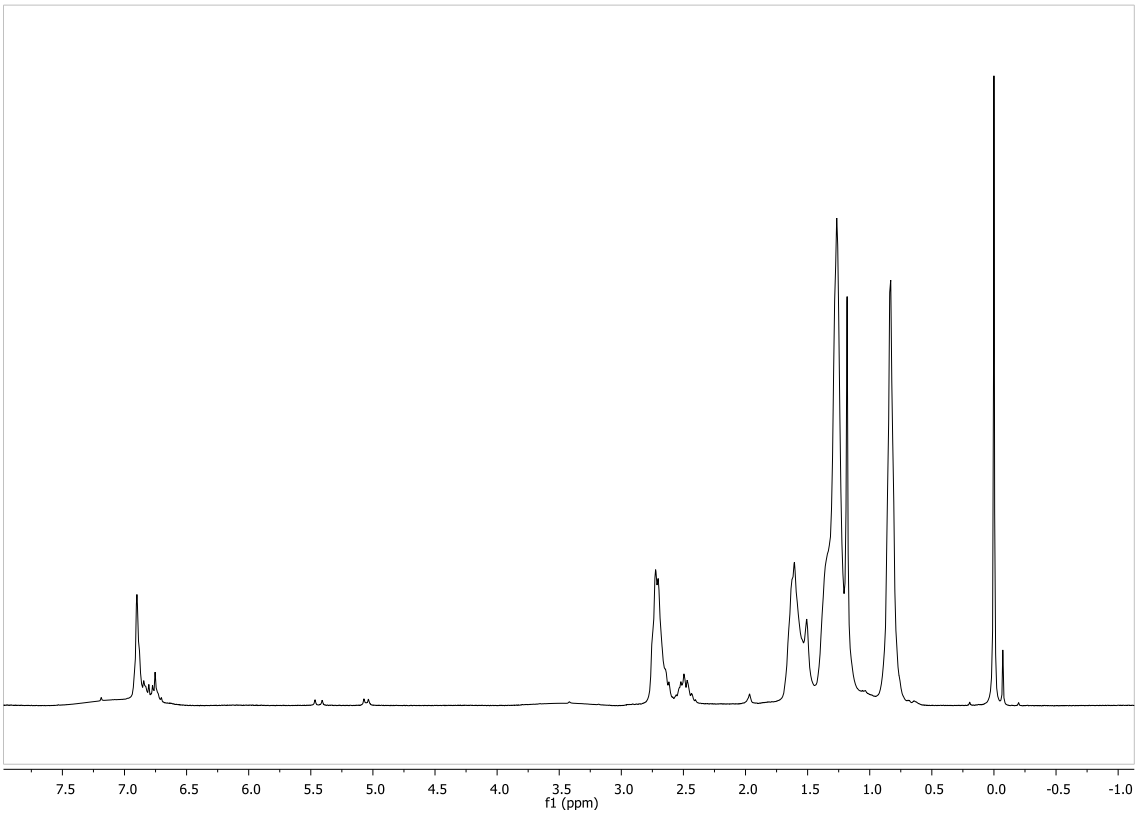

Figure 65. ^{1}H NMR of P3HT after reaction with 1-(1-(4-bromophenyl)ethoxy)-2,2,6,6-tetramethylpiperidine.

Summary

Investigated herein, were the end-capping reactions of the Grignard Metathesis polymerization of 2,5-dibromo-3-hexylthiophene, with both commercially available vinyl magnesium bromide and a synthesized Grignard

reagent. The end-capping reactions proved to be efficient using vinyl magnesium bromide. On the contrary, the synthesized Grignard species did not end-cap sufficiently for detection using ^{1}H NMR. The absence of end-capped species from this particular synthesis method was theorized as either, the lack of complete Grignardization before addition or the over-indexing and strong complexation with the nickel catalyst species as an alternative to functionalization.

Several additional methods were attempted towards efficient end-capping. Subsequent transformation reactions were also examined, including hydroboration/oxidation reactions for block-block coupling reactions and heck coupling modifications for sequential block growth. The hydroboration/oxidation reactions proved to be efficient, converting up to 95% of the available vinyl groups to hydroxyl groups. Unfortunately under our conditions, the heck-coupling reaction was inefficient and yielded mixed products. The data leads us to believe that additions across the thiophene rings as well as addition of TEMPO to both brominated sites were conflicting side reactions.

REFERENCES

1. Jeffries-El, M.; Sauve, G.; McCullough, R. D. *Advanced Materials.* **2004,** 16(12), 1017-1019.
2. Baker, K. V.; Brown, J. M.; Huges, N.; Skarnulis, A. J.; Sexton, A. *Journal of Organic Chemistry.* **1991,** 56, 698-703.
3. Jeffries-El, M.; Sauve, G.; McCullough, R. D. *Macromolecules.* **2005,** 38, 10346-10352.

CHAPTER VI

SYNTHESIS OF ACID FUNCTIONAL POLYSTYRENE:CHLOROMETHYL STYRENE AND P3HT:PS:CMS

Introduction

The prior chapter described the successful synthesis of a donor polymer segment completing the first of two blocks towards a final block copolymer. In this chapter, our focus was the acceptor block and critical characteristics for the functional homopolymers as well as the sequential block growth starting from the donor P3HT material. The first chapter section focused on the distinct and important first synthesis step for the functional donor material, ultimately containing a controlled ratio of Buckminster Fullerene. Described herein are the statistical copolymerization results of styrene and chloromethyl styrene (CMS) using both macroinitiator and azo-initiators. The statistical copolymers of styrene and CMS offer several advantages when employed as the host material for Buckminster Fullerene containing polymers and the acceptor block in organic photovoltaics. The copolymerization of styrene and CMS has two main advantages:

1. The monomers possess similar reactivity ratios that allowed feed and composition to be closely matched and monitored (^{1}H NMR integration techniques confirmed these ratios).
2. Similar reactivity ratios enable the styrene:CMS ratio within the polymer to be tailored by adjusting the relative molar proportions and ultimately direct functional control for the Buckminster Fullerene content.

The copolymers are easily processed using solvent or thermal methods allowing more versatility in further experiments when the reaction conditions are more stringent and the overall process-ability is hindered by the less soluble and more difficult to handle donor block (P3HT).

Styrene-CMS copolymers have been polymerized by radical, ionic and metal mediated systems. Radical polymerization appeals to our end goals via its ease of preparation and simple modification of the final polymer molecular weights through monomer-to-monomer and monomer-to-initiator ratios. Conventional free radical techniques offer the ability to reach target molecular weight averages; however, they produce polymers possessing higher polydispersity indexes. Advancements in the area of controlled free radical systems such as nitroxide mediated polymerization (NMP), atom transfer radical polymerization (ATRP), and reversible addition fragmentation chain transfer (RAFT) polymerization have facilitated both molecular weight control and low polydispersity. The following sections discuss the conventional polymerization of styrene and CMS as compared with TEMPO mediated NMP as well as initiation from the macroinitiator mentioned in the previous chapter.

Nitroxide Mediated Polymerization

Each of the current living free radical polymerization techniques, including nitroxide mediated polymerization, operates upon the same basic principle, i.e., maintain an instantaneous and reduced concentration of active radicals at all times during polymerization. Reducing the active radical concentration directly reduces the rate of all forms of termination such as coupling or combination and

disproportionation. Scheme 5 illustrates the mechanistic steps for styrene required for successful living free radical polymerization (following initiation). For our purposes in this scheme, there are two more factors to be considered: reversibility of the termination step, and stability of the mediating species. When these two factors are successfully controlled, polymer chains are predominantly initiated by the initiating species and chain growth occurs in a living manner, allowing for well-defined polymer synthesis.

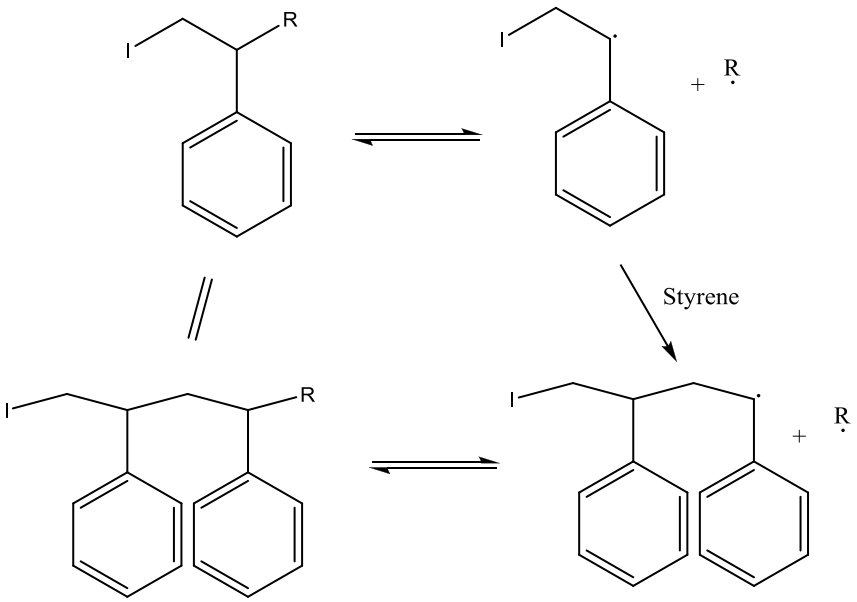

Scheme 5. Mechanism Of Operation For Living Free Radical Polymerization Where R Is A Mediating Species

For nitroxide mediated polymerization, the nitroxide or alkoxyamine mediating radical R has been widely studied. The pioneering work for NMP developed from quenching reactions; Solomon, Rizzardo and Moad [1] demonstrated that TEMPO would create a stable adduct and act as a radical trap at temperatures from 40-60ºC. Later, Moad and Rizzardo performed similar reactions at temperatures varying from 80-100ºC and observed low molecular

weight oligomers. The polymerization was not considered living conditions at these temperatures; however, the work did provide the foundation for future innovations and modifications to these experimental techniques, that once optimized, became the basis for free-radical living reactions. [2] Additional advances resulted in controlled radical systems, which have been most often defined by a first-order relationship of monomer conversion versus time. The relationship can be further exemplified by plots of number average molecular weight versus conversion. Figure 66 below illustrates this relationship for TEMPO-mediated polymerization of *n*-butyl acrylate.

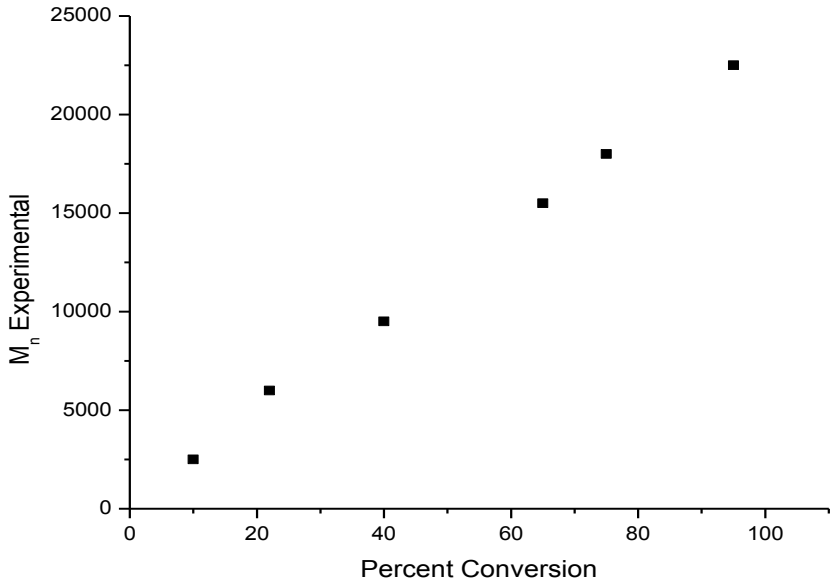

Figure 66. Number average molecular weight versus conversion for nitroxide mediated polymerization of n-butyl acrylate. [3]

NMP of styrene and CMS were of specific interest to our research as the ratio of styrene to chloromethyl styrene ultimately controls the fullerene incorporation level in the resulting acceptor donor block copolymer. Performing NMP of CMS requires consideration of certain side reactions involving the

chlorine as well as its relative rate towards styrene. Worthy of note, TEMPO mediated polymerization of CMS is reported to proceed faster than that of styrene due to a change in the equilibrium constant directly related to the electron withdrawing nature of the chlorine. This subtle but important difference can influence both the rate constant of coupling and rate constant of dissociation.[1, 2] At low ratios of CMS to styrene, the reactivity ratios are minimally affected and allow for random copolymers to be synthesized successfully.[3] However, several researchers have noted that when CMS is incorporated at higher ratios, the TEMPO-mediated polymerization of CMS yields polymers with higher polydispersities than that of styrene, suggesting that the benzylic site plays a role in side reactions.[4,7, 8] Lacroix-Demazes *et al.* suggested abstraction of benzylic hydrogen and chlorine by TEMPO as a possible source of side reactions.[7] The first would result in the consumption of an active chain and allow the consumption of TEMPO while the latter would generate a new chain that would grow under controlled conditions. It has been shown that low ratios of CMS in the initial feed reduce the effects of each of these side reactions, especially at monomer conversions below 75%.

Random Copolymerization of Styrene and CMS

The synthetic procedure for the random copolymerization of styrene and CMS was explained in detail in Chapter II, Nitroxide Mediated Polymerization of Styrene:Chloromethyl Styrene Copolymer. Variables that were adjusted for this chapter include:

- initiator [AIBN, 4,4'-azobis(4-cyanovaleric acid), or a macroinitiator]

- monomer-to-initiator ratio
- the presence or absence of TEMPO

The additional sections discuss our attempts to confirm increased control over polydispersity and molecular weight using TEMPO, with a comparison to AIBN, an acid functional initiator 4,4'-azobis(4-cyanovaleric acid), and an internally synthesized macroinitiator discussed in the previous chapter.

Small Molecule/Acid Functional Initiation with and without TEMPO

Systems initiated from both AIBN and 4,4'-azobis(4-cyanovaleric acid) were polymerized in bulk under two conditions: with and without TEMPO. The four synthetic variations were blended in equal molar monomer-to-initiator ratios and styrene to CMS ratios and then characterized. The AIBN initiated systems were attempted first. For these systems, the main point of interest for proof of effectiveness was the AIBN decomposition temperature range (102-104 ºC).[9] Targeted molecular weights were based directly on the monomer-to-initiator ratio, and the degree of polymerization is equal to the moles of monomer divided by two times the moles initiator (both initiators possess two radicals per mole). Table 8 summarizes both AIBN initiated systems in terms of target molecular weight, % CMS added to the formulation and actual molecular weight as measured by GPC and PDI.

Table 8

Styrene/Chloromethyl Styrene Formulations And Molecular Weight Results From AIBN Initiation

	Target MW (g/mole)	**% CMS in Formulation**	**Actual M_n (g/mole)**	**PDI**
AIBN without TEMPO	13,627	3.4	31,070	3.61
AIBN with TEMPO	17,550	3.4	16,400	1.14

As expected, the TEMPO mediated systems resulted in drastically reduced PDI and increased control towards targeted molecular weight. The higher molecular weight of the system in the absence of TEMPO was attributed to a larger variance for time of initiation, as well as, drastically more termination by coupling. GPC and ^{1}H NMR analyses were performed to quantify % CMS incorporation versus the feed percent. We hypothesized that the traditional radical polymerization would show insignificant changes in CMS-styrene content, whereas the TEMPO systems would exhibit a slightly higher CMS incorporation based upon the rate differential. ^{1}H NMR peak integration for CMS versus the benzylic proton in the main chain has been shown to match the copolymers final composition. Figure 67 is an example NMR spectrum with peak identifications. Equation 5 was used to quantify the percent CMS composition. In this equation, the benzylic proton signal associated to the CMS must be subtracted from the overall area of benzylic protons. To do this, the area associated to one proton from the methylene unit is equated to one benzylic proton and subtracted from the overall area.

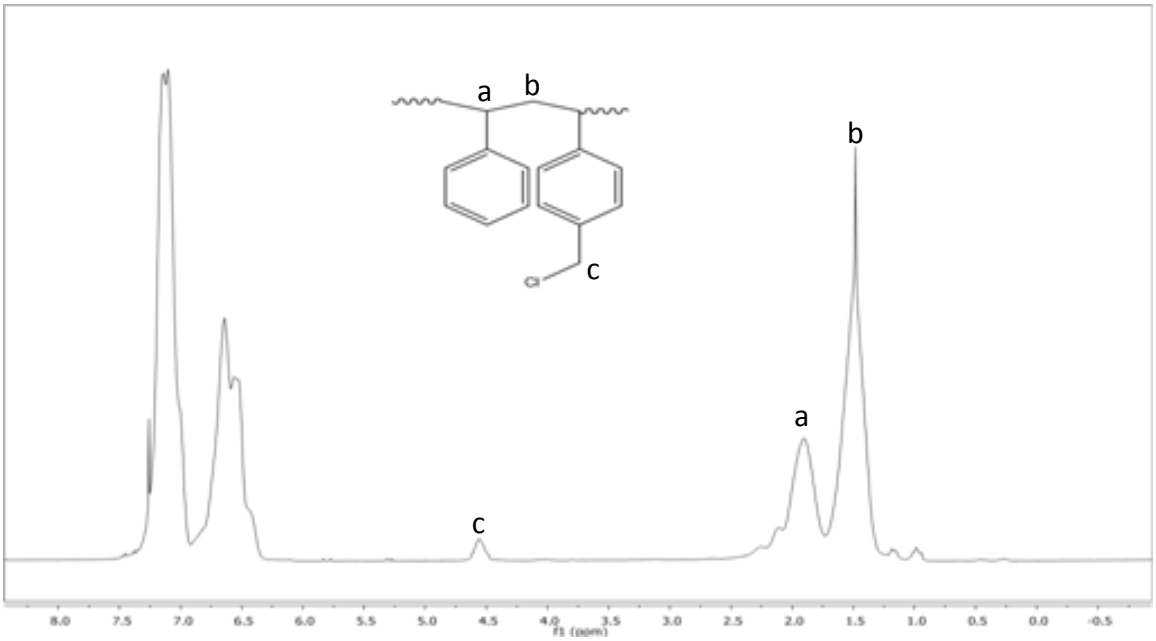

Figure 67. Representative ^{1}H NMR of copolymers of styrene and CMS.

$$\%CMS\ Incorporated = \left(\frac{\frac{Area\ @\ 4.6\ ppm}{2}}{\left(Area\ @\ 2.00\ ppm - \frac{Area\ @\ 4.6\ ppm}{2}\right)} \right) \times 100$$

Equation 5. Quantification of percent incorporation of chloromethyl styrene.

The calculation results from Equation 5 using the integrated values from ^{1}H NMR validated that the feed ratio and resulting monomer ratio in the polymer were very close in composition. Compositional data corresponding to the polymerizations mentioned in Table 8 are shown below in Table 9. These data supported that starting monomer blend ratios accurately represent the monomer ratio of incorporation into the final polymer.

Table 9

Compositional Data For Styrene-Chloromethyl Styrene Copolymers Initiated By AIBN

	% CMS in Formulation (feed ratio)	% CMS in Final Polymer(^{1}H NMR integration using equation 5)
AIBN no TEMPO	3.45	3.7
AIBN with TEMPO	3.33	3.4

Following the above polymerization protocol using AIBN, the same systems were initiated using 4,4'-azobis(4-cyanovaleric acid) (ACVA) in the presence and absence of TEMPO (Table 10). It was seen that TEMPO improved control over molecular weight and minimized polydispersity compared to the control. However, the ACVA initiated system did not result in the same level of predictive control as noted with AIBN initiated systems. Figures 68 and 69 show GPC traces of TEMPO mediated and non-mediated systems, respectively.

Table 10

Styrene/Chloromethyl Styrene Formulations And Molecular Weight Results From 4,4'-Azobis(4-Cyanovaleric acid) Initiation.

	Target MW (gm/mole)	% CMS in formulation	Actual M_n (gm/mole)	PDI
ACVA no TEMPO	18,120	4.4	24,500	3.61
ACVA with TEMPO	23,535	3.4	27,860	1.6

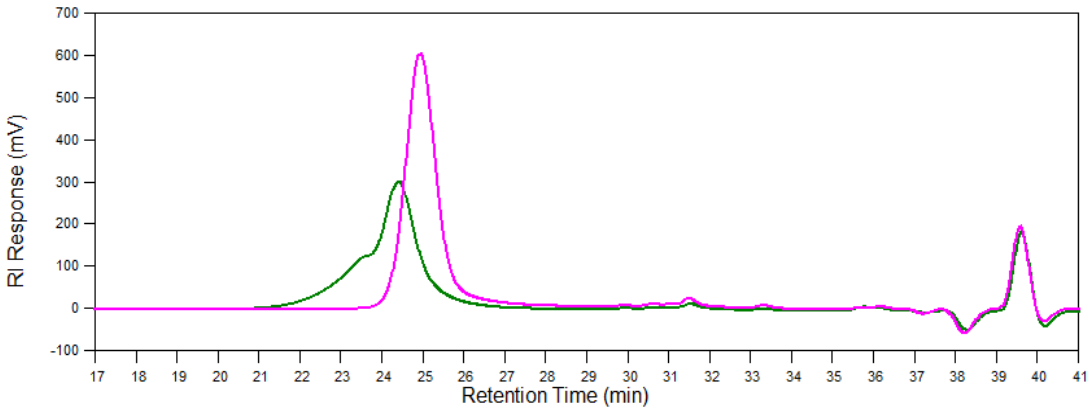

Figure 68. TEMPO mediated systems initiated by AIBN (pink trace) and ACVA (green trace).

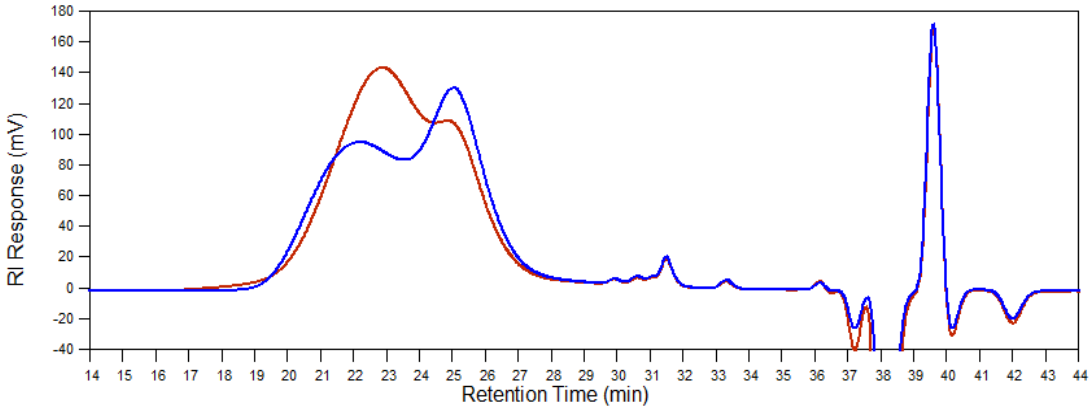

Figure 69. AIBN (blue trace) and ACVA (red trace) initiated systems in the absence of TEMPO.

The shapes of the GPC traces coupled with experimental observations give significant insight into the polymerization process (Figures 68 and 69). Figure 68 supports the relatively low PDI resulting from TEMPO mediated polymerization. However, the ACVA initiated system yields a higher PDI along with a small high molecular weight shoulder not seen in AIBN initiated systems. The GPC peak shoulder is attributed to the early initiation of polymer chains allowed from the more thermally sensitive solubilization of ACVA by the monomer solution. In bulk polymerization conditions, the ACVA does not

solubilize completely until the solution reaches polymerization temperatures; however, the portions that are soluble have been shown to initiate earlier in a given reaction. While these chains initiate earlier, they will propagate at the same rate as the chains initiated later during the polymerization, and thus produce a relatively low PDI (albeit higher than AIBN). Similar observations can be seen in Figure 69, in the absence of TEMPO, polymer chains that are initiated first grow to higher molecular weights before termination. The results were exaggerated in the ACVA initiated system, resulting in a higher percentage of the larger molecular weight peak. Both initiator types demonstrate bimodal molecular weight; however, the system with AIBN contains the higher molecular weight peak in the minority while the system with ACVA reveals that the higher molecular weight peak is in the majority. Examples using AIBN supported that all chains initiate more closely together at the beginning of the polymerization. In AIBN systems chain coupling was more prevalent and resulted higher molecular weight species revealed from the GPC trace.

The ACVA initiated systems were also characterized via percent CMS incorporated versus the feed ratio. Table 11 reveals very little change in the feed composition versus the percent incorporation in ACVA initiated polymers. In combination with percent incorporation from the AIBN systems, it was consistently shown that TEMPO initiated polymers result in a higher compositional consistency regarding CMS content in the final polymer. The slightly higher, yet detectable, CMS percentage incorporated into the polymers without TEMPO was attributed to two possible sources:

1) Side reactions of the chloromethyl group that would result in slight branching of the polymer system (Scheme 6)[4]
2) Higher reactivity rates of CMS than styrene[5]

While Scheme 6 attempts to explain the lower proportions of CMS in TEMPO mediated systems, we attributed the cause to the smaller portion of CMS groups consumed during polymerization. We also believe that the higher CMS reactivity rate in non-mediated systems was significant and should not be overlooked. All four sets of experimental conditions intentionally fell short of 100% conversion and these revealed the differential rate between CMS and styrene as potential sources for higher percentage of the more reactive monomer to be in the final polymer.

Table 11

Compositional Data For Styrene-CMS Copolymers Initiated By ACVA

	% CMS in Formulation	**% CMS in Final Polymer**
ACVA no TEMPO	4.4	4.90
ACVA with TEMPO	3.4	3.37

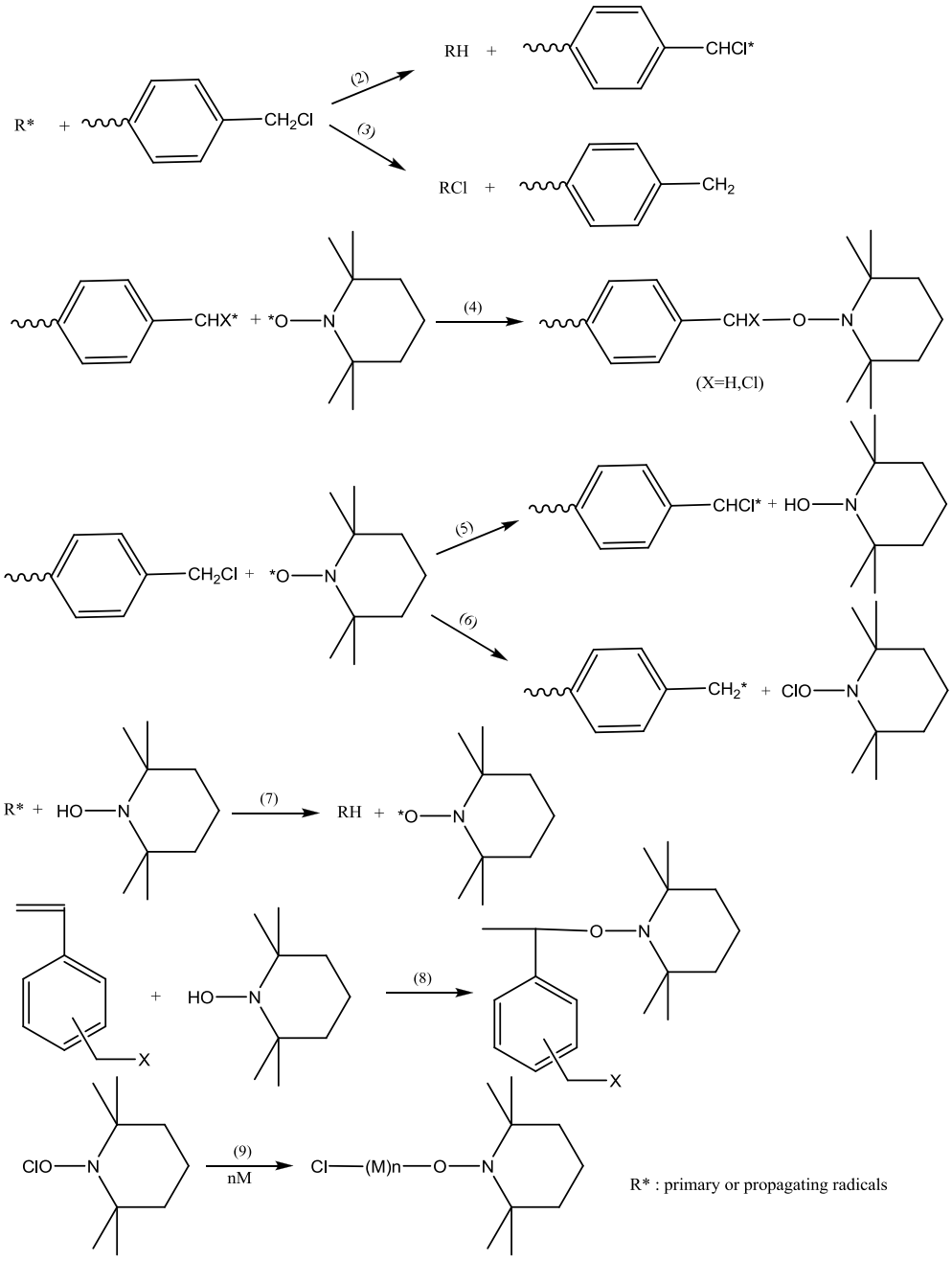

Scheme 6. Side Reaction Mechanism For TEMPO Mediated Polymerization Of CMS.

End group analysis

PS:CMS copolymers were characterized by end group quantification via ^{1}H NMR peak integration through determination of the area ratios of the acid proton (11.5 ppm) and the area related to benzylic main chain protons (1.9 ppm).

Combining the integrated area ratio with the molecular weight data generated another important ratio, i.e., the percent end functionalization versus percent non-functional chains (thermally initiated chains or chains initiated by non-functional initiator). Table 12 summarizes the percent acid group functionalization by ^{1}H NMR for the two ACVA initiated systems and the AIBN initiated system as a negative control. Lower percent end functionalization for TEMPO mediation and ACVA initiated polymers were attributed to side chain reactions (Scheme 6) that are known to increase the quantity of non-functional chains.

Table 12

Percent End Group Functionalization Based On Number Average Molecular Weight And NMR Integrations For ACVA Initiated Systems And AIBN Negative Control

	DP from M_n (GPC)	**Ratio of Acid to Benzylic Proton Area**	**Actual % Acid End Group**
ACVA no TEMPO	230.3	244.5	94.2
ACVA with TEMPO	264.2	286.8	92.1
AIBN with TEMPO	293.7	-	-

Macroinitiator chain growth

As previously mentioned in Chapter V, Quenching Reactions, the ability to create macroinitiators via Heck coupling reactions was not as versatile as desired. The most successful of these reactions resulted in less than 1% functionalization and were therefore considered inadequate for our desired outcome. While these initial attempts to create a highly functional macroinitiator were unsuccessful, it is theorized that additional work in the areas of increasing

precursor purity and end group conservation could increase the likelihood of sequential block addition. Figure 70 illustrates GPC traces for one of the many attempts at sequential block growth, and it is clear there is no shift in the peak location or shape of the initial P3HT block (figure offset due to overlay of traces).

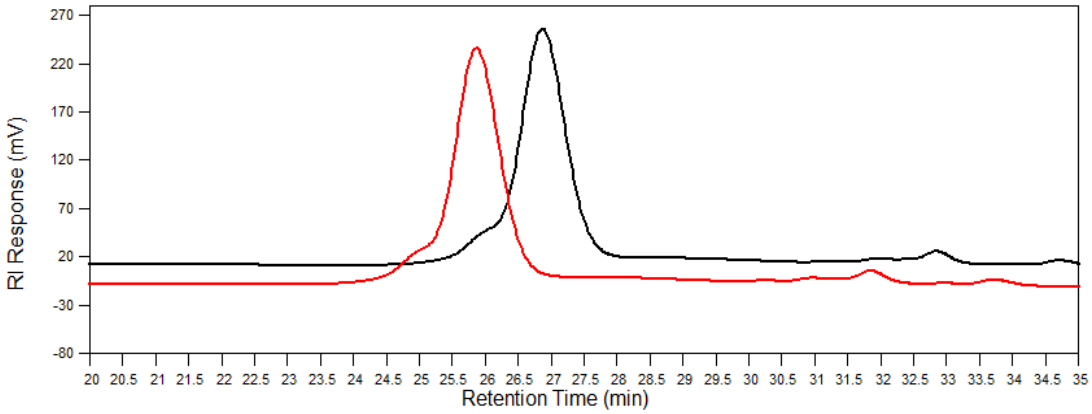

Figure 70. GPC RI traces for P3HT macroinitiator before and after attempts of sequential block addition.

Summary

The data presented in this chapter summarizes the successful polymerization of styrene – CMS copolymers at varying molecular weights and percent CMS incorporation. The polymers are functionalized with acid end groups that was used later for coupling with a hydroxyl functional P3HT. The resulting statistical copolymer(s) will be reacted through ATRA reactions with Buckminster Fullerene to create acceptor polymers for photovoltaic use in the next chapter. Attempts to functionalize and grow blocks sequentially were unsuccessful. Options to optimize these synthetic methods will be discussed in Chapter IX, Conclusions and Recommendations for Future Works.

REFERENCES

1. Moad, G.; Rizzardo, E.; Solomon, D. H. *Macromolecules.***1982,** 15, 909-914.
2. Moad, G.; Rizzardo, E. *Macromolecules.* **1995,** 28, 8722-8728.
3. Benoit, D.; Chaplinski, C.; Braslaue, R.; Hawker, C. *Journal of the American Chemical Society.* **1999,** 121, 3904-3920.
4. Katsumi, D.; Kazmaier, P.; Feorges, M.; Hamer, G.; Veregin, R. *Polymer Preprints (American Chemical Society, Division of Polymer Chemistry).* **1997,** 30(8), 2228-2231.
5. Qui, J.; Matyjaszewski, K. *Marcromolecules.***1997,** 30(19), 5643-5648.
6. Colombani, D. *Progress in Polymer Science.* **1997,** 22(8), 1649-1720.
7. Kazmaier, P. ; Daimon, K. ; Michael, G. K. ; Hamer, G. K. Veregin, R. *Macromolecules.* **1997,** 30, 2228-2231.
8. Lacroix-Dezmazes, P. ; Delair, T. ; Pichot, Ch. Boutevin, B. *Journal of Polymer Science: Part A Polymer Chemsitry.* **2000,** 38, 3845-3854.
9. Zolotova, N. V.; Kharitonov, V. V. Physical Organic Chemistry, **1988,** 8, 1904-1906.

CHAPTER VII

ATOM TRANSFER RADICAL ADDITION OF BUCKMINSTER FULLERENE AND FINAL BLOCK COPOLYMER SYNTHESIS

Introduction

The prior chapter focused on and discussed in detail the synthesis of a statistical copolymer of styrene and CMS. These copolymers were the precursors for the acceptor block coupling reactions to finalize an acceptor:donor block copolymer target. The final synthesis step for the acceptor block modification was the addition of Buckminster Fullerene to the pendant chloromethyl groups. This step was designed and expected to provide the polymer electronic and volumetric specific capabilities while matching the appropriate band gap levels for efficient transfer of excitons generated in the P3HT segment to the electrode. This chapter was organized to validate our hypothesis that atom transfer radical polymerization (ATRP) mechanisms are active via pendant side chains for fullerene addition. Furthermore, this chapter provides supporting physical and analytical evidence of fullerene addition to the previously synthesized copolymer and a summary of the final synthetic steps for coupling hydroxyl functional P3HT with the acid functional styrene:CMS/Fullerene.

Toward our end goal of an all-in-one acceptor:donor block copolymer, each synthetic step presented in this chapter required us to overcome certain major challenges to obtain the desired outcome. One of the most critical synthetic steps to produce materials with utility for our overarching goal is the

synthesis of a fullerene functional polymer while limiting the result(s) to a controlled number of fullerene additions. Multiple attachment points to a single fullerene would result in insoluble products, i.e., fullerene acting as a crosslinker. A variety of experimental conditions were evaluated with multiple chloromethyl to fullerene stoichiometric ratios and reaction conditions in order to examine this hurdle. The convergent last step, for block-to-block copolymer synthesis, utilized end group esterification reactions. To achieve high yields, catalysis and Le Chatelier's principle were employed in combination. The resulting coupling ratio was examined by GPC trace integration.

Atom Transfer Radical Polymerization/Addition Proof of Concept

Conceptually, ATRP is very similar to NMP. As with NMP, the control afforded by ATRP comes from the decrease in active radical species through the reversible reaction with a mediating species. NMP methods use a stable free radical species. However, in the case of ATRP radical generation, the mediating species is typically a metal centered complex with halogenated species where the reaction control is offered by a reversible redox process. The catalyst species is one of the most important components of the ATRP process as it controls the overall rate of reaction, specifically the concentration of active radical species. The metal catalysts were required to meet several considerations in order to be active for ATRP mechanisms. First and foremost, the ATRP catalyst is required to possess two oxidation states that are readily accessed by the transfer of only a single electron. The catalyst must also have an affinity towards halogens and the coordination sphere must be able to accommodate the added halogen species.

Finally, it is necessary that the catalyst exhibit a strong complexation with the solvating ligand.[1]

The main advantage of ATRP includes tolerance to other functional groups present during synthesis.[2] This broad tolerance supports ATRP as the logical choice for the research described in this chapter, i.e., the addition of fullerene to an acid functional styrene:CMS copolymer. Architectural control and its amenability toward molecular design are the significant advantages of controlled free radical polymerization.[3] Many cases that use multiple combinations of controlled free radical techniques have been reported,[4, 5, 6] including ATRP in combination with NMP.[7, 8, 9] However, fewer examples have been reported of ATRP being used as an addition mechanism. This chapter specifically focuses on fullerene addition to the main chain. While this mechanism follows ATRP principles, it is fundamentally different due to the steric nature after the first fullerene addition. It is this steric hindrance to additional reactions and propagation that makes Atom Transfer Radical Addition (ATRA) amenable for grafting fullerene to styrene:CMS copolymers.

The first characterization step was to quantify the number of ATRP active sites. To do this, the styrene:CMS polymer (initiated by ACVA and polymerized using NMP mechanisms with TEMPO as the mediating agent) was modified via ATRP on the CMS moiety to result in branched polystyrene. The use of styrene as a model, in place of Buckminster Fullerene, allowed for exaggeration of the molecular weight change, which was intended to prove that the initiation species was, in fact, the previously synthesized polymer chain.

Example reaction conditions are summarized in Chapter II. In this particular example, toluene was utilized as the solvent. The polymer was precipitated into methanol and dried in a vacuum oven at room temperature for 48 hours before analysis via NMR and GPC to confirm the active nature of ATRP mechanism(s). We did expect the chloromethyl group protons that initiated polymerization to exhibit significant change in electronic character and result in an up field shift, thereby blending with the main chain methylene units at the same ppm. The GPC results were expected to show a complete shift of molecular weight, confirming that initiation species was the initial polymer. Figure 71 illustrates the ^{1}H NMR results for this reaction, and an enlarged focus on the peak 4.6 ppm region before and after synthesis, demonstrates the loss of chloromethyl groups. Figure 72 illustrates the GPC traces of both the precursor and branched polymer. In this figure, the absence of the original peak (completely shifted) supports effective initiation derived from chloromethyl units.

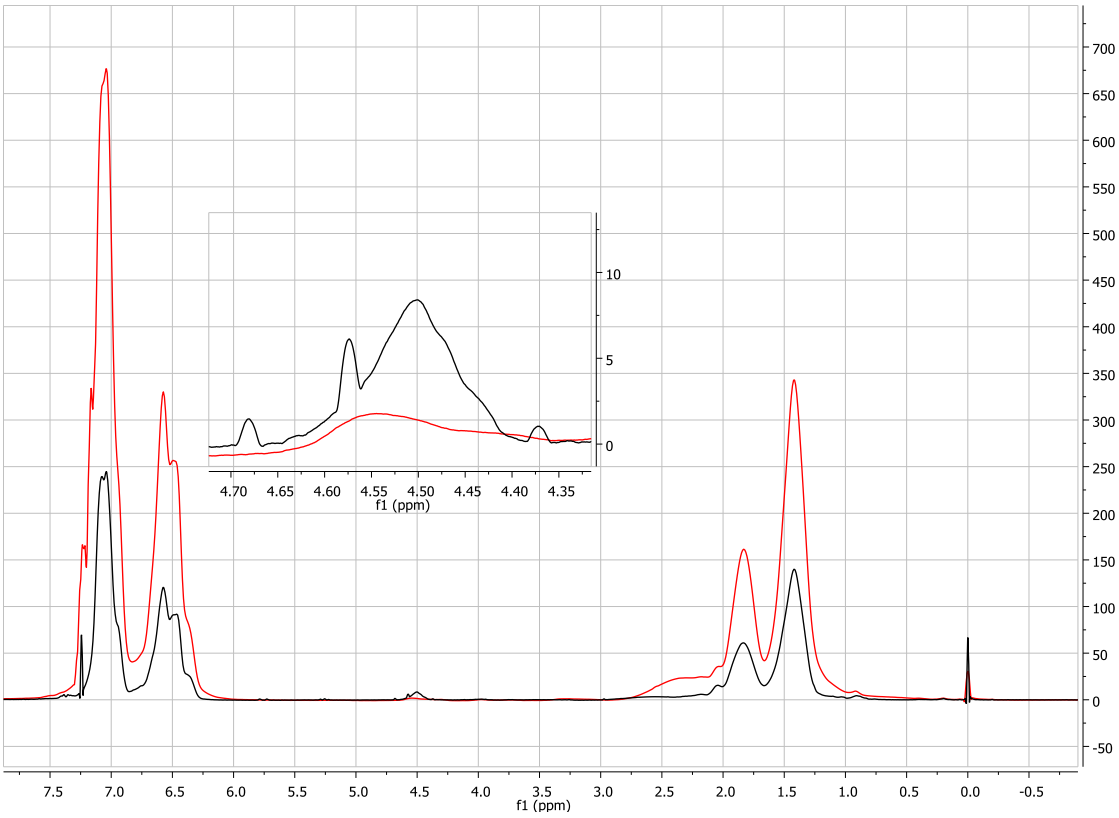

Figure 71. ^{1}H NMR of a) styrene:CMS polymer (black trace) and b) ATRP initiated branched polystyrene (red trace).

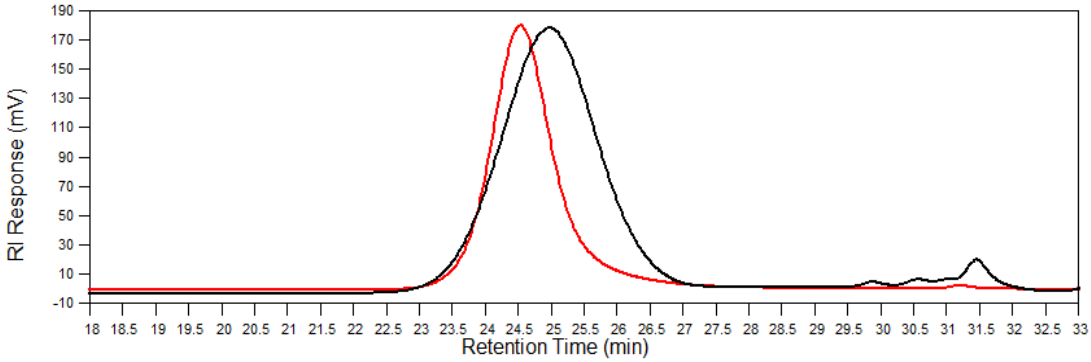

Figure 72. GPC of a) styrene:CMS polymer (black trace) and b) ATRP initiated branched polystyrene (red trace) illustrating effective initiation from chloromethyl group.

Figures 71 and 72 do not singularly demonstrate the effectiveness of the ATRP mechanism as applied to the chloromethyl side chains; however, the

combined data support results from which all chains have at least one active site and that particular site polymerizes an additional chain. The loss of the 4.6 ppm peak, relative to all other peaks, in the NMR supports a dilution of chloromethyl groups. When considering the creation of new polystyrene chains, the data must be used in combination with GPC to confirm that the results were not simply driven by a mixing dilution versus time from thermally initiated polystyrene. Confirmation is clear upon viewing the loss of the original polymer/macroinitiator peak in GPC and the shifted higher molecular weight peaks.

Acid-PS:CMS:Fu

We considered the results in Section 7.2 as successful proof for the concept of active ATRP initiation sites. Several routes were pursued to covalently attach Buckminster Fullerene with polystyrene chains. While the experimental conditions were very similar to those performed with the branching experiments, a few distinguishable and necessary adjustments were made throughout the process as outlined below.

Initial attempts at fullerene addition utilized toluene as the reaction solvent. Precipitate was detected near the reaction end; moreover, the reaction precipitate grew rapidly to become most of the expected yield and these products were intractable. From our results, it is our theory that the extremely poor Buckminster Fullerene solubility (3 g/L) in toluene forced an instantaneous stoichiometric deficiency of fullerene units. The deficiency resulted in a diminished number of available fullerenes for participation, and thereby facilitated multiple additions by the chloromethyl units to each fullerene, effectively

crosslinking through the fullerene. The result leads to two logically possible corrections; further dilution of the reaction and selection of an improved solvent for fullerene.

To produce fullerene functional polymer side chains and maintain resulting polymer solubility, only single fullerene addition is desired. Dilution was improved by doubling the solvent ratio to result in equal amounts of soluble fullerene and chloromethyl groups. Further dilution also altered the reaction kinetics and increased the reaction time drastically. The 2x diluted reaction and the dilution driven slower reaction rates resulted in another intractable product. Fullerene contains a large number of available reaction sites and complicated achieving our reaction goals.

Solvent change was the next logical option. The solvent selection was driven by three characteristics: 1) a desire for increased fullerene and polymer solubility, 2) facile post-product solvent removal, and 3) to ensure that ATRP mechanism activity was not disrupted by another set of side reactions/products. With these criteria in mind, 1,2-dichlorobenzene was selected as the solvent. Results proved that 1,2-dichlorobenzene was capable of maintaining eight times the concentration of soluble fullerene (24 g/L) and several literature reports provided the precedent for non-invasive ATRP reactions.[10, 11, 12] The combined experimental conditions allowed for five times the molar excess of fullerene to chloromethyl groups. The resulting mixture was deep purple due to the large excess of fullerene and yielded a brown soluble polymer fraction. In addition to the traditional precipitation procedure, the resulting products were washed to

remove the excess fullerene. The polymer and fullerene mixture were filtered from methanol and dried in the filter. The precipitate was washed with THF, since the THF would solubilize the polymer and any covalently attached fullerene. Very little of the unattached fullerene would pass through the filter (0.006 g/L solubility in THF). The soluble polymer fraction was analyzed via NMR and GPC to validate fullerene addition to the polymer. Figure 73 illustrates the ^{1}HNMR of a representative final product, as well as, the precursor styrene:CMS copolymer. The important peaks were diminished at 4.6 ppm corresponding to the chloromethyl group and the appearance of peaks at 3.1 and 3.4 ppm correlated with the same protons after fullerene addition.

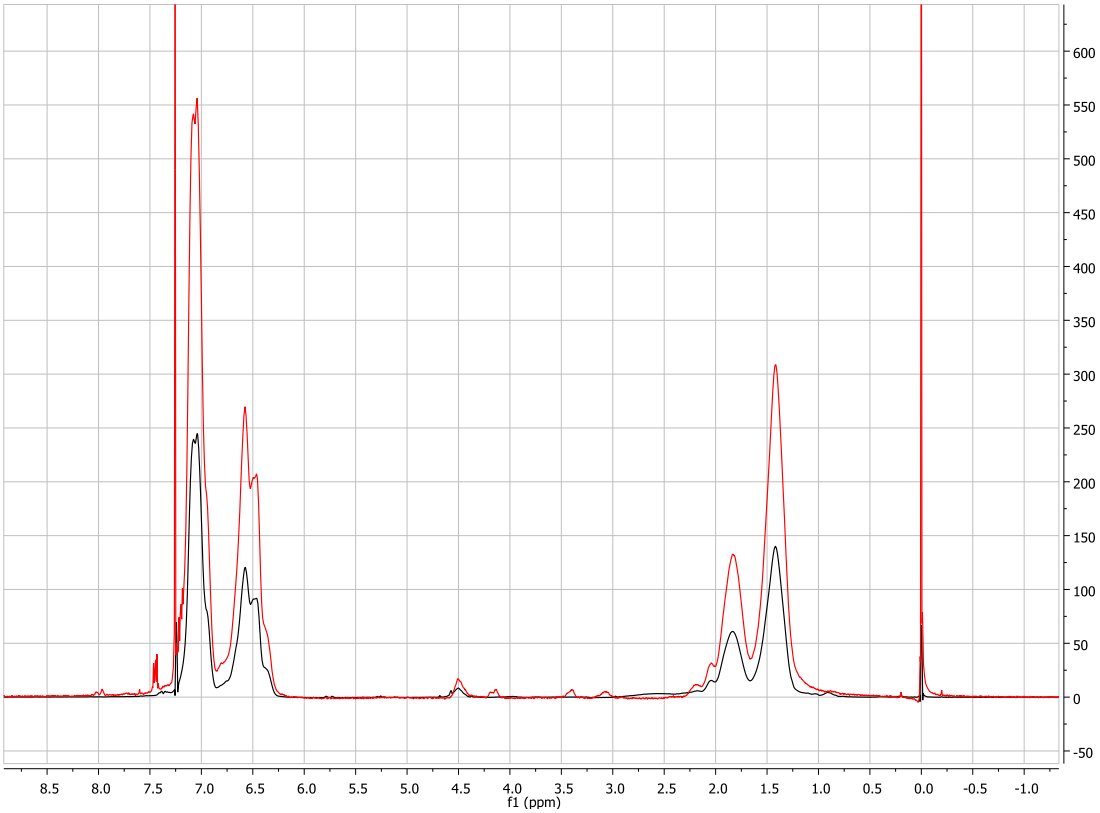

Figure 73. ^{1}H NMR of a) styrene:CMS (black trace) and b) styrene:CMS/Fullerene (red trace).

The GPC chromatogram in Figure 74 exhibits traces for both the styrene:CMS prepolymer, as well as, the fullerene functionalized copolymer. The results validate that there is a slight shift in molecular weight (~1,600 g/mole) that corresponds with the addition of two to three fullerene units per polymer chain. Notably, the peaks representing free fullerene detected in solution at 30.2 minutes or molecular weight 720 g/mole were absent (albeit trace impurities were still possible).

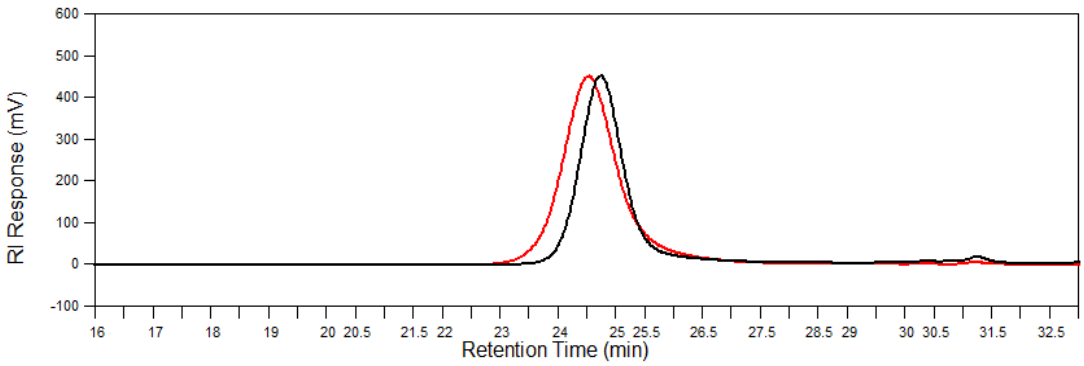

Figure 74. GPC of a) styrene:CMS polymer (black trace) and b) fullerene containing polystyrene (red trace) illustrating effective initiation from chloromethyl group.

GPC and NMR in combination again confirm the presence of the desired reaction. Albeit qualified, these data do not singularly quantify the resulting composition. The GPC data does provide a rough estimate of two to three units per chain; however, for material use, it is critical to define the polymer-tethered fullerene weight percent as an acceptor-block in organic photovoltaics. As used commonly in the fullerene and carbon nanotube literature, tethered fullerene was thermally degraded in the presence of oxygen using TGA.

Thermal properties and confirmation of addition

The quantity of polymer-tethered Buckminster Fullerene and the materials' thermal properties were measured via TGA. Baseline examination of pristine Buckminster Fullerene, a functionalized fullerene, Phenyl-C61-Butyric acid Methyl ester (PCBM) and the polystyrene precursor were conducted on DSC and TGA as control samples. Figures 75, 76 and 77 show the DSC thermograms for pure Buckminster Fullerene, PCBM, and an example polystyrene precursor, respectively.

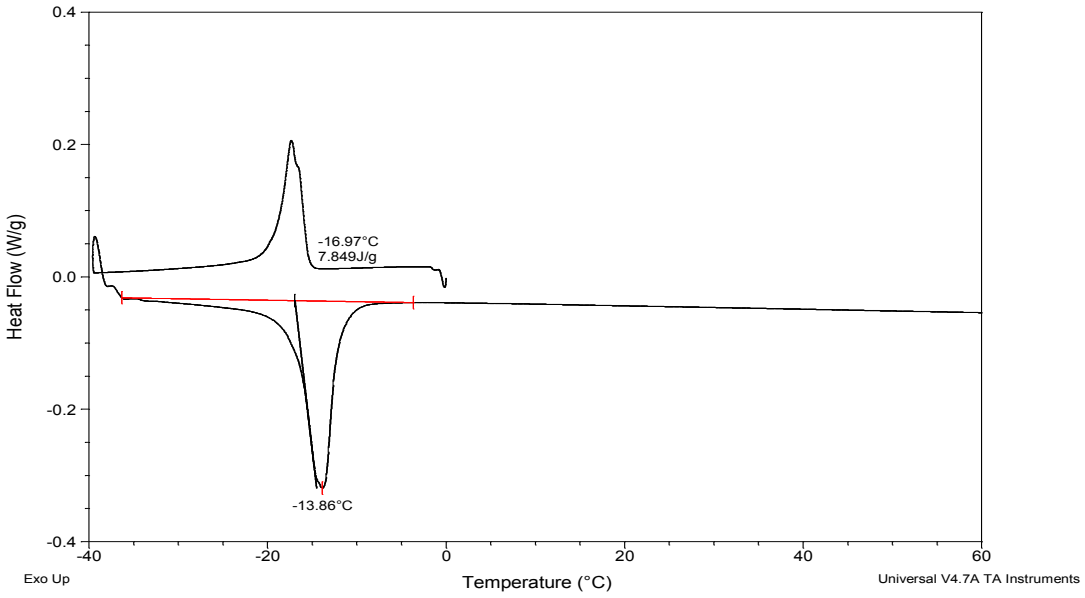

Figure 75. DSC curve of Buckminster Fullerene.

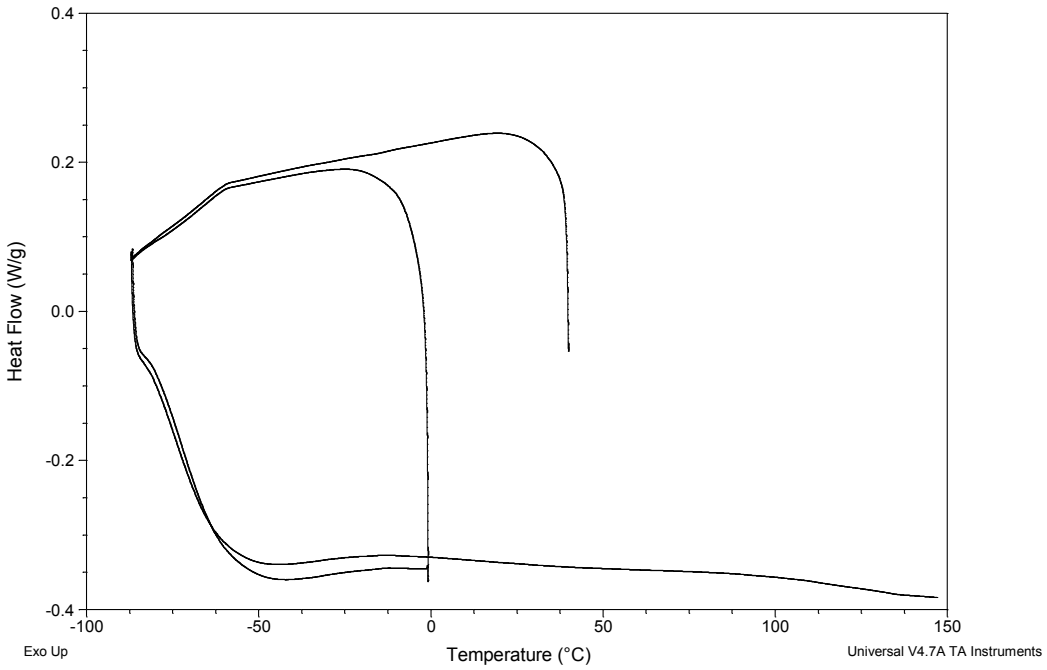

Figure 76. DSC curve of phenyl-C61-butyric acid methyl ester.

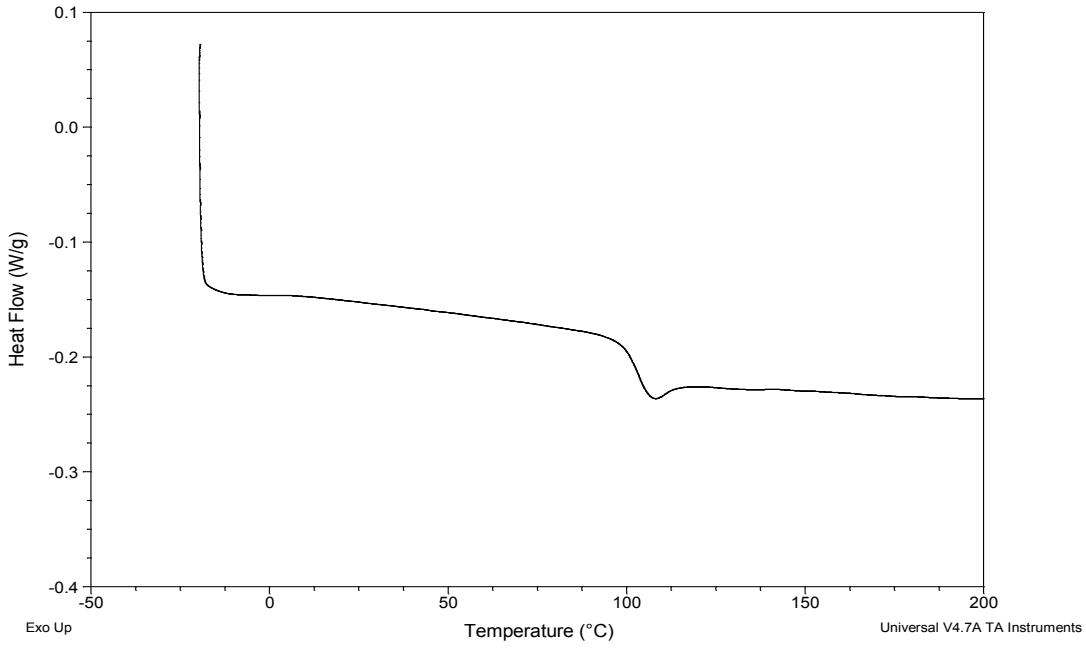

Figure 77. Example DSC curve of a polystyrene-stat-chloromethyl styrene copolymer.

The DSC curves above reveal a low temperature transition at approximately -14ºC for Buckminster Fullerene, and the transition has been

attributed to orientational-ordering.[13, 14] The ordering has been attributed directly to a crystal-to-plastic crystal enthalpy transition of 6.99 kJ/mol or 9.7 J/g according to literature values;[13] however, our results find an enthalpy transition of 7.85 J/g or 5.65 kJ/mol. It is important to note that the same transition is absent in PCBM. The results support an absence of the transition for polymer-tethered fullerene. The thermogram absence from this distinct transition singularly eliminates DSC as a direct method to calculate the tethered fullerene percent incorporation. The thermal transition allows untethered fullerene units to be quantified (free and/or aggregated fullerene). Figure 77 shows the typical T_g transition of approximately 100ºC for polystyrene and is absent any other transitions. The DSC curve for a polymer crosslinked via fullerene units is shown in Figure 78. In this example, tethered and untethered fullerene has become trapped in the intractable polymer. Evidence supporting this conclusion is derived from the absence of the polystyrene T_g transition; however, the sample results clarify a crystal-to-plastic transition from untethered fullerene. Figure 79 is DSC data for a washed polymer-tethered fullerene in the absence of crosslinks. The results exhibit thermal transitions relating to polystyrene and are absent from the ordering transition of fullerene. The combination, or lack, of each transition confirms the ability to remove any residual untethered fullerene, as well as, the absence of crosslinking in this example. Again further analysis is needed to quantify the fullerene content.

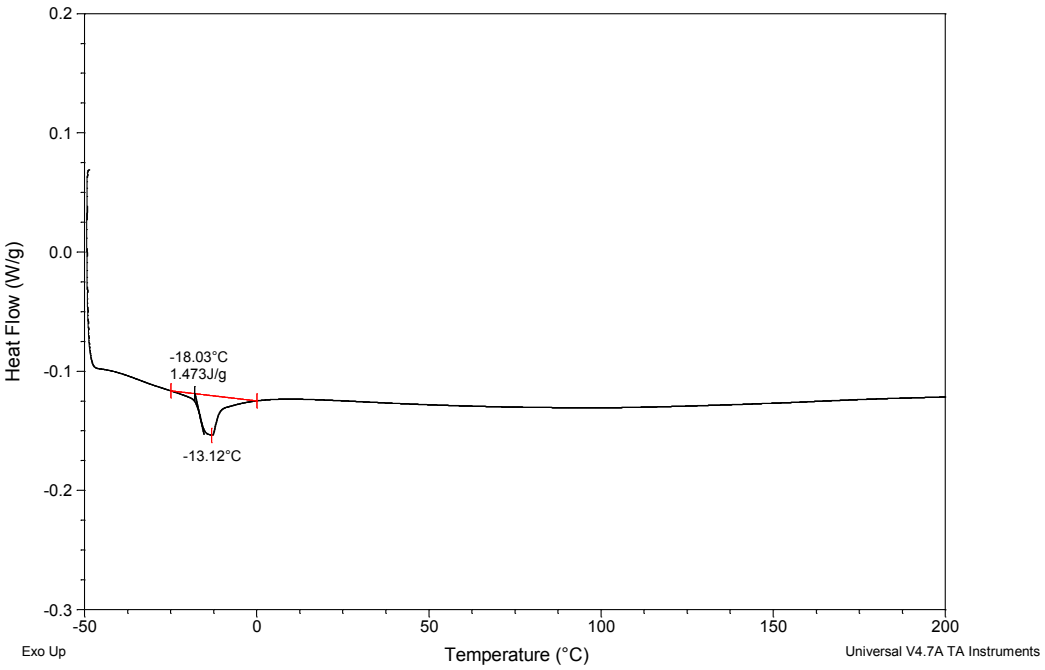

Figure 78. DSC of intractable crosslinked PS-stat-CMS/Fu showing presence of non-grafted fullerene.

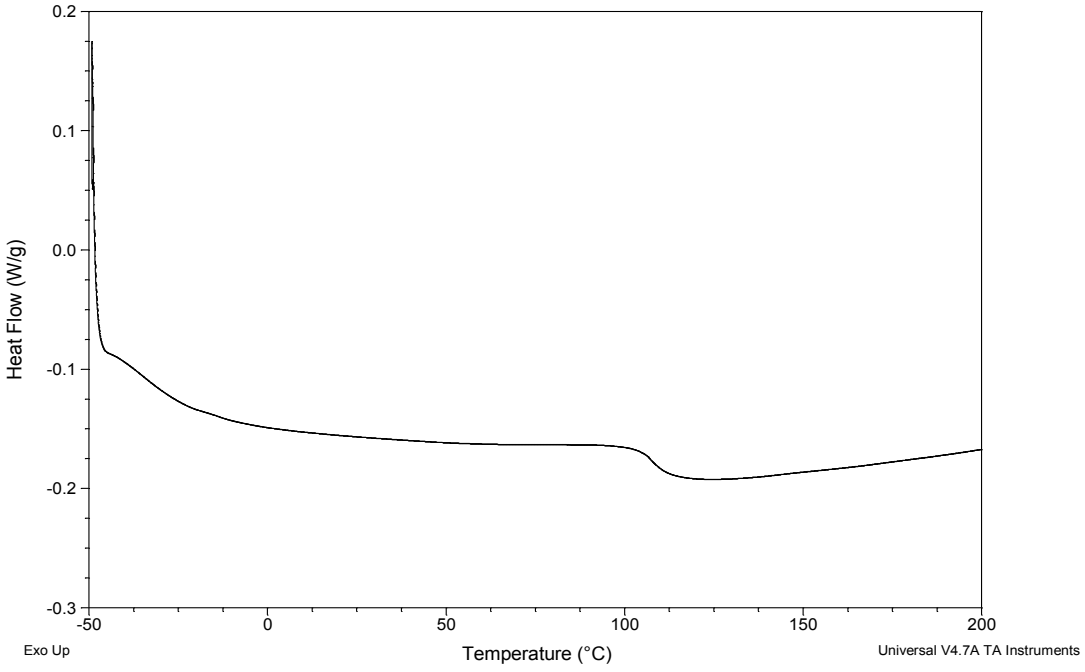

Figure 79. DSC of a completed acceptor segment (PS-stat-CMS/Fu).

Following DSC characterization for thermal transitions, TGA was used to quantify the percent fullerene incorporation. Thermal degradation of fullerene, fullerene derivatives, and the free standing acceptor block were performed in an air atmosphere to prove the methods and as a direct measure of fullerene content. The experiments started by establishing each material's thermal stability and the percent fullerene incorporation for two copolymers of polystyrene and a polymer tethered-fullerene. The polymers were synthesized at varying targeted levels of fullerene addition. Figure 80 summarizes the TGA analysis of pure Buckminster Fullerene, Phenyl-C61 butyric acid methyl ester (PCBM) and the previously mentioned polystyrene samples functionalized with fullerene at different levels of additions, as well as, pre-fullerene addition. As expected, the data reveal that pure Buckminster Fullerene (black trace) maintains the highest thermal stability and weight retention of material.[14] The remaining samples degraded at varying temperatures based on the number of substitutions to the fullerene structure. The samples containing polystyrene have an initial degradation point related to the styrene portion as seen in the styrene trace (black dotted trace); however, the second degradation is directly attributed to fullerene incorporation. The styrene:CMS/fullerene copolymer with one addition (two substitutions) to each fullerene (green trace) exhibited the second highest degradation temperature. This degradation was expected to be comparable to PCBM, which has two substitutions. PCBM has the added ring strain of a three-membered ring, which would account for the decreased fullerene stability in contrast to the previously supported literature data. Finally, the crosslinked

fullerene sample possessed the lowest thermal stability and yet was also intractable in all the solvents tested (1,2-dichlorobenzene did manage to extract small portions of unreacted Buckminster Fullerene).

Two main conclusions were drawn from these data: 1) fullerene thermal stability generally decreases in direct correlation with the number of substitutions or loss of conjugation compared with virgin fullerene and 2) TGA characterization provides an accurate methodology to quantify fullerene content and track the synthesis results for future homopolymers and block copolymers.

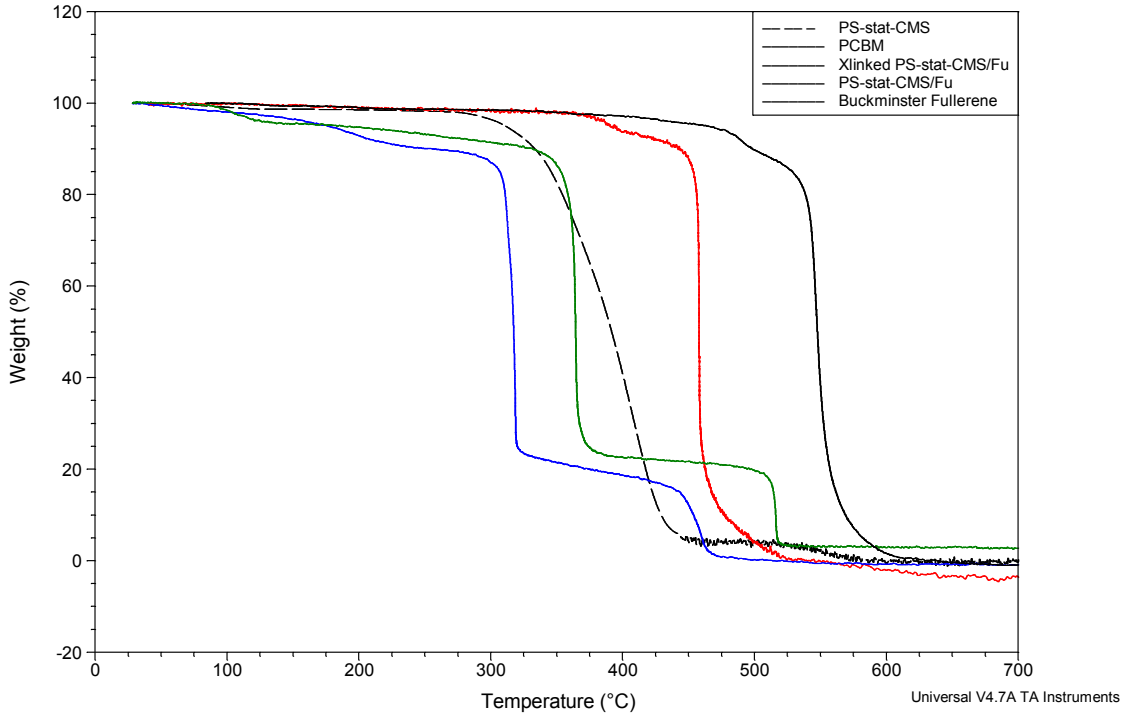

Figure 80. TGA of Buckminster Fullerene (black trace) and its derivatives, PCBM (red trace), crosslinked fullerene functional polystyrene (blue trace) and a functional polystyrene with pendant fullerene (green trace).

Synthesis of P3HT:PS:CMS:Fu

For our purposes, the final synthesis step to complete an acceptor:donor block copolymer was to couple the two active blocks via esterification reaction.

Important characteristics that were considered for the resulting polymers include: molecular weight for each block (this important parameter is directly related later to the block volume ratios), percent tethered-fullerene and coupling efficiency to avoid excessive homopolymer presence. The three characteristics are important for a variety of reasons; the most pressing are those affecting the resulting thin film morphology. Specifically, the focus of this work compared the effects of molecular weight changes on P3HT segment weight fraction versus polymer tethered fullerene content, allowing variables to be isolated and the effects of each ratio on thin film morphology studied.

Esterification Coupling Reaction

End functionalized polymers, a series of hydroxyl functional P3HT and an acid functional PS-stat-CMS/Fu polymer, were combined in varying ratios to measure coupling efficiency via esterification. GPC measured the efficiency of coupling. The final copolymer traces were compared with the respective starting homopolymers segments. Using these controls allowed the area of residual homopolymers to be integrated and ultimately resulted in a calculated percent coupling.

The first coupling reactions were attempted in refluxing toluene, without a catalyst and equipped with a Dean-Stark trap for water removal. NMR and GPC results were used to calculate acceptor and donor block starting point stoichiometric ratios. Each of the resulting polymers were precipitated into methanol, filtered and dried. An example GPC trace (Figure 81) confirmed that these conditions yielded only trace quantities of polymer-to-polymer coupling.

The chromatograms confirm that the final polymer trace exhibits a broadening effect (the red trace in Figure 81) due to the mixing of the two reactions. Minimal coupling occurred under these conditions and result in little, if any, high molecular weight block copolymer. An important point of reference, for later experiments, is also shown in Figure 81, i.e., approximately equal volume concentrations of each polymer block were added to the reaction mixture. However, the higher $d\eta/dc$ value for P3HT results in higher RI response than the polystyrene based segments.

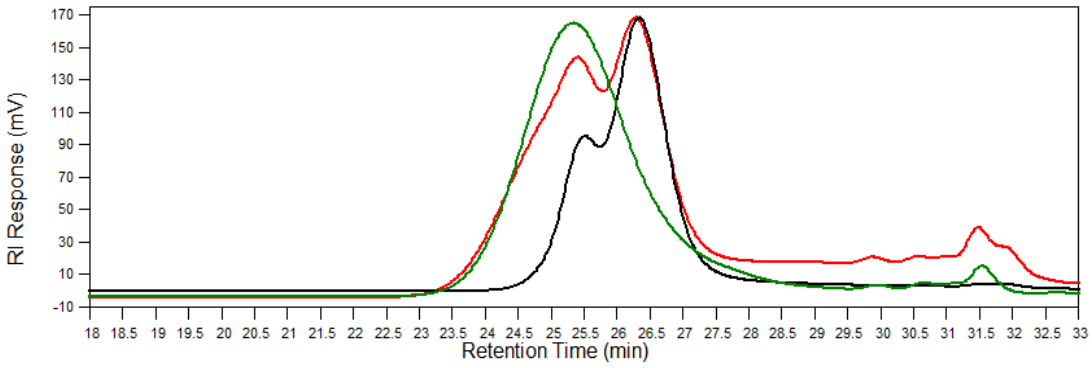

Figure 81. Coupling reaction of 10,000 g/mole P3HT-OH (black trace) and 15,000 gm/mol PS-stat-CMS/Fu (green trace) in the absence of catalyst, with the red trace being the final product.

Next, a reaction was used to test efficient polymer coupling reactions which included the use of dibutyl tin dilaurate as an esterification catalyst. The reactions were started with 0.1 wt% dibutyl tin dilaurate (DBTL) to evaluate homopolymer coupling conversion. Figure 82 summarizes an example of the DBTL catalyzed reactions using the same starting polymers as used from the reaction results summarized in Figure 81. The catalysts clearly improved coupling efficiency; however, only partially coupled products resulted. Calculations were performed assuming a 100% mass recovery (no gel and all

soluble products) and using the dη/dc values as calculated from each homopolymer, all based upon integrated peak areas. The DBTL catalyzed reaction polymer resulted in approximately 85% coupled product.

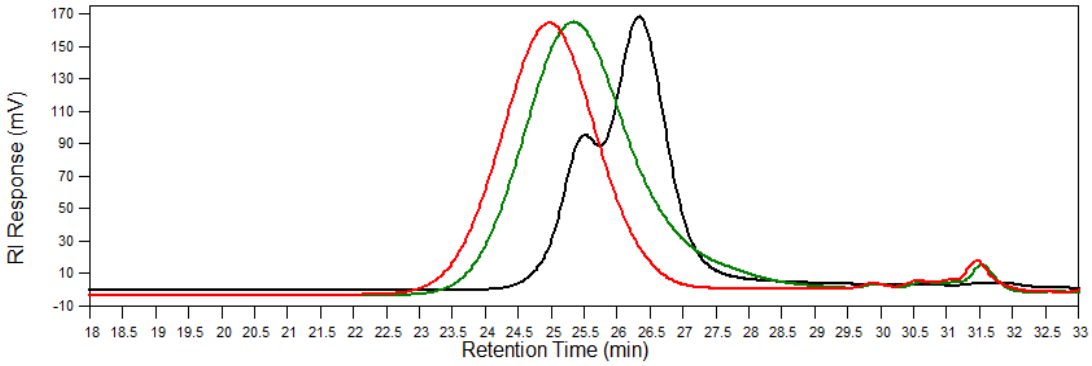

Figure 82. Coupling reaction of 10,000 g/mole P3HT-OH (black trace) and 15,000 g/mol PS-stat-CMS/Fu (green trace) in the presence of dibutyl tin dilaurate catalyst, with the red trace being the final product.

It is critical for us to connect our synthetic results with the end goal of morphology studies. According to several morphology studies in the literature, a degree of coupling in the range of 85% was considered sufficient for acceptor donor blocks to dominate the thin film morphology control mechanisms (stated as 74% volume blocking efficiency).[15] In the cited research, it was shown that the addition of homopolymers to 100% diblock copolymers shifted the resulting morphology on a desired/needed basis for targeting a particular volume fraction ratio. Using these literature data, our synthesis products and varying blends could be used at varying ratios to generate a series of morphologies for study. Their results provide sufficient basis to study our morphology progression and photovoltaic efficiency studies without the necessity of 100% block coupling efficiency.

The next synthesis procedure was performed to give a baseline on the effect of morphology based on the volume fraction of the rod segment, in this case P3HT. Following the same procedure for the coupling of the block as mentioned above, a second block copolymer was produced starting with an increased molecular weight of P3HT building block. The starting molecular weight was increased by 10,000 g/mole and has been considered large in previous studies as the high persistence length of P3HT drives more dramatic morphology changes than typically expected from amorphous blocks. The resulting GPC trace (Figure 83) resulted in 78% coupling using the same methods as described previously.

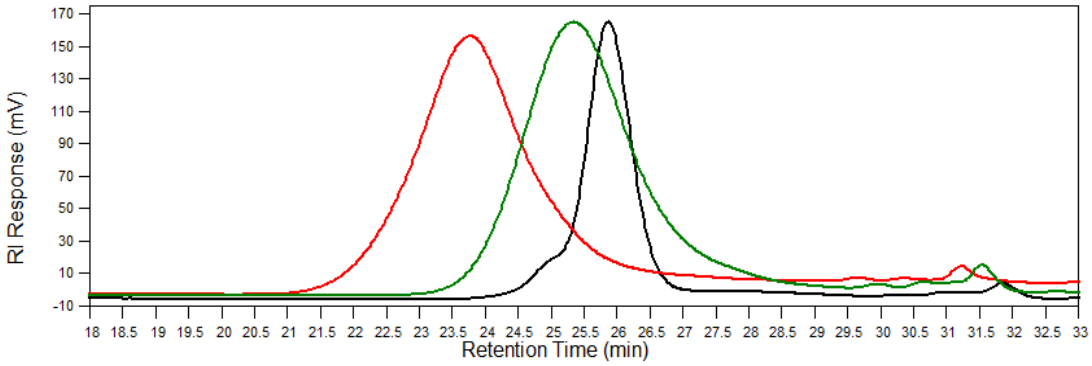

Figure 83. Coupling reaction of 20,000 gm/mole P3HT-OH (green trace) and 15,000 gm/mol PS-stat-CMS/Fu (black trace) in the presence of dibutyl tin dilaurate catalyst, with the red trace being the final product.

Discussed in the next chapter in detail, the resulting block copolymers were proven to exhibit self-quenching behavior as desired and were used to initiate our morphology studies by varying solvent type, casting method and the mode and/or duration of annealing. The same materials were used to construct our initial photovoltaic cells for photovoltaic efficiency measurements. The

diblock copolymer results for morphology and OPV efficiency results are summarized in the next chapter.

Summary

A multitude of synthetic techniques and various molecular weight targets successfully demonstrated tailorable block copolymers that possess characteristics of both donor and acceptor materials for self-organizing organic photovoltaics. The synthesis process and variables confirm the ability to control the molecular weight of each segment, as well as, the percent incorporation of fullerene. It is from this set of parameters, i.e., a molecular OPV toolbox, that a series of acceptor:donor block polymers with varying morphologies will be studied for device performance and used as an overall measurement of material efficiency. The resulting variations in material morphology will provide a systematic method to quantify rod-coil morphologies in direct correlation with photovoltaic efficiency.

REFERENCES

1. Odian, G. *Principles of Polymerization.* 4th Edition. John Wiley & Sons: Hoboken, 2004. pp. 316-325.
2. Coessenes, V.; Matyjaszewski, K. *Journal of Chemcical Education.* **2010,** 87(9), 916-919.
3. Tang, W.; He, J.; Yang, Y., Journal of Macromolecular Science, Part A: Pure and Applied Chemistry. **2006,** 43, 1553-1567.
4. Guo, Y. M.; Pan, C. Y. *Polymer.* **2001,** 42, 2863-2869.
5. Hawker, C. ; Hedrick, J.; Malmstrom, E.; Trollsas, M.; Mecerreyes, D.; Moineau, G. ; Dubois, P.; Jerome, R. *Macromolecules.* **1998,** 31(2), 213-219.
6. Angot, S.; Taton, D.; Gnanou, Y. *Macromolecules*, **2000,** 33(15), 5418-5426.
7. Murthy, K. S. ; Ma, Q. ; Clark, C. ; Remsen, E.; Wooley, K. *Chemical Communications.* **2001,** 8, 773-774.
8. Tunca, U.; Karliga, B.; Ertekin, S.; Ugur, A. L.; Sirkecioglu, O.; Hizal, G. *Polymer.* **2001,** 42(20), 8489-8493.
9. Celik, C.; Hizal, G.; Tunca, U. *Journal of Polymer Science Part A: Polymer Chemistry.* **2003,** 41(16), 2542-2548.
10. Anachenko, G.; Matyjaszewski, K**.** *Macromolecules.* **2002,** 35(22), 8323-8329.
11. Lattuada, M.; Hatton, A. *Langmuir.* **2007,** 23(4), 2158-2168.
12. Qin, S.; Qin, D.; Ford, W. T.; Resasco, D. E.; Herrera, J. E. *Journal of the American Chemical Society.* **2004,** 126(1), 170-176.
13. Jin, Y.; Cheng, J.; Varma-Nair, M.; Lian, G.; Fu, Y.; Wunderlich, B. *Journal of Physical Chemistry.* **1992,** 96(12), 5151-5156.

14. Tse, J. S.; Klug, D. D.; Wilkinson, D. A. *Chemical Physics Letters.* **1991,** 183(5), 387-390.

15. Tureau, M. S.; Rong, L.; Hsiao, B. S. ; Epps III, T. H. *Macromolecules.* **2010,** 43, 9039-9048.

CHAPTER VIII

PROPERTY ANALYSIS OF RESULTING POLYMERS

Introduction

The most important aspect of the polymers discussed in this dissertation relate to their physical properties. While the synthesis of the goal structures proved to be difficult and allowed for development of understanding in both the mechanism and experimental conditions required for these particular reactions, they were made with an overall use in mind. This end use as a photovoltaic active material requires several different specific properties, many of which are required to produce any photovoltaic response such as broad absorption properties of photons at appropriate energy levels. These requirements were addressed directly in the synthesis by known properties of homopolymers or homopolymer constituents. Other requirements including efficient transfer of electrons are dictated by other properties such as percent incorporation of conductive moieties and the self-assembly properties of the polymer. Specifically, these requirements are a function of the completed block copolymer and details to their impact on the overall properties were examined.

This final data inclusion chapter will discuss the physical properties, morphology and photovoltaic response pertinent to each domain of the block copolymer, singularly in their homopolymer form and ultimately the block copolymer. The most efficient block copolymers will effectively display the characteristics of both the homopolymers, while having the added advantage of self-assembly. This self-assembly into controlled morphologies is theorized to improve overall photovoltaic efficiency through the increased exciton

disassociation and electron transfer while reducing the ability of charge recombination. The properties of each homopolymer and block copolymer were examined by the techniques described below.

UV-Vis-Fluorescence

The defining property for materials use in photovoltaic devices is their ability to absorb photonic energy and convert this energy to electrical current. UV-Vis-Fluorescence spectroscopy measures a material's effectiveness of absorbing photonic energy and transferring this energy to varying energy bands. UV-Vis accomplishes this by the measurement of the wavelength and intensity of absorption of near-ultraviolet and visible light. Ultraviolet and visible light is energetic enough to promote outer-shell or Highest Occupied Molecular Orbital (HOMO) electrons to higher energy levels or the Lowest Unoccupied Molecular Orbital (LUMO). Absorption spectra are useful for vague identification of compounds but are commonly used for quantitative measurements; specifically the absorbance spectrum of P3HT can give information on its crystalline structure, approximate molecular weight, and regioregularity. It has been shown that bathochromic shifts are observed upon the increase of molecular weight, and peak shape or modality is affected by crystallinity and regioregularity.[1]

Fluorescence occurs after the absorption of radiation has occurred. Once this absorption has occurred, the system releases a photon of radiation as it moves back down to the HOMO within 10^{-6} seconds. During this de-excitation, there are three separate modes in which it can take: vibrational relaxation, internal emission and external conversions. In terms of photovoltaic processes, it

has been shown that the presence of fluorescence in a donor material indicates the ability to effectively transfer energy to the generation of an exciton. Once in combination with an acceptor material, the original fluorescence should no longer be present due to the quenching of fluorescence, or charge separation. The degree of quenching can be a direct indicator of interfacial contact and overall photovoltaic promise.

TGA and DSC

Thermal properties of the resulting homopolymers and block copolymers are useful in characterizing the resulting material, as well as, giving an indication of the properties that can be expected from a resulting photovoltaic cell. Specifically, DSC allows for the quantification of crystalline regimes caused by the π-π stacking and side chain crystallization of P3HT[2], and as discussed in the previous chapter will allow for the quantification of non-covalently bonded Buckminster Fullerene present in the polymer system.[3] TGA augments the understanding of the degradation processes occurring in homopolymers and quantifies the fullerene content.

Atomic Force Microscopy (AFM)

One of the driving forces for increased efficiency of photovoltaic cells is morphology control of the active materials. AFM is a well-established technique for the measurement and quantification of nanoscale morphologies. When performing this type of characterization, the AFM typically operates in non-contact mode, which is a sharp tip in an oscillating mode above the surface. The changes in oscillations are caused by local changes in the topography and are

optically recorded by a laser impinging on the back of the cantilever. The amplitude of the cantilever has proven to be very sensitive to topographical changes and mechanical properties of the material, and is suitable for delineating interfaces of photovoltaic materials. AFM is capable of both monitoring the surface roughness of the material while simultaneously measuring the phase separation of the materials. These two factors are significant to the overall final cell efficiency. Due to the ability to gain useful information from one test, AFM has turned into a standard characterization method for the routine analysis of semiconducting polymers and blends used for photovoltaic purposes. In combination with these effects, conductive AFM is becoming a more standard means of operation, offering the added bonus of measuring electrical properties while producing the same morphological and roughness information.

Results and Discussion

Absorbance and Fluorescence Quenching

Synthesized P3HT was analyzed for properties that affect the overall efficacy in final photovoltaic cells. These analyses include UV-Vis absorbance, fluorescence, crystallinity, thermal degradation, and morphology. UV-Vis absorbance determines the amount of energy that can be absorbed by the donor phase. When absorbance is coupled with fluorescence, the optical band gap of the material can be determined. Optical band gap is important due to its direct correlation to the spectral regions that is capable of being absorbed and subsequently converted into excitons. Equation 6 and Figure 84 illustrate this correlation. In considering the optical band gap of the synthesized P3HT, the peak heights of the maximum absorbance and maximum fluorescence

wavelengths are both normalized to a value of one. The point where the two curves intersect is considered the wavelength related to the optical band gap.

$$Wavelength\ (nm) = \frac{h \times c}{eV}$$

Equation 6. Correlation of optical band gap to the solar spectrum.

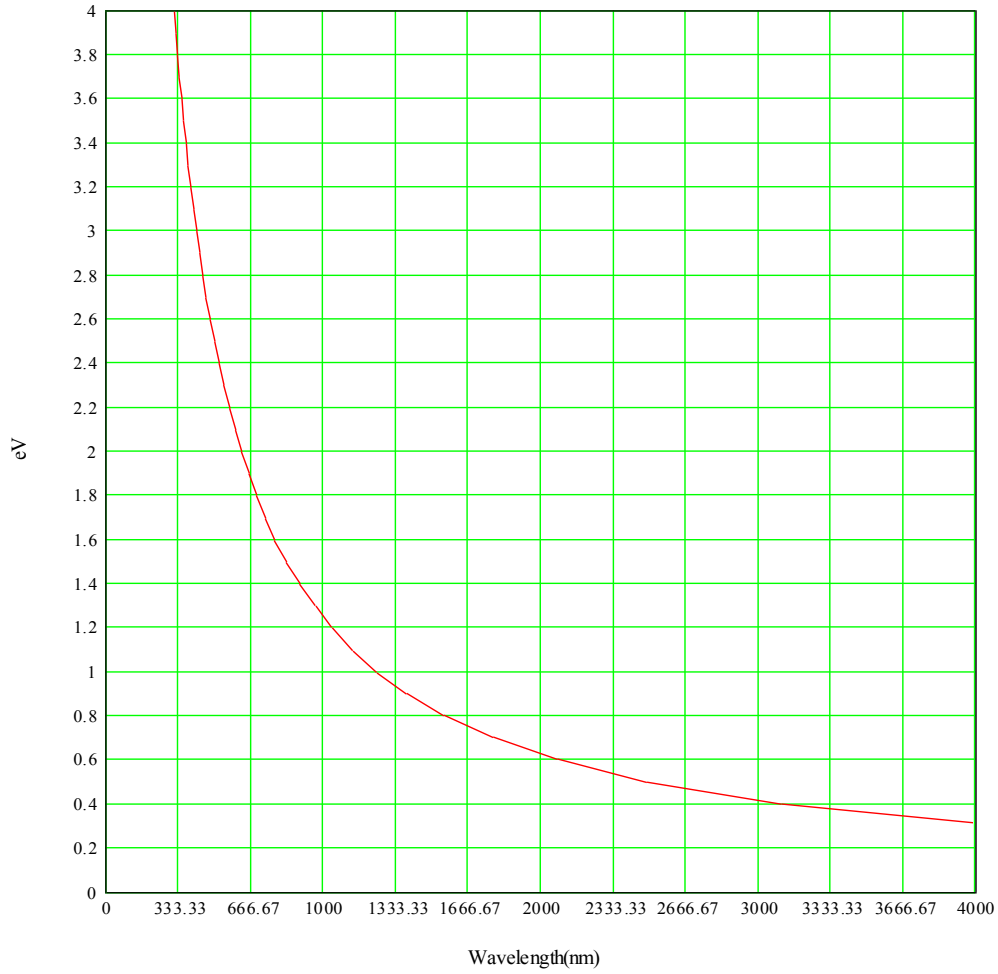

Figure 84. Graph illustrating band gap correlation to the solar spectrum.

The absorbance spectrum for each individual sample is valuable on many different fronts. On top of the ability to use the absorbance spectrum in combination with the fluorescence spectrum and calculate optical band gap, information about the level of crystallinity and that of crystal type can be

determined by the shape of the resulting curve. Figure 85 is an example of P3HT absorbance and fluorescence in chloroform. The intersecting point is at 550 nm, relating to an optical band gap of 2.3 eV in Figure 84. The shape of the absorbance curve is a single peak and centers at approximately 460 nm indicating a single mode of absorption. However, both absorbance and fluorescence are greatly affected by being either in solution or dried due to the chain crystallinity. This shift is illustrated in Figure 86, which depicts the changes in the absorbance λ_{max} and curve shape from a solution of 1wt% P3HT in chloroform as it dries. The solution (10 microliters) was placed into a 300 µL well of a 96 well plate and a spectrum was obtained every 75 seconds to capture the drying/crystallization process, where the arrow indicates the progression of time based on the peak located at 605 nm.

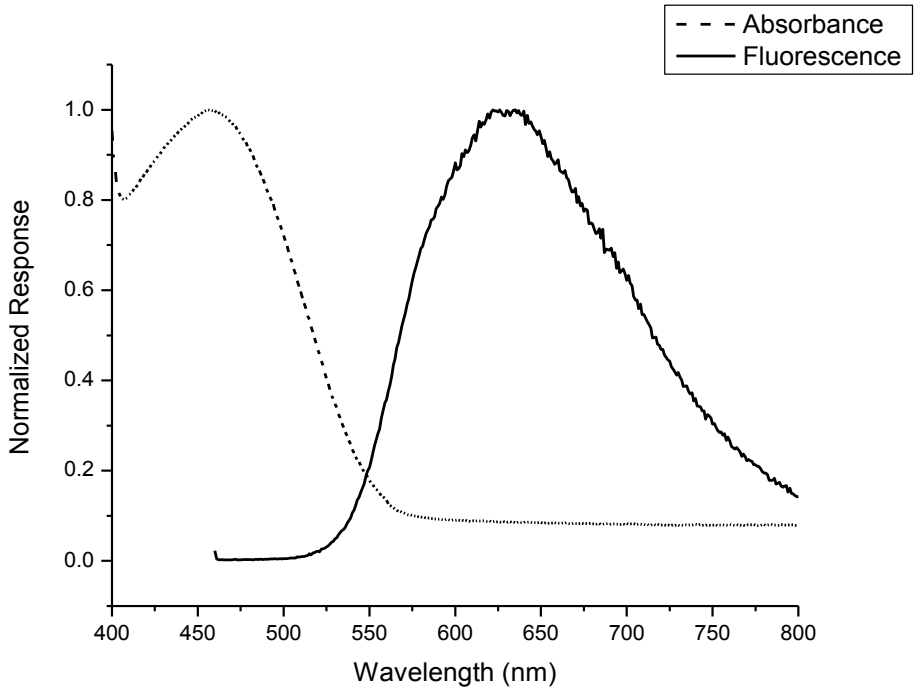

Figure 85. Absorbance and emission spectrum of P3HT in solution of chloroform.

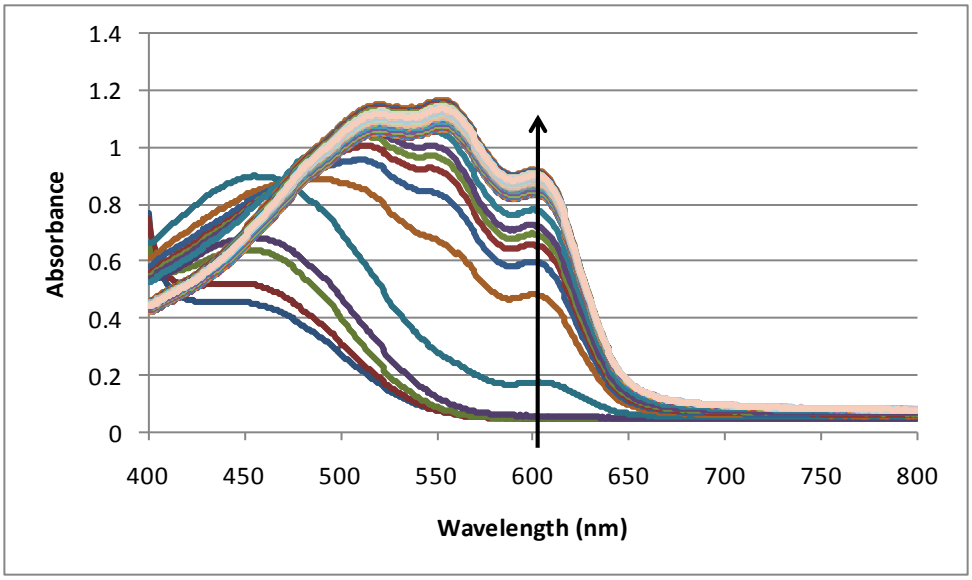

Figure 86. Absorbance of P3HTdrying process cast from 1 wt% chloroform solution.

Upon examination of Figure 86, four specific absorbencies are evident. Each of these peaks relate to a variance in the crystallinity and local structure. The peak centered at approximately 460 nm relates to the fully soluble amorphous chains, and shifts towards 510 nm as the film dries due to the reduced spacing between chains. The remaining peaks offer the most insight into the ultimate structure formation as the peak centered on 550 nm relates to short chain order, or specifically side chain crystallinity, and the peak centered at approximately 605 nm relates to long range order and is attributed to main chain crystallinity.[8, 9] An important piece of information that can be obtained from this plot is the relative time each of the crystalline regimes begins to form. The main chain crystallinity, or π-π stacking, dominates the early crystal formation, and is responsible for higher conductivity levels. The results suggest longer (higher boiling point) and better solvents will allow for increased order of the main chain crystals resulting in higher conductivity and exciton transport.

It is also of note that the fluorescence spectra of dry films are significantly affected by the level of crystallinity. Figure 87 reveals the normalized absorbance and fluorescence of a dried film. This graph indicates a new optical band gap, 637 nm, which correlates with an electronic band gap of approximately 1.9 eV. The dry film optical bandgap becomes the working bandgap for the final material and will ultimately control the properties of the absorbance and its ability to convert the photons into electrical energy. This figure also illustrates the shift in the fluorescence λ_{max} from 630 nm to 725 nm when the P3HT is in a solution of chloroform to a dry film.

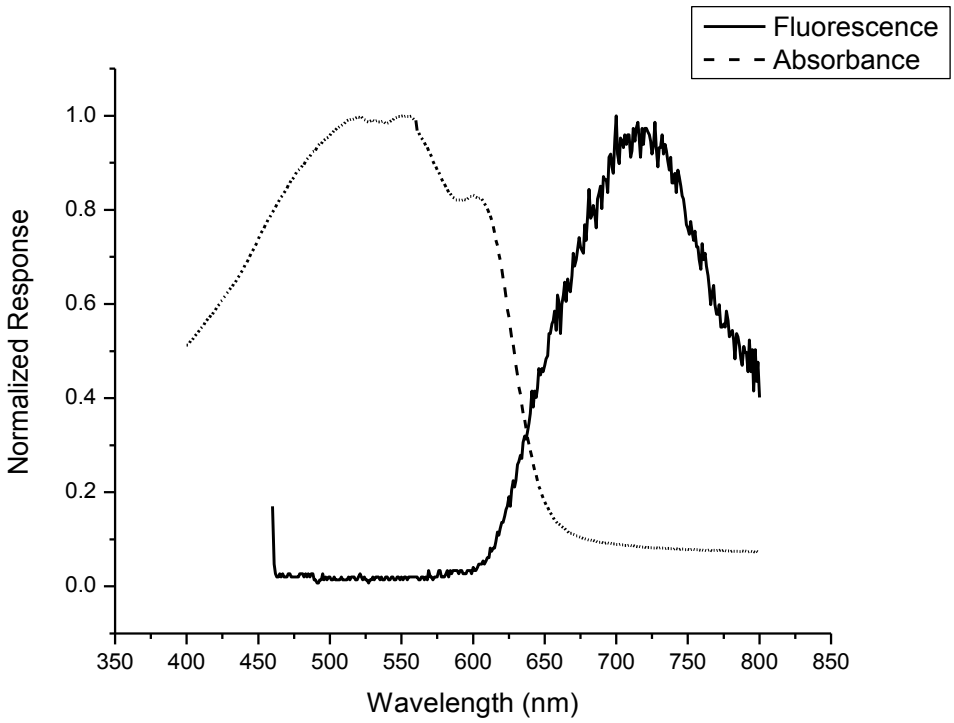

Figure 87. Normalized UV-Vis and fluorescence of dry P3HT film.

Following the complete absorbance and fluorescence evaluation of P3HT homopolymer, it is logical to compare the results to the completed block

copolymers, as well as the fullerene homopolymer. Solutions of a completed block copolymer, styrene:CMS/fullerene homopolymer and a physical blend of the two homopolymers were prepared in chloroform. The solutions were prepared at concentrations where the resulting absorbencies related to the P3HT segments or fractions were on the same magnitude. The resulting absorbance spectra are shown in Figure 88. In this figure, it is important to note that the maximum absorbencies are within the same magnitude of one another, excluding the fullerene containing homopolymer. The normalization to absorbance will result in comparable fluorescence spectra if quenching does not occur within the material.

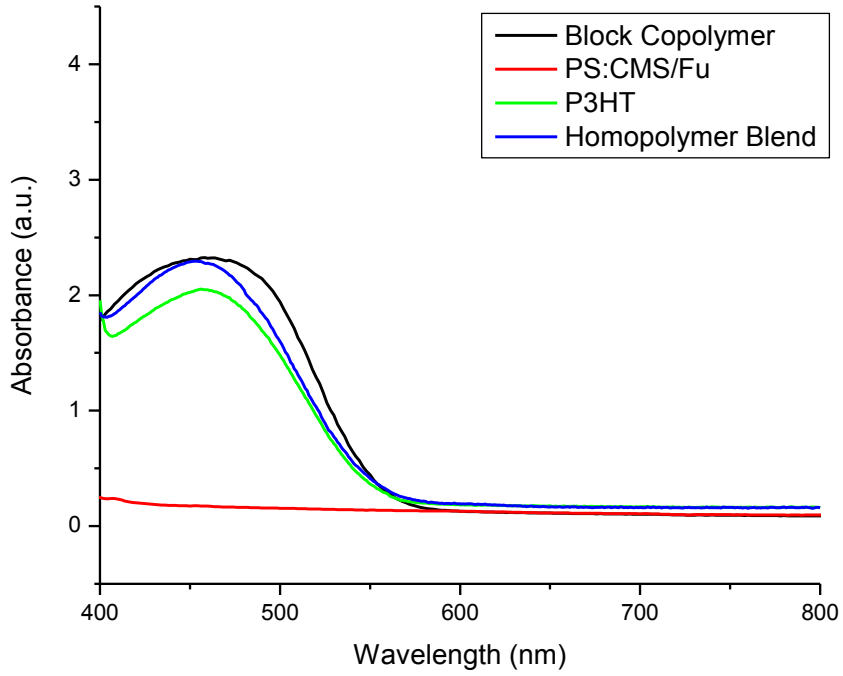

Figure 88. Comparison of block copolymer and homopolymer absorbencies in chloroform.

Following the absorbance spectra normalization by concentration of P3HT, fluorescence was measured. For this group of polymers, fluorescence

offers insight into the efficacy of the transfer of excitons into the acceptor phase. Figure 89 illustrates the chloroform solutions and their resulting fluorescence when excited at 450 nm where Figure 90 is the resulting spectrum after drying.

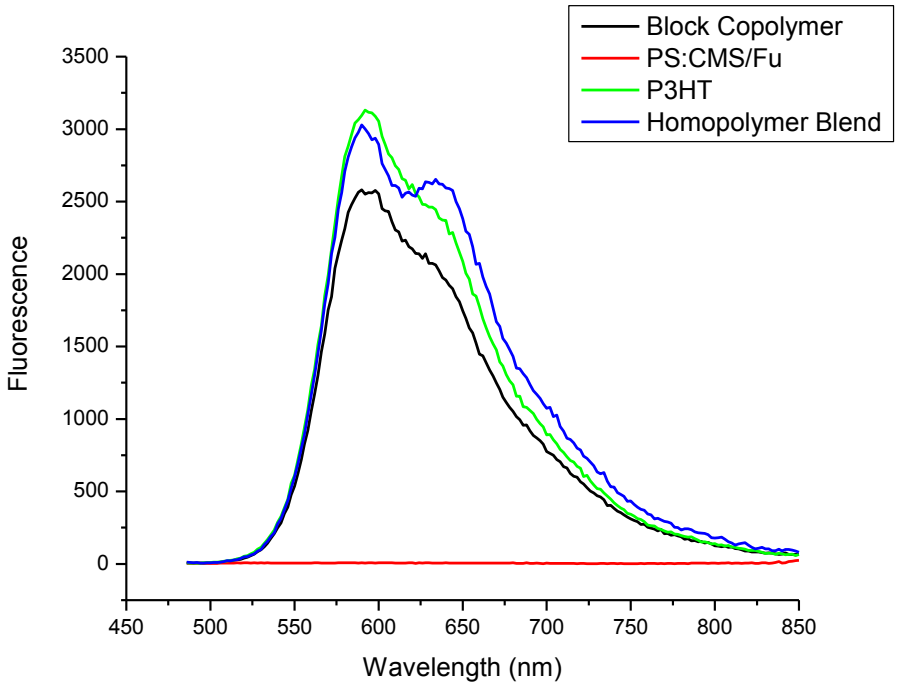

Figure 89. Comparison of block copolymer and homopolymer fluorescence in chloroform.

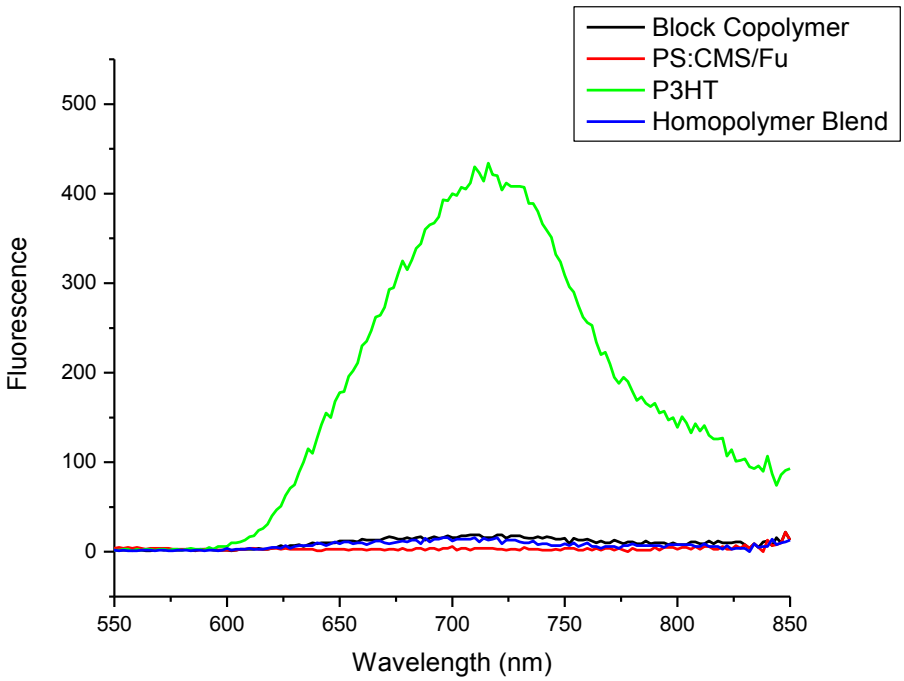

Figure 90. Comparison of block copolymer and homopolymer fluorescence in dry films, illustrating quenching.

Figure 89 illustrates a bimodal peak distribution for fluorescence, relating to the drying or aggregation effect of the films following the absorbance spectra. However, the relative fluorescence change between the samples can be related to quenching of excitons. The obvious sample in this case is the fullerene containing homopolymer which shows no absorbance or fluorescence within the region measured, suggesting that no excitons are generated. The P3HT sample indicates the largest fluorescence peak; however, it shows a more unimodal distribution of the sample. The increased bimodal distribution could be the direct effect of aggregation in solution, which is enhanced in the more concentrated solutions. Further comparison of the sample indicates that the block copolymer produces the lowest fluorescence, which is theorized to be related to single chain quenching due to the covalently bonded nature of the polymer. Figure 90 depicts

the same samples after drying; these fluorescence peaks are also compared against the wet absorbance due to the drastic increase in the absorbance spectra (maxing out the detector) upon drying. This figure shows an obvious difference between the fullerene containing systems and the pure P3HT. To quantify the differences, the areas of absorbance and fluorescence were measured and expressed as a ratio (Table 13).

Table 13

Comparison Of The Areas Of Absorbance And Fluorescence Along With Ratios, Defining Exciton Quenching

	Wet Absorbance Area	**Wet Fluorescence Area**	**Dry Fluorescence Area**	**Wet Ratio**	**Dry Ratio**
Block Copolymer	305.79	306,740	2,966	1003.11	9.69
PS:CMS/Fu	54.15	1,986	993	36.68	18.34
P3HT	273.73	359,789	53,997	1314.39	197.2
Blend	298.44	380,828	2160	1276.06	7.23

The data presented in Table 13 offers an interesting perspective on the P3HT based systems. The ratios of solution absorbance versus fluorescence follow the expected trend: P3HT exhibiting no quenching, a very small amount in the physically mixed system and increasing quenching through single chains in the block copolymer. Following complete drying of the samples, the order of quenching shifts. As expected, the systems containing fullerene exhibit greater quenching than the P3HT sample; however, the mixed system exhibits the highest order of quenching. This surprising result suggests that a mixed system will perform better than this specific block copolymer. As morphology is

optimized for the block copolymer system, it is believed it will outperform the mixed system. Morphology and photovoltaic response were determined for these samples allowing for a complete comparison of the absorbance-fluorescence results and how they relate to photovoltaic efficiency. These results will be discussed in detail later in this chapter.

Thermal stability and transitions

In the previous chapter, thermal analysis of fullerene, fullerene derivatives and the free standing acceptor block were performed as a direct measure of both fullerene content and degradation mechanisms. This chapter will explore the P3HT segment, as well as, the completed block copolymer degradation and thermal response.

P3HT was examined for thermal stability and degradation by TGA and crystallization energy and glass transition temperature (T_g) by DSC. The initial TGA analyses yield a dual degradation mechanism in an air environment. The TGA analysis (Figure 91) illustrates the loss of approximately 45 wt% at 400ºC for the first mechanism. This weight loss is approximately the weight percent relating to a loss in five units of the side chains. To examine this theory of side chain degradation preceding main chain degradation, TGA-Mass Spec was performed with specific units of weight under consideration. Figure 92 is an example of the results.

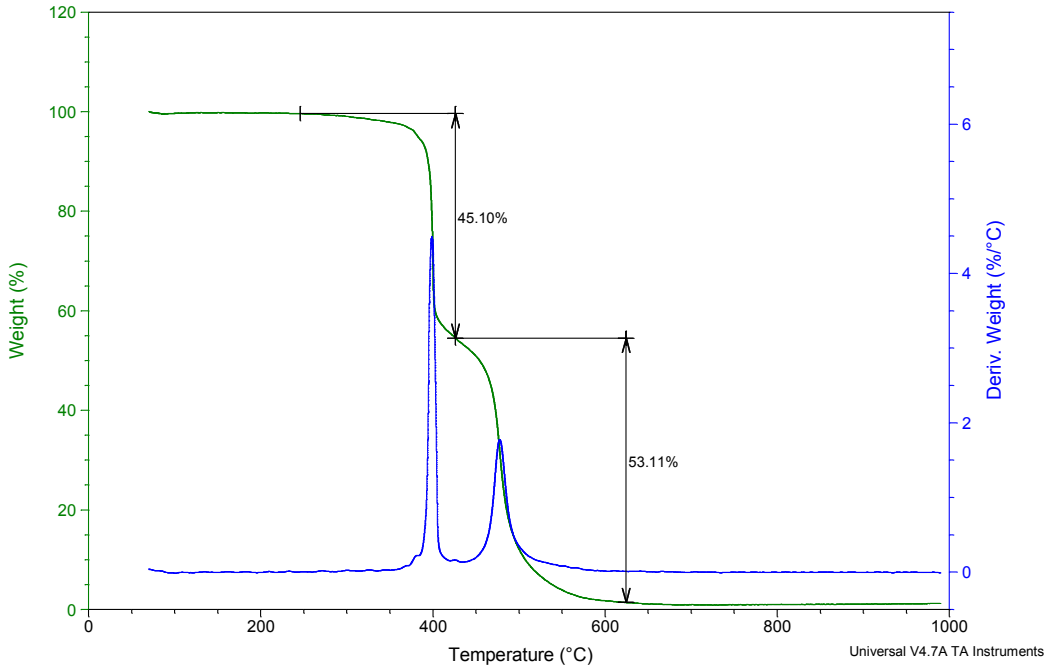

Figure 91. TGA of P3HT performed in air at a rate of 10ºC per minute.

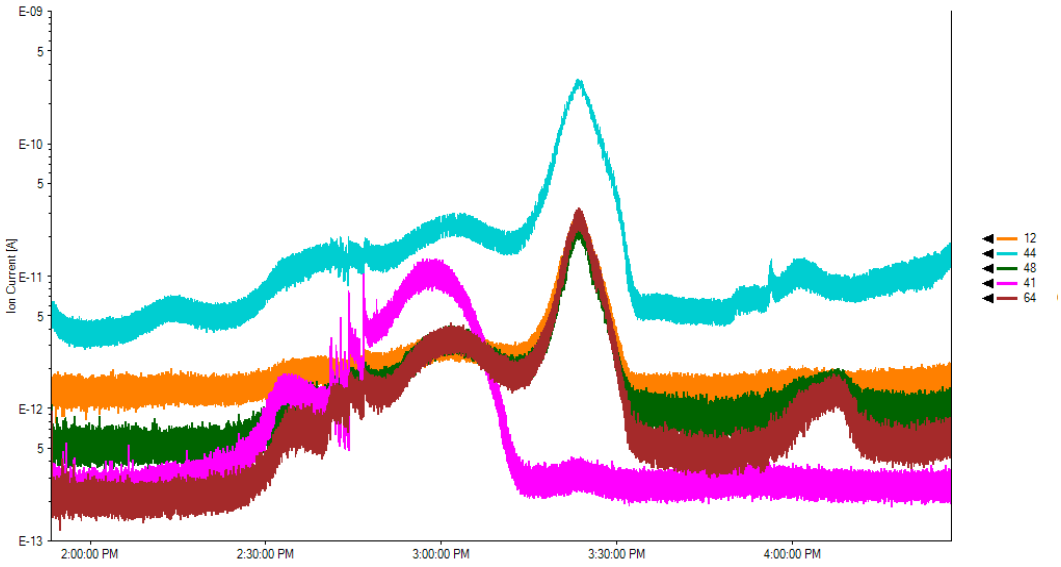

Figure 92. Mass-Spec corresponding to dual degradation mechanisms in P3HT.

The above results confirm the presence of two degradation mechanisms, in that two different degradation products (Figure 92) occur at corresponding times with the weight loss of the sample (Figure 91). This result does not

eliminate side chain degradation as a possible cause for the initial weight loss. It does remove the possibility of five carbon units degrading simultaneously. The degradation of P3HT in air becomes crucial to ultimate photovoltaic performance. Thermal stability to 400ºC suggests that the P3HT is stable under operating conditions that could reach elevated temperatures; however, it does not take into effect the photo degradation in combination with thermal degradation. It is for this reason that tested photovoltaic cells are encapsulated prior to illumination.

Equally if not, more important than the degradation of P3HT is the glass-transition temperature and crystallization temperatures of P3HT. Once P3HT has reached a reasonable molecular weight (~5,000 gm/mole), the T_gs appear to plateau (the crystalline melt magnitude can be altered by molecular weight). Figure 93 shows the DSC thermogram of 10,000 g/mole P3HT. This P3HT depicts a T_g of ~51ºC and a crystalline melt point of 215ºC. It was seen that the magnitude of the crystalline melt is altered between runs. The change in magnitude is attributed to a change in crystalline structure. These temperatures offer insight into the annealing temperatures required for efficient changes in crystalline order and self-organization.

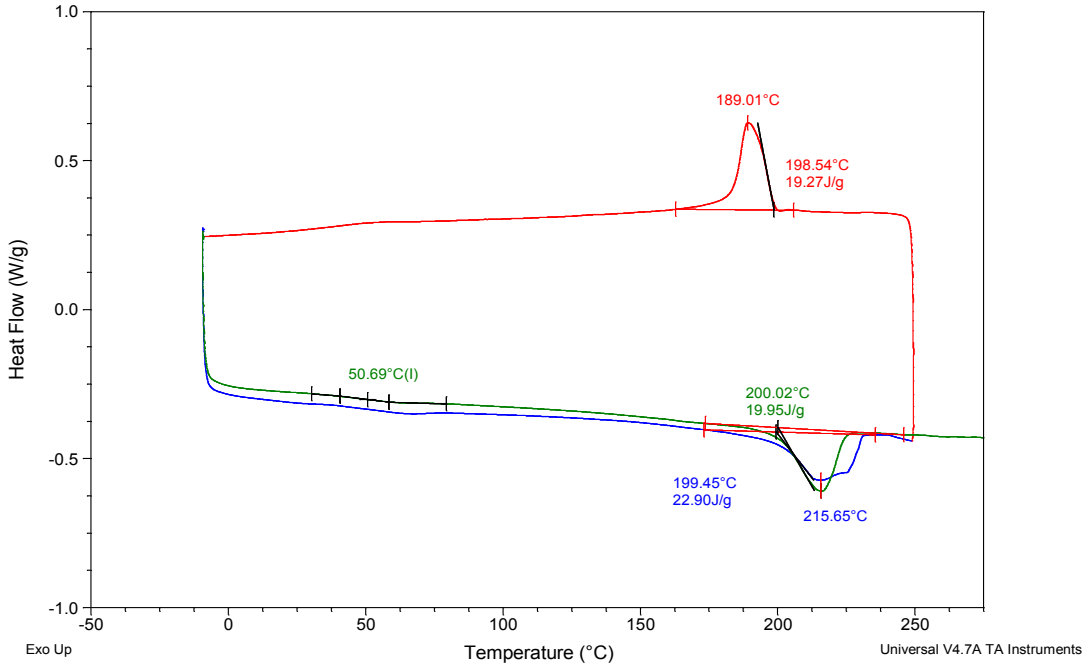

Figure 93. DSC analysis of P3HT illustrating T_g and typical crystalline melt transitions a) first heating pass – blue trace, b) cooling – red trace c) second heating pass – green trace.

The first analysis of the fullerene containing systems involved comparing the oxidative degradation of pure Buckminster Fullerene and PCBM mentioned in the previous chapter. Following the same concept, the P3HT:Styrene:CMS/Fullerene block copolymers were analyzed by TGA for overall fullerene content. Samples were degraded in nitrogen, as well as, runs where the gas was switched to air at 650ºC. Maintaining a nitrogen atmosphere up to 650ºC offers the ability for sharp degradation of fullerene content and a plateau of fullerene content (gaining both sets of information during a single analysis). The drop in weight relative to the nitrogen samples allowed quantification of fullerene content. Figure 94 is representative of the analysis protocol for a system containing approximately 19% fullerene. The level of fullerene achieved is significant from a variety of different material desires.

Foremost, it has been estimated that for dissociated excitons to migrate to collection sites, it is necessary for block copolymers to be ~15 volume % fullerene. A contrary but desired need is to have the appropriate volume fraction in the acceptor phase to drive adequate phase separation on a volume fraction basis. It should be pointed out that the TGA data also revealed the broad initial degradation when analyzing materials containing both the P3HT and polystyrene components.

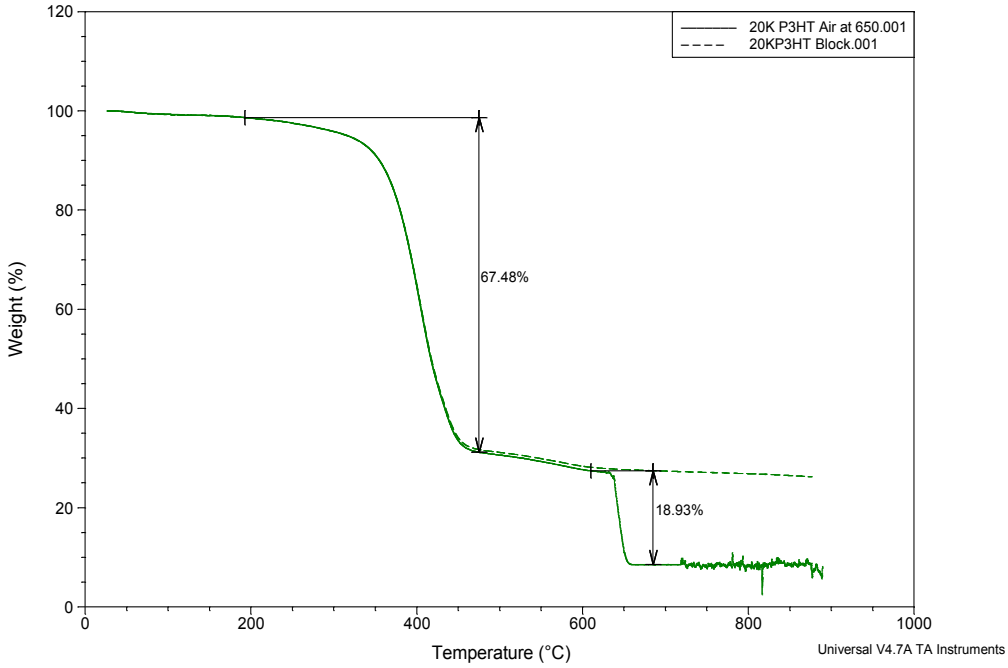

Figure 94. TGA analysis of block copolymers for confirmation of fullerene % incorporation using 20,000 g/mole P3HT performed in 1) in nitrogen up to 650ºC and switched to compressed air at that temperature and compared with 2) the same polymer in a nitrogen atmosphere throughout.

Morphology

The overall goal of controlled morphology through block copolymer synthesis was probed through deposition of polymer systems on mica substrates. AFM was utilized to perform detailed surface analysis and compare the phase

images for P3HT and fullerene functionalized polystyrene physical blends with completed block copolymers. The block copolymers examined were of consistent functionalized polystyrene segment lengths and varying molecular weights of P3HT. Samples were prepared via spin casting at 1,000 rpm using a 1 wt% polymer solution in 1,2-dichlorobenzene followed by annealing at 120ºC for 20 minutes.

The first morphology samples analyzed were a 1:1 weight ratio of purchased P3HT and PCBM to provide a baseline for comparison purposes. Figure 95 is an example of the phase images acquired for these samples and illustrates the relative lack of order in the morphology. Following this analysis, a simple blend of homopolymers, i.e., 20,000 g/mole P3HT and a 20,000 g/mole PS:CMS/Fu at equal weight ratios was analyzed. The phase image shown in Figure 96 is believed to represent significant phase separation where the P3HT phase appears to be driving nano-wire formation and excluding the PS:CMS/Fu phase.

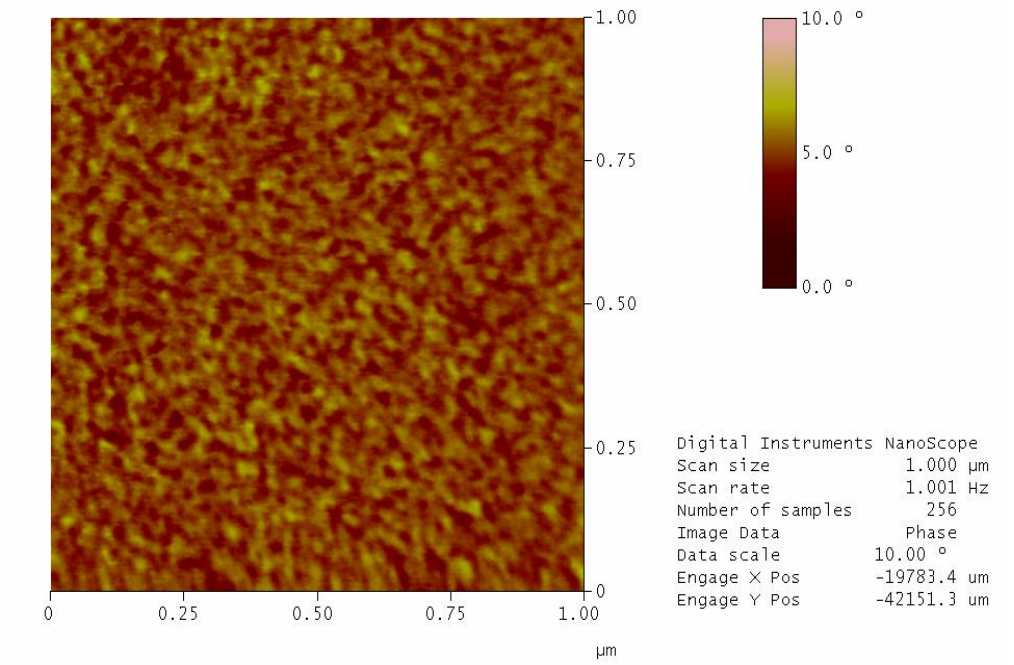

Figure 95. AFM phase image of P3HT and PCBM mix at a 1:1 weight ratio.

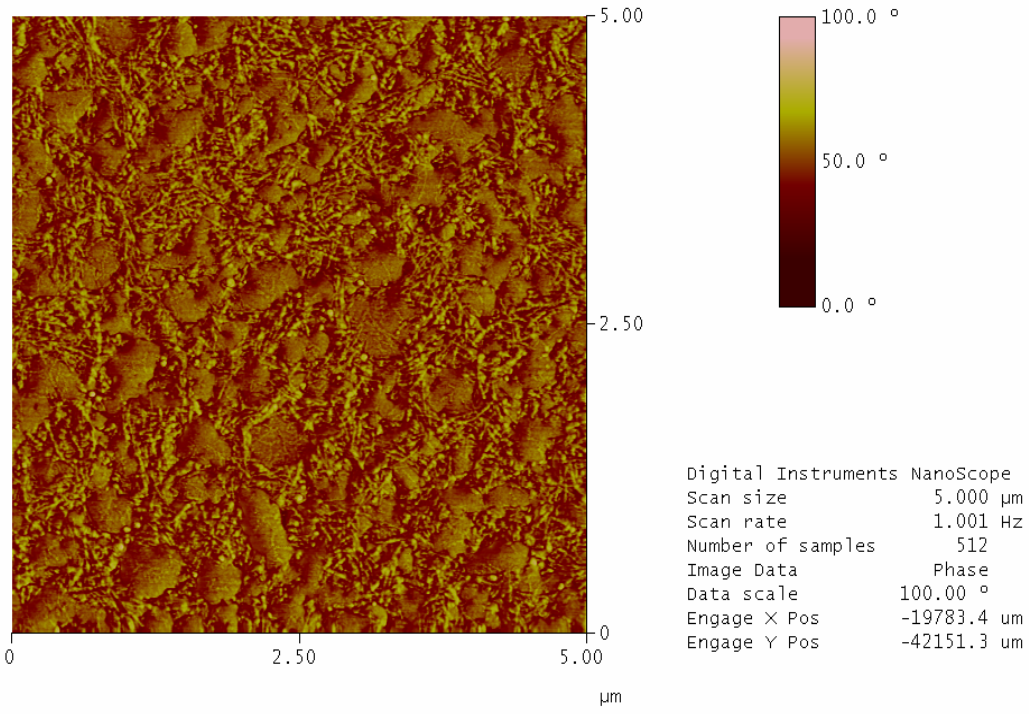

Figure 96. AFM phase image of physical blend of 20,000 g/mole P3HT and 20,000 g/mole PS:CMS/Fu.

Figure 97 reveals the first AFM for a completed block copolymer where the P3HT segment is 10,000 g/mole and the PS:CMS/Fu segment is 20,000 g/mole. The image appears to support a similar nanowire formation and some surface uniformity issues. The same surface uniformity issues were more exaggerated when characterizing the higher molecular weight samples using a variety of conditions, e.g., various solvents, weight percentages, filtering techniques and spin coating speeds. Finally, Figures 98 and 99 illustrate block copolymers with an increased fraction of P3HT. Once again, surface issues became prevalent causing difficulties in imaging. As an additional step, the sample used in generating Figure 99 was filtered through a 0.45 micron filter before casting. The overall results suggest that self-assembly and order is possible; however, the conditions and molecular architecture must still be optimized using other variables such as substrate.

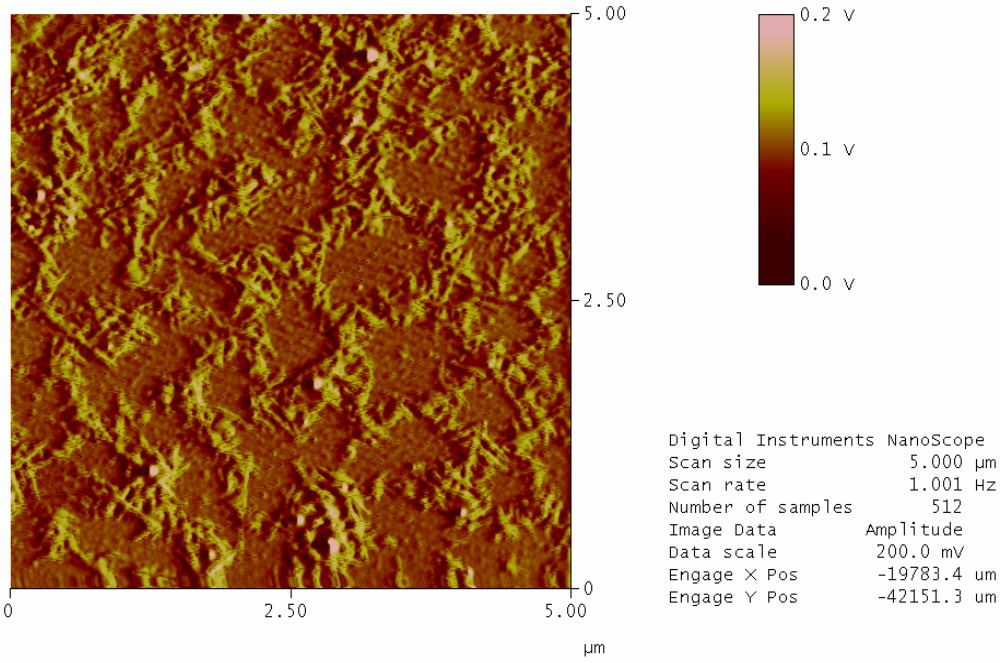

Figure 97. Completed block copolymer of 10,000 g/mole P3HT and 20,000 g/mole PS:CMS/Fu.

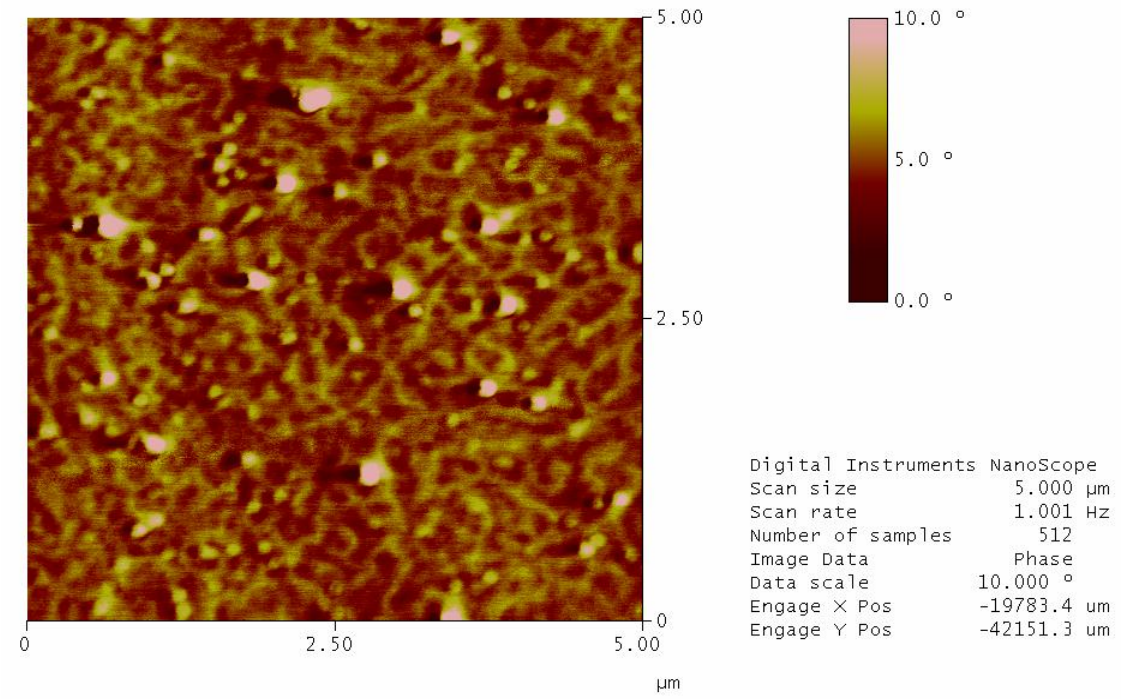

Figure 98. Completed block copolymer of 20,000 g/mole P3HT and 20,000 g/mole PS:CMS/Fu prefiltration.

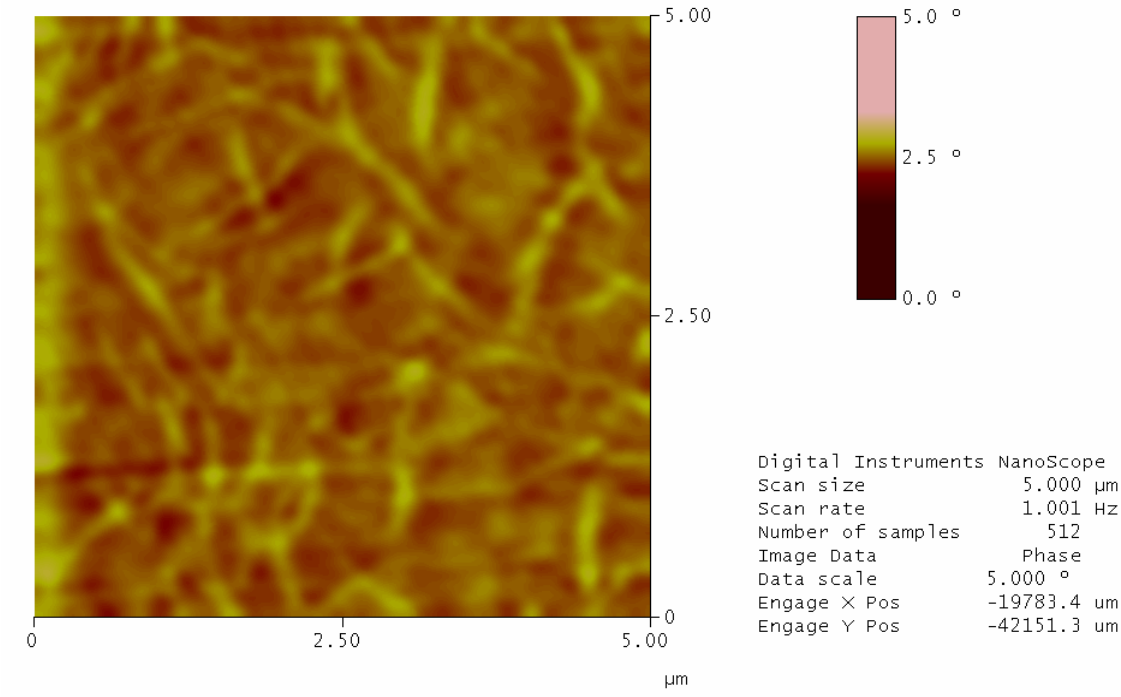

Figure 99. Completed block copolymer of 20,000 g/mole P3HT and 20,000 g/mole PS:CMS/Fu post filtration through 0.45 micron filter.

The morphology response and induction of order are encouraging and led into photovoltaic characterization. The completion of photovoltaic characterization would lead to a correlation of morphology and photovoltaic efficency.

Photovoltaic response

While the system morphologies were not ideal when analyzed, the increased order warranted investigation of photovoltaic properties. Following the same concept as the morphology study, the first cells to be examined were the cells based on the P3HT:PCBM physical blend bulk-heterojunction cells. Figure 100 depicts the voltage-current curve and shows a photovoltaic efficiency of 1.23%. Two primary features of this curve are the short circuit current and open circuit voltage, the intersect points of their respective axes. Perpendicular lines taken from these points generate the expected output, and the difference in area from the actual curve represents the fill factor (FF%).

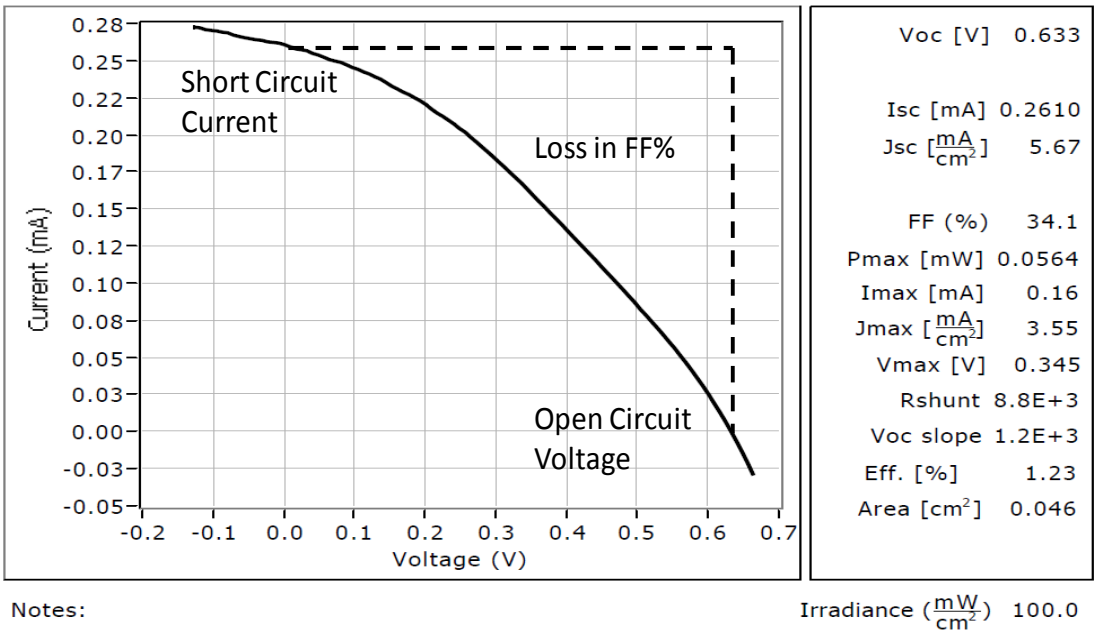

Figure 100. Photovoltaic efficiency curve for P3HT:PCBM bulk heterojunction cell, illustrating the key points for photovoltaic measurement.

With the baseline for our materials set, an examination of both homopolymer blends and block copolymers was performed. Recalling the UV-Vis data reported earlier in this chapter, the homopolymer blend would be expected to perform at a higher level than the block copolymer in this study. This is not the case however, and neither system performed exceedingly well. Figure 101 reveals the data for a physical blend of the homopolymers, i.e., an efficiency of 1.8×10^{-4}% and a fill factor of 43.9%. Figure 102 shows the results for a 20kP3HT-20KPS:CMS/Fu block copolymer with an efficiency of 1.7×10^{-2}% and a fill factor of 20.2%.

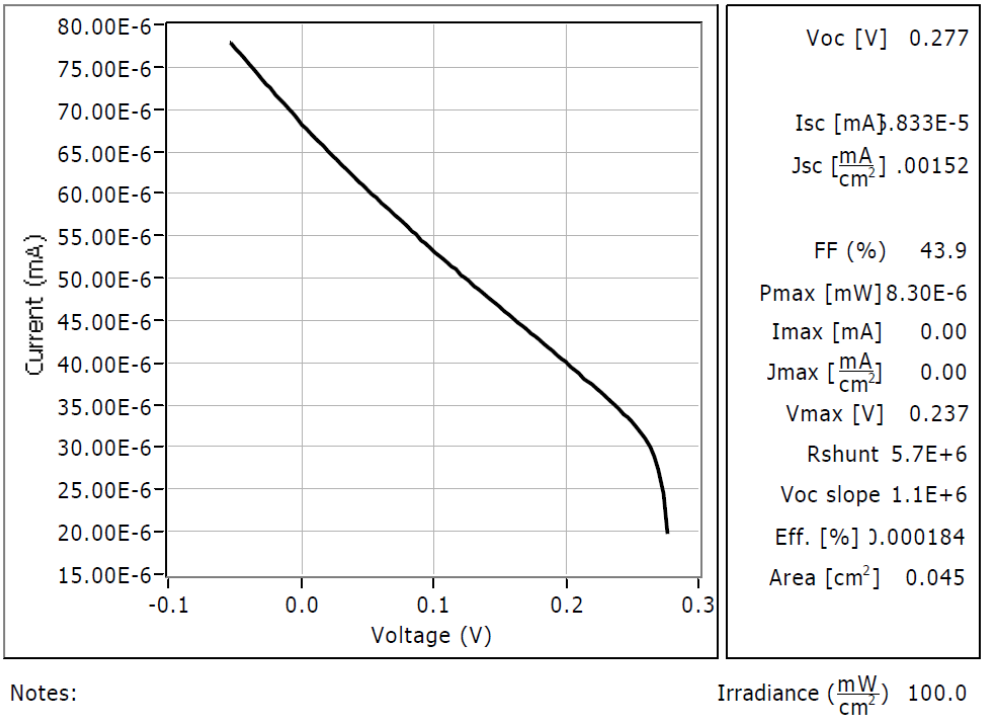

Figure 101. Photovoltaic efficiency curve for P3HT and PS:CMS/Fu physical blend/bulk heterojunction cell.

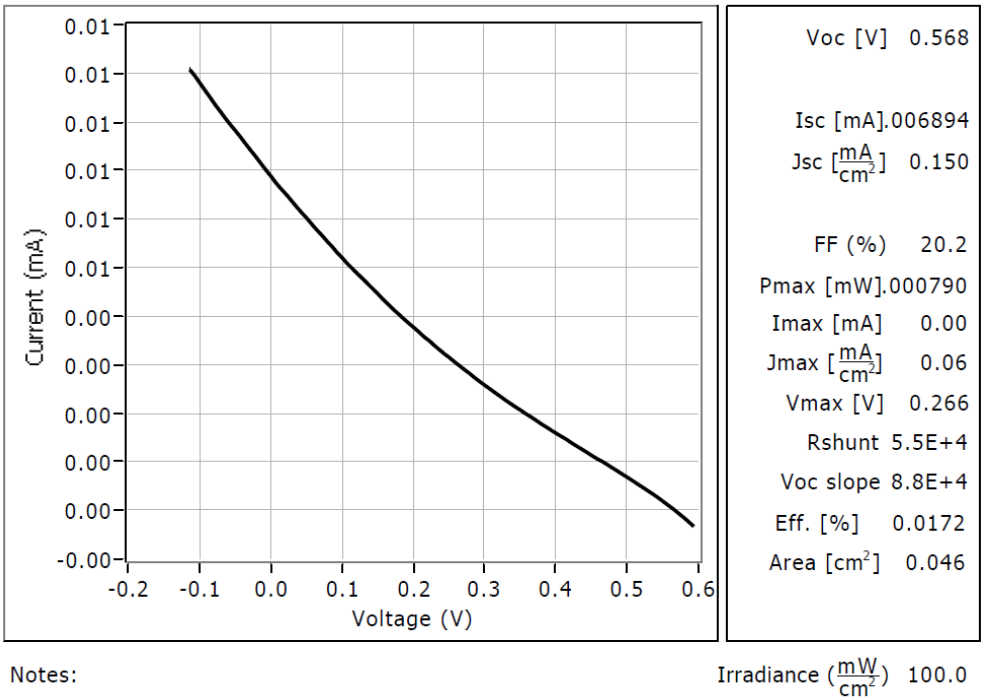

Figure 102. Photovoltaic efficiency curve for P3HT –b-PS:CMS/block copolymer cell.

While these results may appear to be discouraging and do not correspond to the expected increase in efficiency gain with increased morphological control, an expanded view offers insight into the low efficiencies. Figure 103 is a SEM image of the 20kP3HT-20KPS:CMS/Fu block copolymer system at 3000 times magnification. This image illustrates the poor film formation achieved by spin casting of the block copolymer system. This image, coupled with the previous AFM results (large particles on the surface) and promising UV-Vis/Fluorescence, suggests that the problem lies in cell construction and not materials.

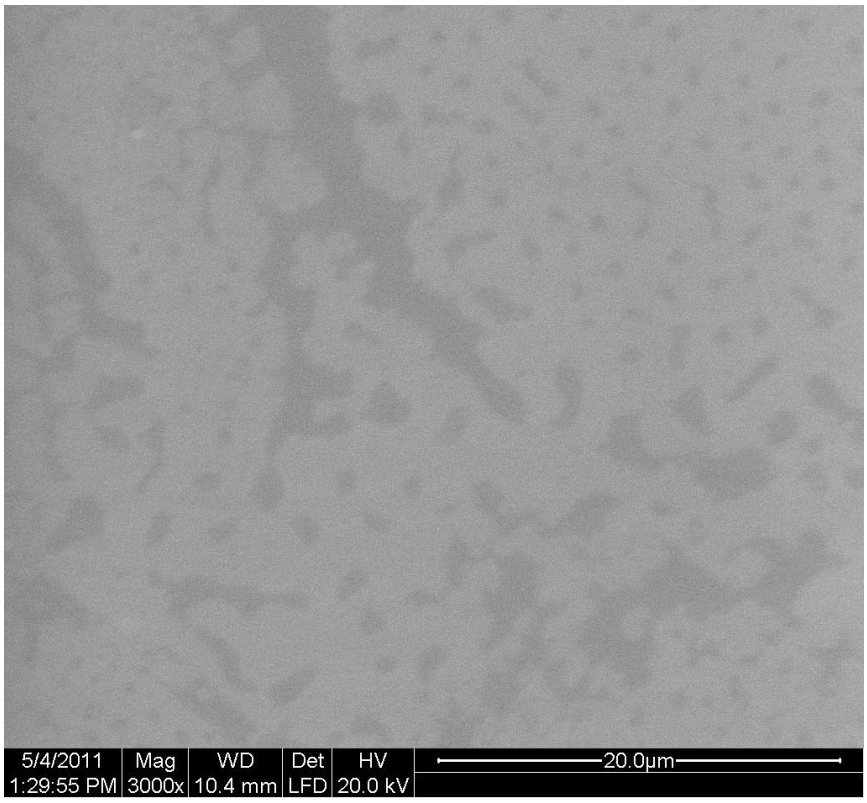

Figure 103. SEM image of 20kP3HT-20KPS:CMS/Fu block copolymer spin cast on mica.

Continued work in the process of creating cells, as well as, material development through novel synthesis, should result in a true correlation between morphology and photovoltaic efficiency.

Summary

The work performed in this chapter details the overall physical properties of both the functionalized homopolymer systems and completed block copolymers. Specifically, thermal degradation of P3HT proved to be a multistep process in which main chain segments are thermally stable in air at temperatures nearing 500ºC. Photon absorption is specific in intensity and wavelength based on the state of the P3HT or completed block copolymers. The results suggest the ability to induce main chain crystallization preferentially over side chain crystalline peaks. The increase in crystallinity, ultimately, will result in more efficient exciton diffusion and transfer. Both block copolymer systems, as well as, homopolymer physical blends show quenching while still in solution, suggesting that the interaction through the polymers are active. However, the block copolymers illustrate increased quenching as compared to the physical blends. Following casting, block copolymers and physical blends both illustrate increased quenching where the physical blends slightly outperform the completed block copolymer.

System morphologies were also examined where both the physical blends and block copolymers illustrated increased order over that of the P3HT:PCBM standard cells. Resulting morphology suggested that further optimization of volume fractions are required and provides promising initial results. Finally, the systems were evaluated for photovoltaic efficiency, offering poor comparative results. The poor results were due in part to film formation, as SEM has shown a discontinuous film which suggested short circuiting upon the photovoltaic testing.

These results offer hope that increased control over the cell construction parameters will result in functioning photovoltaic cells with increased efficiency over the standard blend systems. Morphology and photovoltaic efficiency can be examined and correlated based on volume fraction of block copolymer samples and enhance our understanding of the controlling parameters of photovoltaic activity in a given system.

REFERENCES

1. Trznadel, M.; Pron, A.; Zagorska, M.; Chrzaszcz, R.; Pielichowshki, J. *Macromolecules.* **1998,** 31(15), 5051-5058.
2. Zhao, Y.; Yuan, G.; Roche, P.; Leclerc, M. *Polymer.* **1995**, 36, 2211-2214.
3. Jin, Y.; Cheng, J.; Varma-Nair, M.; Lian, G.; Fu, Y.; Wunderlich, B. *Journal of Physical Chemistry.* **1992**, 96(12), 5151-5156.
4. Garnier, F.; Yassar, A.; Hajlaoui, R.; Horowitz, G.; Deloffre, F.; Servet, B.; Ries, S.; Alnot, P. *Journal of the American Chemical Society.* **1993**, 115(19), 8716-8721.
5. McCullough, R. D.; Williams, S. P. *Journal of the American Chemical Society.* **1993**, 115, 4910-4911.
6. Winokur, M.J.; Prosa, T. J.; Moulton, J.; Smith, P.; Heeger, A. J. *Macromolecules.* **1992**, 25(17), 4364-4372.
7. Chen, T. A., Wu, Z. and Rieke, R. D. *Journal of American Chemical Society.* **1995,** 117, 233-244.
8. Lee, S. H.; Lee, Y. B.; Park, D. H.; Kim, M. S.; Cho, E. H.; Joo, J. *Science and Technology of Advanced Materials.* **2001**, 12, 1-6.
9. Huang, P. T.;, Chang, Y. S.; Chou, C. W. *Journal of Applied Polymer Science.***In Press, 2011**.
10. Chabinyc, M. *Polymer Reviews.* **2008,** 48, 463-492.
11. Jeffries-EL, M.; Sauve, G.; McCullough, R. *Advanced Materials*. **2004,** 16(12), 1017-1019.
12. Holdcraft, S. *Journal of Polymer Science Part B: Polymer Physics*.**1991,** 29(13), 1585-1588.

13. Vanlandingham, M. R.; Mcknight, S. H.; Palmese, F. R.; Elings, J. R.; Huang, X.; Bogetting, T. A.; Eduljee, R. F.; Gillespie, J. W. *Journal of Adhesion.* **1997,** 64(1-4), 31-59.
14. *Device performance; Measurements & characterization .* National Center for Photovoltaics, National Renewable Energy Laboratory (NREL). 2006. Brochure.
15. Green, M. *Physica E.* **2002,** 14, 11-17.
16. Liu, J.; Loewe, R.; McCullough, R. D. *Macromolecules.* **1999,** 32, 5777-5785.

CHAPTER IX

CONCLUSIONS AND RECOMMENDATIONS FOR FUTURE WORK

Conclusions

A consistent feature in materials science research is the ends and means are interconnected at many points along the route of study. Figure 104 summarizes how every property is interconnected. The more complicated the materials function, the more critical the interdependence of intrinsic material properties, fabricated object properties and processing controls become. The research discussed here is no exception. OPV's ultimate properties are tightly associated with both the physical properties of the donor and acceptor domains, as well as, the structural order and morphology of the resulting films, which are highly tied to processing conditions and treatments.

This research project was based upon the hypothesis that OPV efficiency gains are tethered to the size and scale of morphology between donor and acceptor materials. Fully functionalized block copolymers match the appropriate size scale to proof if efficiency limits are directly related to exciton diffusion length/time. Albeit not every question was answered, the project has resulted in improving our understanding of materials for OPV.

The success of photovoltaics based on block copolymers hinge upon the efficient development of broad absorbing molecules that self organize into highly ordered and specific morphologies. The molecular parameters that will control the efficiency are wide and range from conductivity of the donor region, band gap modification and matching, to volume fraction control for specific morphology development. In turn, the processes used to create the final photovoltaic cell

also stretch across a large breadth of areas, where solvent choice, concentration, spin coating speed, electrode choice and annealing procedures all play critical roles. The objective of this research was to develop and understand synthesis routes for both homopolymer and block copolymers that will provide the opportunity to examine morphology and processing conditions in order to lay a foundation of the molecular controlling factors in organic photovoltaic efficacy.

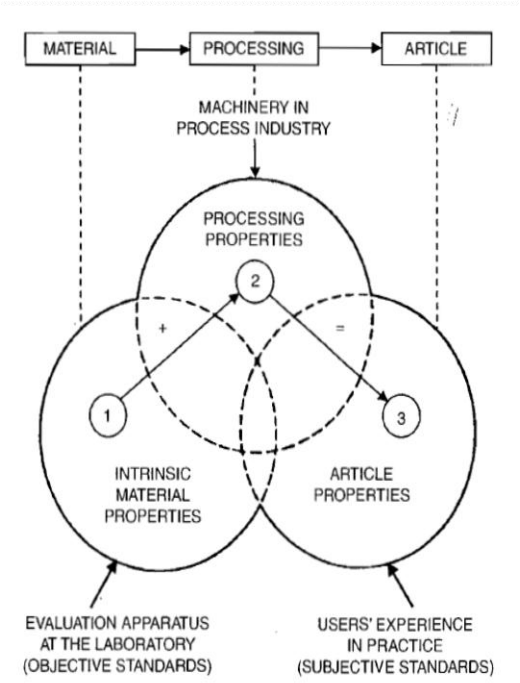

Figure 104. The concept of properties. [1]

The major conclusions of this research are summarized as follows:

1. Thorough study and characterization of the results from the GRIM polymerization of two comparable monomers revealed minimal differences in regioregularity between the two polymers. Ultimately, furthering our hypothesis that regioregularity control is driven by side chain steric hindrance; the data supports that the resulting polymers

are only minimally affected by the directing and leaving group quality/type. The greater energy and time for the additional synthesis steps to produce the iodo substituted monomer leave us preferring the option to purchase the commercially available 2,5-dibromo-3-hexylthiophene.

2. The mechanism of Grignard metathesis polymerization of 3-hexylthiophene was characterized using many experimental parameters as reported in Chapters II, III and IV. The resulting evidence continues to support our perspective, that the mediating nickel species diffuses from chain to chain throughout the reaction and the diffusion of the nickel species concurs with a loss of uniform chain ends; however, the resulting polymers did not correspond directly to a loss in molecular weight or regioregularity control.
3. The resulting molecular weight of P3HT is controlled at a ratio directly proportional to the monomer to nickel ratio and initial monomer molarity, with the latter dominating under our entire series of investigated conditions (more than 200 P3HT GRIM polymerizations were performed using a drastic variety of conditions). A combination of polymerization kinetics, molecular weight monitoring and end group analysis after each quenching (methanol and HCl) confirms another possible mechanism for polymerization and offers insight into improved molecular weight control and more precise control over the resulting polymer architecture, i.e., regioregularity.

4. An important aspect of our research is founded in the kinetic analysis that identified the Grignardization step, which creates activated monomer, as the rate limiting step in the polymerization reaction. Manipulation of this rate controlling step alters the variables and can also result in changes in molecular weight and end-capping efficiency while maintaining the overall yield of the polymerization when quantified as the absence of monomer.
5. Vinyl magnesium bromide provided efficient end-capping reactions for the Grignard Metathesis polymerization of 2,5-dibromo-3-hexylthiophene.
6. Contrary to above, another attempted route using a synthesized Grignard species containing potential latent nitroxide mediating polymerization sites did not end-cap sufficiently.
7. Post successful vinyl end capping reactions, several site-transformation reactions were also examined. These included hydroboration/oxidation reactions for block-block coupling reactions and Heck coupling modifications to facilitate further options for sequential block growth. The hydroboration/oxidation reactions proved to be highly efficient, whereas the Heck coupling reactions, under our conditions, resulted in extremely low conversion efficiency. The results were attributed to several potential main chain coordinated side reactions.

8. Acid functional copolymers consisting of styrene and chloromethyl styrene at varying molecular weights and percent chloromethyl styrene incorporation were synthesized. Molecular weight and composition control of the copolymers were controlled most directly by the combined addition of a nitroxide mediating agent (TEMPO) and feed composition, respectively. Furthermore, the reaction conditions (solvent) and the temperature exhibited a combined effect for satisfactory levels of polydispersity.
9. The specific conditions necessary for successful avoidance of multi-step crosslinking additions with Buckminster Fullerene to polystyrene:chloromethyl styrene co-polymers were developed.
10. Thermal characterization/analyses of the controls, negative controls and Buckminster Fullerene polymers were tested, and a method developed to measure for the characteristic degradation and also direct quantification of the tethered fullerene content.
11. Finally, block copolymers were produced matching our original goal, resulting in a series of tailored and tunable sizes/molecular weights, volume ratios of blocks and exhibiting both donor and acceptor responses as necessary for organic photovoltaic materials.
12. The block copolymer series has been characterized for thermal response and a thorough characterization protocol has been established.

13. Singularly and in combination, the physical properties of both individual functionalized homopolymer systems and the completed block copolymer series were performed.
14. Thermal degradation of P3HT has been proven to be a multistep process exhibiting main chain thermal stability in air at temperatures nearing 500ºC.
15. Photon absorption is specific in intensity and wavelength based on the physical/chemical state of the P3HT or completed block copolymers. The data can be explained from a perspective that the ability to induce main chain crystallization is possible and preferential over side chain crystalline peaks. The higher organization driven by main chain crystallinity has promise to ultimately drive efficient exciton diffusion and transfer.
16. Fully functionalized diblock copolymer systems exhibit increased quenching when evaluated in solution versus physical homopolymer blends, suggesting a single chain quenching mechanism, as would be expected, in an all-in-one donor:acceptor block copolymer.
17. Post solvent cast block copolymers and physical blends both illustrate UV Vis quenching, where the physical blends slightly outperform the completed block copolymer in quenching efficiency.
18. Physical blends of homopolymers and block copolymers illustrated a higher degree of morphological order over that of the P3HT:PCBM standard cells. The range of resulting morphologies support that

further optimization of volume fractions/ratios are required. The data were promising initial results.

19. Systems were evaluated for photovoltaic efficiency and initially delivered poor results when compared with P3HT:PCBM cells (physically blended cells). The less than desirable results were attributed in part to poor film formation control and process.

The combination of these results provides a solid foundation to synthesize, study, and understand the critical parameters that control organic photovoltaic efficiency. Albeit broad in scope, the parameters of interest that are now open for study include the molecular level absorption and transfer/conversion of photons to electrons and the opposite extreme of macroscale finished PV cell formation. The range of precursors, processes, and protocols result in a series of assembled materials and devices. These are expected to expand into an ever growing knowledge base for future improvements on efficiency through both materials (absorption and self-assembly into appropriate morphologies) and processes (film formation and annealing).

Suggestions for Future Work

While my research primarily focused on the synthesis of controlled length block copolymers and the mechanisms used to maintain regioregularity and afford control, these synthesis are performed with an ultimate purpose; i.e., increased OPV efficiency. For gains in understanding and continued OPV improvement, my suggestions for future work remain focused on the synthesis of defined block copolymers. Specifically, modification of the synthetic steps to

generate a sequential block copolymer would facilitate a systematic examination of polymeric OPV materials that are near 100% coupled. Ultimately this process will define how, if at all, an active material's morphology control is affected by coupling efficiency.

In terms of morphology, systems studying the changes in volume fraction could provide a complete map of the rod-coil morphologies produced from these systems, offering insight in the interactions of stiffness factors and solubility parameters. This insight would offer an added area of interest when studying and modeling the phase separation and mixing of both block copolymers, as well as polymer blends.

Cell construction is barraged with variables influencing the final efficiency of the cell. In order to determine how to best create cells with our given system, a study involving solvent choice, film deposition methods, annealing process and encapsulation must be defined. Perhaps the most time critical of these steps is the annealing process, where temperature seemed less significant but heating and cooling rates were revealed as the morphology controlling factors.

With these suggested research activities completed and the corresponding photovoltaic response curves generated, the results are estimated to create cells of higher efficiency and aid in defining the key steps of both molecular engineering and macroscale engineering that have influence on device output. This will ultimately allow the highest efficiency of these systems to be produced, but also allow new materials to be developed in which the downfalls could be addressed. Complete understanding of the processes involved and the

material properties required will allow for an economically viable, efficient photovoltaic cell to be produced, benefiting both the environment and economic stability.

REFERENCES

1. Nijenhuis, Van Krevelen**.** *Properties of Polymers.* 4th . Elsevier: New York, **2010.**